Mathematisches Forschungsinstitut Oberwolfach

Report No. 21/2023

DOI: 10.4171/OWR/2023/21

Tomographic Inverse Problems: Mathematical Challenges and Novel Applications

Organized by
Simon Arridge, London
Martin Burger, Erlangen
Bernadette Hahn, Stuttgart
Eric Todd Quinto, Medford

30 April – 5 May 2023

Abstract. This workshop brought together researchers working on mathematical problems related to tomography, with a particular emphasis on novel applications and associated mathematical challenges. Examples of respective issues represented in the workshop were tomographic imaging with Compton cameras or coupled-physics imaging, resolution and aliasing, vector and tensor field tomography, diffraction tomography, magnetic particle tomography, and limited data, all of which are motivated by the many modern applications. These topics were complemented by novel algorithmic strategies in the solution of tomographic inverse problems, such as stochastic methods and machine learning techniques. Bringing together mathematical and scientific researchers working on these different mathematical problems created a fruitful interchange with novel ideas and strong impact for the future of the field.

Mathematics Subject Classification (2020): 44A12, 92C55, 65Rxx, 44XX, 86XX.

Introduction by the Organizers

Tomography is the mathematics, physics, and technology used to image the internal properties of objects using indirect data. It has revolutionized fields from diagnostic medicine to nondestructive evaluation by allowing doctors to diagnose diseases without exploratory surgery and researchers to find defects in objects from external observations. Tomographic problems are inverse problems because one wants to go backward from the data to the object that generated it.

The workshop *Tomographic Inverse Problems: Mathematical Challenges and Novel Applications* brought together forty-five participants from Europe and Asia as well as North and South America. Their expertise covered a broad range of areas from pure mathematics to numerical analysis and practical applications in medicine, science, and industry. Besides international experts and young scientists, the group of participants included six graduate students whose talks and posters were especially effective to introduce these new researchers to the field. This was a diverse workshop. In particular, the discussions and the talks reflected the high quality of the young mathematicians in the field. This is the eleventh Oberwolfach workshop in this series. The first workshop, in 1980, was crucial for the development of this then-young field. As the field has grown and broadened, the themes of the workshop series have expanded, and these workshops remain crucial to the development of the field and of its practitioners.

New X-ray detectors have recently been developed that record energy (proportional to frequency) as well as intensity, and this opens important new tomographic modalities. In Compton tomography, one images objects using photons whose scatter obeys the Compton effect. The mathematical model involves a new Radon transform that integrates over surfaces of rotation of circles to generate American football or “apple” shaped spindle tori. Important open problems include determining effective data acquisition methods and finding stable reconstruction methods. To do this, one must develop the mathematical properties of the transforms. Other Compton models include V-line and conical methods, and they generate their own questions. In most of these problems, the data are limited, and understanding what object features are visible is important and involves deep pure mathematics. These fields were well-represented at the workshop.

Another novel direction in X-ray imaging is three-dimensional nano-tomography, which leads to interesting combinations of phase retrieval and tomographic reconstruction problems. This field of diffractive imaging was represented at the workshop in talks on all instances from practical issues to mathematical reconstruction techniques and their theory.

Vector and tensor tomography are interesting extensions of the classical tomography approaches, which were represented at the workshop by talks on diffractive versions thereof as well as fast inversion formulae. Further versions of the tomography problems related to limited angle and low dose data were covered by several talks, including the application of dental CT. Similar problems appearing in magnetoacoustoelectric tomography, leading to weighted Radon transform of vector fields, were also reported.

Many tomographic modalities share similar mathematical models, and progress in one application can benefit other applications. Examples include coupled physics imaging (CPI) techniques, modalities where user-controlled probes generate simulated signals read by a complementary measurement system. A leading example is Photoacoustic Tomography (PAT) which measures pressure waves generated by the body in response to light, and ultrasound measures the reaction of the body to ultrasonic radiation. Other novel examples of CPI presented were magnetoacoustoelectric tomography and optical coherence elastography.

Radar and sonar measure waves generated by radiation reflected off objects. In each case, the measured data can be modeled as averages over circular, spherical or ellipsoidal (or more complicated) wavefronts, allowing for a broad range of approaches. As well as its role in PAT, ultrasound is a direct example of tomographic imaging; recently with the increasing computational resources available, ultrasound tomography by full waveform inversion has become a practical possibility. Another example of imaging of data described by a partial differential equation (PDE) is quantum optics, which was the subject of the final talk in the workshop.

A ubiquitous topic nowadays is deep learning, which also found strong interest at the workshop in the context of improving tomographic reconstruction. In the workshop methods using deep learning for model error correction, for curing issues in limited angle tomography, and for motion estimation from tomography data were presented. Moreover, some talks investigated fundamental issues related to machine learning in inverse problems, including a discussion of potential use cases and limitations as well as theoretical convergence guarantees.

Another interesting issue arising in many practical problems is uncertainties (such as also the model errors mentioned above). Several talks addressed this issue and its mathematical treatment by Bayesian and data-driven approaches.

Besides presenting the current research areas in the field, the workshop was also crucial in fostering existing and initiating new collaborations among participants. Gaël Rigaud and Todd Quinto discussed joint work on Compton scattering tomography; Simon Arridge and Matias Courdurier discussed a new model for phase-contrast tomography; Simon Arridge and John Schotland initiated a collaboration to develop a learned based method for the inverse Born Series; Tim Salditt initiated new collaborations with Martin Burger, Samira Kabri, Lorenz Kuger, and Simon Arridge; to name only a few. This gives a small glimpse into the vibrancy of the field and the important role this workshop series plays in its advancement.

Acknowledgement: The organizers thank Prof. Dr. Huisken and the staff of the Mathematisches Forschungsinstitut Oberwolfach for creating a perfect environment to do serious mathematics. We thank the MFO for their efficient and very helpful organization that made the conference go smoothly and allowed us to focus on the mathematics. The MFO and the workshop organizers would like to thank the National Science Foundation for supporting the participation of junior researchers in the workshop by the grant DMS-2230648, “US Junior Oberwolfach Fellows”. Lastly, we thank the participants themselves for sharing their mathematics and helping create a lively and stimulating workshop.

Workshop: Tomographic Inverse Problems: Mathematical Challenges and Novel Applications

Table of Contents

Andreas Rieder (joint with Kevin Ganster)
On the approximate inversion of generalized Radon transforms emerging in seismic imaging 1113

Benedikt Wirth (joint with Martin Holler)
Exact reconstruction and reconstruction from noisy data: Going beyond point sources? 1116

Jürgen Frikel (joint with Simon Göppel, Markus Haltmeier)
Translation invariant diagonal frame decomposition for the Radon transform 1119

Alexander Katsevich
Reconstruction From Discrete 2D Radon Transform Data – Resolution and Aliasing 1121

Leonid Kunyansky (joint with E. McDugald and B. Shearer)
Weighted Radon transforms of vector fields, with applications to magnetoacoustoelectric tomography 1124

Gaik Ambartsoumian (joint with Mohammad J. Latifi)
Injectivity and stability of the inversion of the star transform 1128

Tim Salditt
Phase Retrieval and Tomographic Reconstruction in X-ray Near-field Diffractive Imaging: Inverse Problems at Work 1131

Voichita Maxim
Tomographic inverse problems: which place for deep learning? 1132

Gaël Rigaud (joint with David Elias Frank)
Data-driven approaches to address model inexactness and motion in Compton Scattering Tomography 1134

Tatiana A. Bubba (joint with Mathilde Galinier, Matti Lassas, Marco Prato, Luca Ratti, Samuli Siltanen)
Integrating data-driven techniques and theoretical guarantees for limited angle tomography 1137

Matias Courdurier (joint with Pablo Arratia, Victor Castañeda, Evelyn Cueva, Steffen Härtel, Axel Osses and Benjamin Palacios)
Mathematical model and stability analysis for an inverse problem in light sheet fluorescence microscopy 1140

Lorenz Kuger (joint with Martin Burger)
Bidirectionality and Multiple Scattering Correction in Compton Camera Imaging 1143

Denise Schmutz (joint with Peter Elbau, Michael Quellmalz, Monika Ritsch-Marte, Otmar Scherzer, Gabriele Steidl)
Rigid Motion Reconstruction in Parallel Beam and Diffraction Tomography 1145

Marius Nitzsche (joint with Bernadette Hahn, Hannes Albers, Tobias Kluth)
Accounting for model inexactnesses in Magnetic Particle Imaging 1148

Stephanie Blanke (joint with Christina Brandt)
Dealing with field imperfections for field-free line magnetic particle imaging 1151

Mathias S. Feinler (joint with Bernadette N. Hahn)
Retrospective Redundancy-based motion estimation in MRI using Deep CNNs 1154

Samira Kabri (joint with Alexander Auras, Danilo Riccio, Hartmut Bauermeister, Martin Benning, Michael Moeller, Martin Burger)
Convergent Data-driven Regularization for CT Reconstruction 1156

Yiqiu Dong (joint with Babak M. Afkham, Nicolai A. Riis, Per Christian Hansen)
Uncertainty Quantification of Inclusion Boundaries 1158

Anuj Abhishek (joint with Thilo Strauss, Taufiquar Khan)
A Bayesian level-set inversion method for simultaneous reconstruction of absorption and diffusion coefficients in diffuse optical tomography 1159

Anne Wald (joint with Stephanie Blanke, Bernadette Hahn-Rigaud, Florian Hartmann, Alice Oberacker)
Recent approaches in nano-CT using inexact models and deep learning . 1161

Jin Keun Seo (joint with Hyoung Suk Park)
Ill-Posed Inverse Problems in Low-Dose Dental Cone-Beam Computed Tomography 1163

Thomas Schuster (joint with Lukas Vierus)
Diffractive tensor field tomography as an inverse problem for a transport equation 1166

Plamen Stefanov
Semiclassical methods in tomography 1169

Felix Lucka (joint with the PAMMOTH team)
Photoacoustic and Ultrasonic Tomography for Breast Imaging 1171

Ming Jiang
Is BMD by DXA or CT reliable? 1174

Alfred K. Louis
Fast Inversion Formulae for Some Ray Transforms in Vector and Tensor Tomography 1177

James W. Webber
On a cylindrical scanning modality in three-dimensional Compton scatter tomography 1179

Marta M. Betcke (joint with Matt G. Foster, Ben T. Cox)
Ray tracing approximations to the acoustic propagation in weakly nonlinear regime with applications in HIFU 1182

Christoph Brune (joint with Len Spek, Tjeerd Jan Heeringa)
Duality for Neural Network Inverse Problems through Reproducing Kernel Banach Spaces 1185

Jakob Sauer Jørgensen (joint with Gemma Fardell, Laura Murgatroyd, Evangelos Papoutsellis and Edoardo Pasca)
Directional regularization for the limited-angle Helsinki Tomography Challenge with the Core Imaging Library (CIL) 1185

Ekaterina Sherina (joint with Lisa Krainz, Simon Hubmer, Otmar Scherzer, Wolfgang Drexler)
Inversion Methods for Strain and Stiffness Reconstruction in Quantitative Optical Coherence Elastography 1186

John C. Schotland
Inverse problems for nonlocal PDEs with applications to quantum optics 1189

Abstracts

On the approximate inversion of generalized Radon transforms emerging in seismic imaging

ANDREAS RIEDER
(joint work with Kevin Ganster)

Wave propagation in a medium that does not admit shear stress is accurately modeled by the acoustic wave equation when, in addition, attenuation is neglected: the pressure wave $u = u(t; \mathbf{x}, \mathbf{x_s})$ at $\mathbf{x} = (x_1, x_2)^\top \in \mathbb{R}^2$ and time $t \geq 0$ satisfies

$$\frac{1}{\nu_{\mathrm{p}}^2}\,\partial_t^2 u - \Delta_{\mathbf{x}} u = \delta(\mathbf{x} - \mathbf{x_s})\delta(t), \qquad u|_{t=0} = \partial_t u|_{t=0} = 0, \tag{1}$$

where the wave is initiated by a source at location $\mathbf{x_s}$ and time $t = 0$ (δ denotes the Dirac distribution in the related variables). The seismic inverse problem in the acoustic regime that we consider reads: reconstruct the sound speed ν_{p} in an open set $X \subset \mathbb{R}^2_+ := \mathbb{R} \times [0, \infty)$ from reflected fields $u(t; \mathbf{x_r}, \mathbf{x_s})$, $(t; \mathbf{x_r}, \mathbf{x_s}) \in [0, T] \times \mathcal{R} \times \mathcal{S}$. Here $\mathcal{S}$ and $\mathcal{R}$ are sets of source and receiver positions in $\partial\mathbb{R}^2_+ = \mathbb{R} \times \{0\}$, respectively, and T is the observation time.

We linearize this nonlinear inverse problem by

$$\frac{1}{\nu_{\mathrm{p}}^2(\mathbf{x})} = \frac{1 + n(\mathbf{x})}{v^2(\mathbf{x})}$$

with a smooth, a priori known background velocity $v = v(\mathbf{x})$ satisfying the geometric optics assumption[1]. Thus, multiple reflections are excluded. The reflectivity n captures the high frequency content of ν_{p} and is the quantity we are interested in.

We assume that pairs of source and receiver positions can be smoothly parametrized by a variable s in an open subset $S \subset \mathbb{R}$, that is, $\mathbf{x_r} = \mathbf{x_r}(s)$ and $\mathbf{x_s} = \mathbf{x_s}(s)$. Using principles of wave propagation under the geometric optics assumption we can show, see [7], that n approximately solves the integral equation

$$Fw(s, t) = 4\pi \int_0^t (u - \widetilde{u})(r; \mathbf{x_r}(s), \mathbf{x_s}(s))\mathrm{d}r. \tag{2}$$

The reference solution $\widetilde{u}$ has to be computed from (1) with v in place of ν_{p}. In (2), the operator F is a generalized Radon transform

$$Fw(s, t) = \int_X A(s, \mathbf{x}) w(\mathbf{x}) \delta\big(t - \varphi(s, \mathbf{x})\big)\mathrm{d}\mathbf{x},$$

$$A(s, \mathbf{x}) = \frac{a(\mathbf{x}, \mathbf{x_s}(s)) a(\mathbf{x}, \mathbf{x_r}(s))}{v^2(\mathbf{x})}, \qquad \varphi(s, \mathbf{x}) = \tau(\mathbf{x}, \mathbf{x_s}(s)) + \tau(\mathbf{x}, \mathbf{x_r}(s)),$$

where the travel time τ and the amplitude a can be computed from

$$|\nabla_{\mathbf{x}} \tau|^2 = v^{-2} \quad \text{and} \quad \mathrm{div}_{\mathbf{x}}(a^2 \nabla_{\mathbf{x}} \tau) = 0. \tag{3}$$

---

[1] Any two points in the medium can be connected by a unique ray of geometric optics. Rays are characteristic curves of the PDE on the left in (3) (eikonal equation).

Define $X = \operatorname{int}\{\mathbf{x} \in \mathbb{R}^2_+ : \nabla_{\mathbf{x}}\varphi(s,\mathbf{x}) \neq \mathbf{0},\ s \in S\}$ and $Y = \{(s,t) : s \in S, t > t_{\text{first}}(s)\}$ where $t_{\text{first}}(s)$ is the time, which the unique ray needs from source to receiver. Then, $F\colon \mathcal{E}'(X) \to \mathcal{D}'(Y)$ is a Fourier integral operator of order $-1/2$ which integrates over reflection isochrones $\mathcal{L}(s,t) = \{\mathbf{x} \in X : t = \varphi(s,\mathbf{x})\}$.

Recently, in [3–5] the authors proposed and analyzed imaging operators $\Lambda = KF^\dagger\psi F$ where K is a properly supported pseudodifferential operator of positive order, $\psi\colon Y \to [0,\infty)$ is a smooth cutoff function, and $F^\dagger$ denotes the generalized backprojection with smooth weight W, that is,

$$F^\dagger u(\mathbf{x}) = \int_S W(s,\mathbf{x})u(s,\varphi(s,\mathbf{x}))\mathrm{d}s.$$

The formal L^2-adjoint F^* has weight $W = A$ and a backprojection with $W = 1/A$ was used in [1]. Further, a numerical scheme for Λ can be based on the concept of approximate inverse [6]. To this end let, for $k > 0$,

$$e_\gamma(\mathbf{x}) = \frac{k+1}{\pi\,\gamma^{2(k+1)}}\begin{cases}(\gamma^2 - |\mathbf{x}|^2)^k & : |\mathbf{x}| < \gamma,\\ 0 & : |\mathbf{x}| \geq \gamma.\end{cases}$$

The family $\{e_\gamma\}_{\gamma>0}$ converges to δ in the distributional sense as $\gamma \to 0$.

Now, for $\mathbf{p} \in X$ and $g \in L^2(Y)$, we define the approximate inverse by

$$\Phi_\gamma g(\mathbf{p}) := \langle \psi g, \upsilon_{\mathbf{p},\gamma}\rangle_{L^2(Y)}$$

where

$$\upsilon_{\mathbf{p},\gamma}(s,t) = \widetilde{F}\big(W(s,\cdot)K^* e_\gamma(\cdot - \mathbf{p})\big)(s,t) \tag{4}$$

is the *reconstruction kernel* and

$$\widetilde{F}\rho(s,t) = \int_{\mathcal{L}(s,t)} \rho(s,\mathbf{x})\,\frac{\mathrm{d}s(\mathbf{x})}{|\nabla_{\mathbf{x}}\varphi(s,\mathbf{x})|}.$$

Note that $\Phi_\gamma Fn(\mathbf{p}) = \Lambda n \star e_\gamma(\mathbf{p})$ is a regularized version of Λn ($\star$ denotes convolution).

The following tasks have to be performed to numerically compute the kernel: 1. Solve the PDEs in (3), for instance, by Fast Marching and Lax-Friedrich sweeping schemes, respectively. 2. Find $\mathcal{L}(s,t)$ efficiently by Marching Squares. 3. Evaluate the right hand side of (4) by a quadrature rule where in concrete settings $K^*e_\gamma(\cdot - \mathbf{p})$ can be computed analytically.

To process these steps in full generality is challenging and subject to ongoing research. However, if one considers a layered background medium, that is, $v(\mathbf{x}) = v(x_2)$, and the common offset acquisition geometry, that is, $\mathbf{x_s}(s) = (s-\alpha, 0)^\top$ and $\mathbf{x_r}(s) = (s+\alpha,0)^\top$ for offset $\alpha \geq 0$ fixed, then invariance properties apply, which reduce the numerical effort considerably, see [2] for implementation details. Figure 1 shows a reconstruction kernel under the assumptions just given.

By the steps explained above we can pre-compute/approximate $\upsilon_{\mathbf{p},\gamma}$ on a grid $\mathcal{S} \times \mathcal{T} \subset Y$ for $\mathbf{p}$ in a discrete set $\mathcal{M}_p \subset X$. Finally, for data g given on a uniform

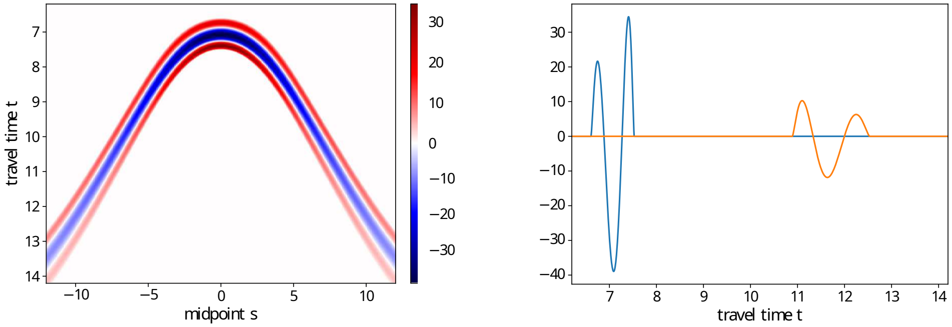

FIGURE 1. Numerical approximation of $\upsilon_{(0,4),1}$ for offset $\alpha = 3$, $k = 3$, $F^\dagger = F^*$, and $K = \Delta M^2$ where M is the multiplication operator by x_2 and Δ is the Laplacian. The background velocity is $v(\mathbf{x}) = \frac{1}{2}\left(1 + x_2 + \frac{1}{2}\cos\left(\frac{\pi}{4}\, x_2\right)\right)$. On the right: cross sections for $s = 0$ (blue) and $s = \pm 9$ (orange).

grid $\mathcal{S}_{\text{data}} \times \mathcal{T}_{\text{data}} \subset Y$ with step sizes $h_{\mathcal{S}_{\text{data}}}$ and $h_{\mathcal{T}_{\text{data}}}$ we get

$$\Phi_\gamma g(\mathbf{p}) \approx h_{\mathcal{S}_{\text{data}}} h_{\mathcal{T}_{\text{data}}} \sum_{\mathcal{S}_{\text{data}}} \sum_{\mathcal{T}_{\text{data}}} \psi|_{\mathcal{S}_{\text{data}} \times \mathcal{T}_{\text{data}}} \circledast g \circledast (\Pi \upsilon_{\mathbf{p},\gamma})|_{\mathcal{S}_{\text{data}} \times \mathcal{T}_{\text{data}}} \tag{5}$$

where Π interpolates the kernel onto the data grid. In (5) we have an element-wise multiplication of three arrays, indicated by $\circledast$, and then we take the sum over rows and columns.

A variety of numerical experiments to demonstrate the performance of this inversion/regularization scheme can be found in [2].

Acknowledgment. We gratefully acknowledge financial support by the Deutsche Forschungsgemeinschaft (DFG, German Research Foundation)
- Project-ID 258734477 - SFB 1173.

REFERENCES

[1] G. Beylkin, *Imaging of discontinuities in the inverse scattering problem by inversion of a causal generalized Radon transform*, J. Math. Phys. **26** (1985), 99–108, `https://dx.doi.org/10.1063/1.526755`.

[2] K. Ganster, A. Rieder *Approximate inversion of a class of generalized Radon transforms*, SIAM J. Imaging Sci. **16** (2023), 842–866, `https://doi.org/10.1137/22M1512417`

[3] C. Grathwohl, P. Kunstmann, E. T. Quinto, and A. Rieder, *Microlocal analysis of imaging operators for effective common offset seismic reconstruction*, Inverse Problems **34** (2018), 114001, `https://doi.org/10.1088/1361-6420/aadc2a`.

[4] C. Grathwohl, P. Kunstmann, E. T. Quinto, and A. Rieder, *Imaging with the elliptic Radon transform in three dimensions from an analytical and numerical perspective*, SIAM J. Imaging Sci. **13** (2020), 2250–2280, `https://doi.org/10.1137/20M1332657`.

[5] P. Kunstmann, E. T. Quinto, and A. Rieder, *Seismic imaging with generalized Radon transforms: stability of the Bolker condition*, CRC 1173 Preprint 2022/3, Karlsruhe Institute of Technology, 2022, `https://doi.org/10.5445/IR/1000141638`. Pure and Applied Mathematics Quarterly (to appear).

[6] A. K. Louis, *Approximate inverse for linear and some nonlinear problems*, Inverse Problems **12** (1996), 175–190, `http://dx.doi.org/10.1088/0266-5611/12/2/005`.
[7] W. W. Symes, *Mathematics of reflection seismology*, Technical report, The Rice Inversion Project, Rice University, Houston, TX, USA (1998). `http://www.trip.caam.rice.edu/downloads/preamble.pdf`.

Exact reconstruction and reconstruction from noisy data: Going beyond point sources?

Benedikt Wirth
(joint work with Martin Holler)

A prototypical example problem for so-called *superresolution* is the following: Given a discrete Radon measure

$$\rho^\dagger = \textstyle\sum_{n=1}^N a_i\delta_{(x_i,y_i)}$$

as ground truth with $a_1,\ldots,a_N\in\mathbb{R}$ and $(x_1,y_1),\ldots,(x_N,y_N)\in\mathbb{T}^2$ for $\mathbb{T}^2$ the flat two-dimensional torus (identified with $[0,1)^2$ for simplicity), can we recover this ground truth from *finitely many* Fourier measurements, i.e. from the measurement

$$f^\dagger = A\rho^\dagger = \left(\textstyle\int_{\mathbb{T}^2}\exp(-2\pi i k\cdot(x,y))\,\mathrm{d}\rho^\dagger(x,y)\right)_{k\in\mathbb{Z}^2,\ |k|_\infty\le K}$$

with some finite cutoff frequency $K>0$? This problem and the related problem of reconstruction from noisy data were solved by various researchers, e.g. [1–3]: Under multiple alternative conditions (such as nonnegativity of $\rho^\dagger$ or a minimum distance condition between the (x_i,y_i)) one can indeed exactly reconstruct $\rho^\dagger$ from $f^\dagger$ by solving the convex minimization problem

$$\min_\rho \mathrm{M}(\rho)\quad\text{such that } A\rho = f^\dagger,$$

in which $\mathrm{M}(\rho)$ denotes the mass or total variation of the Radon measure ρ. Furthermore, if one only has access to noisy measurements f^δ with $\delta=\frac12|f^\delta-f^\dagger|^2>0$, one can replace the above constraint by a convex fidelity term with weight $\alpha>0$ and for instance solve the convex minimization problem

$$\min_\rho \mathrm{M}(\rho)+\tfrac{1}{2\alpha}|A\rho-f^\delta|^2.$$

If α decreases (sufficiently slowly) with δ, then one can estimate the error between the minimizer ρ^δ and $\rho^\dagger$ in some weak norm or related difference measure and show that it converges to zero as $\delta\to0$. The natural question arises to what type of regularizers other than M or measurement operators other than A such results extend. As a first simple example in this direction we replace the regularizer by the so-called *anisotropic total variation*

$$\mathrm{TV}(u)=\mathrm{M}(\partial_x u)+\mathrm{M}(\partial_y u),$$

which is a natural regularizer for the reconstruction of a piecewise constant ground truth image $u^\dagger\in L^1(\mathbb{T}^2)$ with only horizontal and vertical discontinuities at vertical coordinates $y_1,\ldots,y_N$ and horizontal coordinates $x_1,\ldots,x_M$, respectively. Setting again $f^\dagger=Au^\dagger$, we obtain the following result.

Theorem ([4]). *There exists* $C > 0$ *such that, if the discontinuity lines of* $u^\dagger$ *have mutual distance no smaller than* $\frac{C}{K}$ *and if* $\partial_x u^\dagger$ *and* $\partial_y u^\dagger$ *do not change sign on any vertical and horizontal discontinuity line, respectively, then* $u = u^\dagger$ *is unique minimizer of*

$$\min_u \mathrm{TV}(u) \text{ such that } Au = f^\dagger.$$

Further, $\|u^\delta - u^\dagger\|_{L^1} \leq C\delta^{1/4}$ *for any minimizer* u^δ *of*

$$\min_u \mathrm{TV}(u) + \tfrac{1}{\sqrt{\delta}}|Au - f^\delta|^2.$$

The proof follows the same steps as in the reconstruction of point masses $\rho^\dagger$:

- In the noise-free case one first shows that the support of $\partial_x u^\dagger$ and $\partial_y u^\dagger$, the vertical and horizontal discontinuity lines, is correctly identified (while in the point mass setting one would first show that the locations of the Dirac masses in $\rho^\dagger$ are correctly reconstructed). As a consequence, the reconstruction u must also be piecewise constant and has the same discontinuity lines as $u^\dagger$. Then in a second step one shows that the finitely many function values of the reconstruction u coincide with those of $u^\dagger$ (while in the point mass setting one would show that the reconstructed weights of the Dirac masses coincide with those of $\rho^\dagger$).
- In the noisy setting one refines the previous arguments for identifying the support and the values of $\partial_x u^\dagger$ and $\partial_y u^\dagger$ to obtain an estimate for an unbalanced optimal transport distance between $\partial_x u^\delta$ or $\partial_y u^\delta$ and $\partial_x u^\dagger$ or $\partial_y u^\dagger$ (while in the point mass setting one would get an unbalanced optimal transport distance estimate between ρ^δ and $\rho^\dagger$ from such a refinement). In a final step one turns this unbalanced optimal transport estimate into an estimate of $\|u^\delta - u^\dagger\|_{L^1}$.

Optimal transport distances such as the so-called Wasserstein distances are a classical framework to metrize weak-* convergence on the space of probability measures. The above used so-called *unbalanced optimal transport* is a variant in which the total mass of the measure may change so that one is not restricted to probability measures. In the above context a natural unbalanced optimal transport cost between two nonnegative measures $\rho^\delta, \rho^\dagger$ is

$$W_{2,R}^2(\rho^\dagger, \rho^\delta) = \inf_\rho W_2^2(\rho, \rho^\delta) + \tfrac{R^2}{2}\mathrm{M}(\rho^\dagger - \rho)$$

for some fixed parameter $R > 0$, where W_2 denotes the classical Wasserstein-2 distance between nonnegative measures of same mass (for signed measures one simply computes the Wasserstein distance separately for the positive and the negative part). $W_{2,R}^2$ represents a natural error measure if one can only expect weak convergence of reconstructions to the ground truth.

Each of the above listed steps is based on convex analysis principles. Exemplarily we illustrate the first step of identifying the support of $\partial_x u^\dagger$ and $\partial_y u^\dagger$ in the noise-free case: One starts by showing that the following source condition can be satisfied.

Source condition ([4]). There exists $w^\dagger \in \{k \in \mathbb{Z}^2 \,|\, |k|_\infty \leq K\}$ with

$$-A^* w^\dagger \in \partial \mathrm{TV}(u^\dagger),$$

i.e. $A^* w^\dagger = \mathrm{div}\varphi$ for some $\varphi \in H(\mathrm{div}; \mathbb{T}^2)$ with $\varphi_1 \in \partial \mathrm{M}(\partial_x u^\dagger)$, $\varphi_2 \in \partial \mathrm{M}(\partial_y u^\dagger)$ (this implies $|\varphi_1|, |\varphi_2| \leq 1$ and $\varphi_1 = \mathrm{sign}\partial_x u^\dagger$ on the vertical and $\varphi_2 = \mathrm{sign}\partial_y u^\dagger$ on the horizontal discontinuity lines). In addition $w^\dagger$ can be chosen such that

$$|\varphi_1(x,y)| < 1 \text{ unless } x \in \{x_1, \dots, x_M\}, \quad |\varphi_2(x,y)| < 1 \text{ unless } y \in \{y_1, \dots, y_N\}.$$

This compares to a structurally analogous source condition in the setting of point mass reconstruction, which requires the existence of some dual variable $w^\dagger$ such that $-A^* w^\dagger \in \partial \mathrm{M}(\rho^\dagger)$ and $|A^* w^\dagger| < 1$ away from the support of $\rho^\dagger$. In both settings such dual variables $w^\dagger$ or rather the degree K trigonometric polynomials $-A^* w^\dagger$ can be constructed almost explicitly using so-called Fejér kernels (which can be thought of as trigonometric polynomial approximations of Dirac masses). The correct reconstruction of the support of $\partial_x u^\dagger$ and $\partial_y u^\dagger$ is then a direct consequence of the nonnegativity of the so-called *Bregman distance* $D_v^{\mathrm{TV}}(u, u^\dagger)$ for any $v \in \partial \mathrm{TV}(u^\dagger)$: We have

$$\begin{aligned} 0 \leq D^{\mathrm{TV}}_{-A^* w^\dagger}(u, u^\dagger) &:= \mathrm{TV}(u) - \mathrm{TV}(u^\dagger) - \langle -A^* w^\dagger, u - u^\dagger \rangle \\ &= \mathrm{TV}(u) - \mathrm{TV}(u^\dagger) + \langle w^\dagger, Au - Au^\dagger \rangle = \mathrm{TV}(u) - \mathrm{TV}(u^\dagger) \leq 0, \end{aligned}$$

since $Au = Au^\dagger$ and u is a minimizer of TV. The one-homogeneity of TV now implies $\mathrm{TV}(u^\dagger) = \langle -A^* w^\dagger, u^\dagger \rangle$ so that

$$0 = D^{\mathrm{TV}}_{-A^* w^\dagger}(u, u^\dagger) = \mathrm{TV}(u) - \langle -A^* w^\dagger, u \rangle = \mathrm{M}(\partial_x u) - \langle \varphi_1, \partial_x u \rangle + \mathrm{M}(\partial_y u) - \langle \varphi_2, \partial_y u \rangle.$$

Thus, since $|\varphi_1|, |\varphi_2| < 1$ away from the support of $\partial_x u^\dagger$ and $\partial_y u^\dagger$, $\partial_x u$ and $\partial_y u$ must have the same support. (In the point mass setting the argument would be almost identical with u, $u^\dagger$ replaced by ρ, $\rho^\dagger$ and TV by M.)

To prove that the actual values of u and $u^\dagger$ coincide, one needs to show that the *error* $u - u^\dagger$ satisfies a similar source condition as $u^\dagger$, followed by a similarly simple argument (the point mass setting would proceed analogously).

The error estimates in the noisy case derive from quantitative refinements of the above, which require that the functions $|\varphi_1|, |\varphi_2|$ from the source condition decay quickly enough away from the supports S_x of $\partial_x u^\dagger$ and S_y of $\partial_y u^\dagger$, respectively. As smooth functions (linear combinations of Fejér kernels), φ_1 and φ_2 indeed behave like parabolas near S_x and S_y, which leads to the occurrence of squared distances to S_x and S_y in the quantitative estimates and thereby to Wasserstein-2-type error estimates. Those can finally be turned into L^1-type estimates by the following one-dimensional norm interpolation result.

Lemma ([4]). *If a function v of bounded variation on $(0,1)$ satisfies $v(1) = 0$ in the trace-sense, then $\|v\|^2_{L^1} \leq \mathrm{M}(\partial_x v)\mathrm{M}(\mathrm{dist}^2(0,x)\partial_x v)$.*

References

[1] Y. de Castro and F. Gamboa, *Exact reconstruction using beurling minimal extrapolation*, Journal of Mathematical Analysis and Applications **395**(1) (2012), 336–354.

[2] E. J. Candès and C. Fernandez-Granda *Towards a mathematical theory of super-resolution*, Communications on Pure and Applied Mathematics **67**(6) (2014), 906–956.
[3] Q. Denoyelle, V. Duval, G. Peyré, *Support recovery for sparse super-resolution of positive measures*, Journal of Fourier Analysis and Applications **23**(5) (2017), 1153–1194.
[4] M. Holler, B. Wirth, *Exact reconstruction and reconstruction from noisy data with anisotropic total variation*, arXiv:2206.02908 (2022).

Translation invariant diagonal frame decomposition for the Radon transform

Jürgen Frikel
(joint work with Simon Göppel, Markus Haltmeier)

Frame-based regularization methods have become one of the standard technique for solving ill-posed inverse problems due to their ability to simultaneously adapt to the operator and the signal class (a-priori information). In particular, regularization methods based on diagonal frame decomposition (DFD) of linear operators have been developed and analyzed recently, see for example [5, 10]. The Radon transform has been a popular example in this context, since several DFDs are available in the literature, such as wavelet-vaguelette decompositions [4], and DFDs based on curvelets and shearlets, cf. [1, 3]. However, existing DFDs often lack translation invariance, which is crucial for efficient denoising, cf. [2].

In this work, we introduce a translation-invariant DFD framework (TI-DFD) for solving ill-posed reconstruction problems in computed tomography and present the construction of a translation-invariant diagonal frame decomposition of the Radon transform $\mathcal{R} : L^2(\mathbb{R}^2) \to L^2(\mathbb{Y})$, with $\mathbb{Y} := S^1 \times \mathbb{R}^2$, as a densely defined and closed operator. For more details we refer to [8, 9].

Translation invariant frame decompositions.

Definition 1. *Let Λ be an at most countable index set. A family $(u_\lambda)_{\lambda\in\Lambda} \in L^2(\mathbb{R}^2)^\Lambda$ is called a translation invariant frame (TI-frame) for $L^2(\mathbb{R}^2)$ if $\hat{u}_\lambda \in L^\infty(\mathbb{R}^2)$ for all $\lambda \in \Lambda$ and there exist constants $A, B > 0$, such that*

$$\forall f \in L^2(\mathbb{R}^2): \quad A\|f\|^2 \le \sum_{\lambda\in\Lambda} \|u_\lambda^* * f\|^2 \le B\|f\|^2 . \tag{1}$$

A TI-frame $(u_\lambda)_{\lambda\in\Lambda}$ is called tight if (1) holds with TI-frame founds $A = B = 1$.

For every TI frame element u_λ, we define the canonical dual frame element via

$$w_\lambda := \mathcal{F}^{-1}(2\pi\widehat{u}_\lambda / \sum_{\mu\in\Lambda} |\widehat{u}_\mu|^2),$$

where $\widehat{u}_\mu$ denotes the Fourier transform of u_μ and $\mathcal{F}^{-1}$ denotes the inverse Fourier transform. The resulting frame $(w_\lambda)_{\lambda\in\Lambda}$ is called the canonical dual of $(u_\lambda)_{\lambda\in\Lambda}$, and for every $f \in L^2(\mathbb{R}^2)$ it holds that

$$f = \sum_{\lambda\in\Lambda} w_\lambda * (u_\lambda^* * f), \tag{2}$$

where $u_\lambda^*(x) := \overline{u(-x)}$ and $\bar{z}$ denotes the complex conjugate of $z \in \mathbb{C}$.

Generalizing the notion of the DFD (cf. [5]) we arrive at the following definition of the translation invariant version of the DFD (cf. [9]).

Definition 2 (TI-DFD). *Let $B(\mathbb{Y}, L^2(\mathbb{R}^2))$ denote the space of bounded operators between $\mathbb{Y}$ and $L^2(\mathbb{R}^2)$. We call the system $(u_\lambda, \mathcal{V}_\lambda^*, \kappa_\lambda)_{\lambda\in\Lambda}$ a translation invariant frame decomposition (TI-DFD) for $\mathcal{R}$, if the following properties hold:*

(TI1) $(u_\lambda)_{\lambda\in\Lambda} \in L^2(\mathbb{R}^2)^\Lambda$ is a TI-frame for $L^2(\mathbb{R}^2)$.

(TI2) $\forall\lambda \in \Lambda: \ \mathcal{V}_\lambda^* \in B(\mathbb{Y}, L^2(\mathbb{R}^2))$ and $\forall g \in \overline{\operatorname{ran}\mathcal{R}}$: $\sum_{\lambda\in\Lambda}\|\mathcal{V}_\lambda^* g\|^2 \asymp \|g\|$.

(TI3) $\forall\lambda \in \Lambda$: $\kappa_\lambda \in (0,\infty)$ and $\forall f \in \operatorname{dom}(\mathcal{R})$: $\mathcal{V}_\lambda^*(\mathcal{R}f) = \kappa_\lambda\,(u_\lambda^* * f)$.

Here, $f \asymp g :\Leftrightarrow \exists c, C > 0$: $c\|g\| \le \|f\| \le C\|g\|$.

Filter-based TI-DFD regularization methods. In what follows, a family $(\Phi_\alpha)_{\alpha>0}$ of bounded and piecewise continuous functions $\Phi_\alpha : (0,\infty) \to \mathbb{R}$ is called a *regularizing filter*, if the following properties hold:

(F1) $\exists C > 0 : \ \sup\limits_{\alpha,t>0} |t\Phi_\alpha(t)| \le C$,

(F2) $\forall t > 0 : \ \lim\limits_{\alpha\to 0} \Phi_\alpha(t) = \frac{1}{t}$.

We quote the following central result, the proof of which can be found in [9].

Theorem 3. *Let $(u_\lambda, \mathcal{V}_\lambda^*, \kappa_\lambda)_{\lambda\in\Lambda}$ be a TI-DFD for $\mathcal{R}$ and $(w_\lambda)_{\lambda\in\Lambda}$ be a dual TI-frame for $(u_\lambda)_{\lambda\in\Lambda}$. Then,*

$$\forall g \in \operatorname{ran}(\mathcal{R}): \quad \mathcal{R}^{-1}g = \sum_{\lambda\in\Lambda} w_\lambda * (\kappa_\lambda^{-1} \cdot (\mathcal{V}_\lambda^* g)). \tag{3}$$

Furthermore, for a regularizing filter $(\Phi_\alpha)_{\alpha>0}$, the family of operators $(\mathcal{R}_\alpha^\Phi)_{\alpha>0}$, given by

$$\mathcal{R}_\alpha^\Phi g := \sum_{\lambda\in\Lambda} w_\lambda * (\Phi_\alpha(\kappa_\lambda) \cdot (\mathcal{V}_\lambda^* g)) \tag{4}$$

defines a regularization method (for definition see [6]).

The equation(3) reveals the ill-posedness of the reconstruction problem and links it to the decay rate of the quasi-singular values κ_λ. Moreover, once a TI-DFD is available for $\mathcal{R}$, this result provides a way to construct regularization methods from a given regularizing filter (examples of regularizing filters can be found, e.g., in [6, 9]). In the next paragraph, we explain how TI-DFDs can be constructed for the Radon transform.

Filter-based TI-DFD regularization methods. The following result shows how to construct a TI-DFD for the Radon transform starting from a given TI-wavelet frame for $L^2(\mathbb{R}^2)$. We recall that the Riesz transform $\mathcal{I}^1$ of a suitably chosen function $g : \mathbb{Y} \to \mathbb{R}$ is defined via the Fourier transform $\mathcal{F}$ as $\mathcal{I}^1 g(\theta,\cdot) := \mathcal{F}^{-1}(|\cdot|\mathcal{F}g(\theta,\cdot)))$.

Theorem 4. *Let $(u_j)_{j\in\mathbb{Z}}$ be a TI-frame of $L^2(\mathbb{R}^2)$, given by $u_{j,l}(x) = 2^j u_{0,l}(2^j x)$, $(j,l) \in \mathbb{Z} \times \{H, V, L\}$, such that $\operatorname{supp}(\widehat{u}_{0,l}) \subseteq \{\omega \in \mathbb{R} : \ a \le |\omega| \le b\}$ for some*

$a, b > 0$. *For* $(j,l) \in \mathbb{Z} \times \{H, V, L\}$, *we define*

$$v_{j,l} := 2^{-j/2} \mathcal{I}^1 \mathcal{R} u_{j,l}(x) \quad \text{and} \quad \mathcal{V}^*_{j,l}(g) := \mathcal{R}^*(v^*_{j,l} * g).$$

Then, the family $(u_{j,l}, \mathcal{V}^*_{j,l}, 2^{-j/2})_{j \in \mathbb{Z} \times \{H,V,L\}}$ *is a TI-WVD for the Radon transform* $\mathcal{R}$.

The proof of this theorem can be found in [8].

REFERENCES

[1] E. J. Candés and D. L. Donoho. *Recovering edges in ill-posed inverse problems: optimality of curvelet frames.* Ann. Statist., Vol. 30, Nr. 3, pp. 784–842, 2002

[2] R. R. Coifman and D. L. Donoho, *Translation-Invariant De-Noising.* In: Antoniadis, A., Oppenheim, G. (eds) Wavelets and Statistics. Lecture Notes in Statistics, Vo. 103. Springer, New York, NY. https://doi.org/10.1007/978-1-4612-2544-7_9

[3] F. Colonna, G. Easley, K. Guo and D. Labate. *Radon transform inversion using the shearlet representation.* Appl. Comput. Harmon. Anal., Vol. 29, pp. 232–250, 2010. https://doi.org/10.1016/j.acha.2009.10.005

[4] D. L. Donoho. *Nonlinear solution of linear inverse problems by wavelet-vaguelette decomposition.* Appl. Comput. Harmon. Anal., Vol. 2, pp. 101–126, 1995. https://doi.org/10.1006/acha.1995.1008

[5] A. Ebner, J. Frikel, D. Lorenz, J. Schwab and M. Haltmeier. *Regularization of inverse problems by filtered diagonal frame decomposition.* Appl. Comput. Harmon. Anal., Vol. 62, pp. 66–83, 2023. https://doi.org/10.1016/j.acha.2022.08.005

[6] H. W. Engl, M. Hanke and A. Neubauer. *Regularization of inverse problems*, Mathematics and its Applications. Kluwer Academic Publishers Group, Dordrecht, Volume 375, viii+321, 1996.

[7] J. Frikel and M.Haltmeier. *Sparse regularization of inverse problems by operator-adapted frame thresholding.* In Mathematics of Wave Phenomena, pp. 163–178, Springer International Publishing (Cham), 2020. https://doi.org/10.1007/978-3-030-47174-3

[8] S. Göppel, J. Frikel and M. Haltmeier. *Translation invariant diagonal frame decomposition for the Radon transform.* Proceedings of the 14th International conference on Sampling Theory and Applications, to appear.

[9] S. Göppel, J. Frikel and M. Haltmeier. *Translation invariant diagonal frame decomposition of inverse problems and their regularization.* Inverse Problems, Vol. 39, Nr. 6, pp. 065011, 2023. https://doi.org/10.1088/1361-6420/accd15

[10] S. Hubmer, R. Ramlau, and L. Weissinger. *On regularization via frame decompositions with applications in tomography.* Inverse Problems, Vol. 38, Nr. 5, pp. 055003, 2022. https://doi.org/10.1088/1361-6420/ac5b86

Reconstruction From Discrete 2D Radon Transform Data – Resolution and Aliasing

ALEXANDER KATSEVICH

Resolution of image reconstruction from discrete data is one of the fundamental questions in imaging. The most direct approach to estimating resolution utilizes the notions of the point spread function (PSF) and modulation transfer function

(MTF) [1, Sections 12.2, 12.3]. This and other similar approaches allow rigorous theoretical analysis of only the simplest settings, such as inversion of the classical Radon transform. For the most part, resolution of reconstruction in more difficult settings (e.g., inversion of the cone beam transform) is analyzed by heuristic arguments, numerically, or via measurements [2–4].

Sampling theory provides another approach to investigating resolution [7, 12]. Consider, for example, the classical Radon transform in $\mathbb{R}^2$

$$\hat{f}(\alpha,p)=\int_{\mathbb{R}^2} f(x)\delta(\vec{\alpha}\cdot x-p)\mathrm{d}x,\ \vec{\alpha}=(\cos\alpha,\sin\alpha). \tag{1}$$

The corresponding discrete data are

$$\hat{f}(\alpha_k,p_j),\ \alpha_k=\bar{\alpha}+k\Delta\alpha,\ p_j=\bar{p}+j\Delta p,\ \alpha_k\in[0,2\pi), j\in\mathbb{Z}, \tag{2}$$

for some fixed $\bar{\alpha}$, $\bar{p}$ and $\Delta\alpha$, Δp. Assume that f is essentially band-limited (in the classical sense). This means that, with high accuracy, its Fourier transform $\tilde{f}(\xi)$ is supported in some ball $|\xi|\le B$. The sampling theory predicts the rates $\Delta\alpha$, Δp with which $\hat{f}(\alpha,p)$ should be sampled, so that reconstruction of f from discrete data does not contain aliasing artifacts. Since the essential band-limit B is related to the size of the smallest detail in f, a typical prescription of the theory can be loosely formulated as follows: given the size of the smallest detail in f, the minimal sampling rates to avoid aliasing are $\Delta\alpha$, Δp. Alternatively, the theory determines the size of the smallest detail in f that can be resolved given the rates $\Delta\alpha$, Δp. A microlocal approach to sampling was developed recently [15–17]. In this approach f is assumed to be band-limited in the semiclassical sense (i.e., the semiclassical wavefront set $\mathrm{WF}_h(f)$ is compact). The goal is to accurately recover the semiclassical singularities of f and avoid aliasing. If the sampling requirement is violated, the theory predicts the location and frequency of the aliasing artifacts.

In [18–22], the author developed an analysis of resolution (we call it Local Resolution Analysis, or LRA), which addresses the question of resolution head on. The main results in these papers are simple expressions describing the reconstruction from discrete data in a neighborhood of the singularities of f in a variety of settings. We call these expressions the Discrete Transition Behavior (DTB). The DTB provides the most direct, fully quantitative link between the sampling rate and resolution. In these papers such a link is established for a wide range of integral transforms, conormal distributions f, and reconstruction operators. In [23,24] LRA was generalized to objects with rough boundaries in $\mathbb{R}^2$.

Suppose $\Delta p=\epsilon$ and $\Delta\alpha=\kappa\epsilon$, where $\kappa>0$ is fixed. The DTB is an accurate approximation of the reconstruction in an ϵ-neighborhood of the singular support of f in the limit as $\epsilon\to 0$. Therefore, the DTB provides much more than a single measure of resolution (e.g., the size of the smallest detail that can be resolved). Given the DTB function, the user may decide in a fully quantitative way what sampling rate is required to achieve the user-defined reconstruction quality. The notion of quality may include resolution (which can be described in any desired way) and/or any other requirement the user desires. Thus, the LRA answers precisely the question of the required sampling rate to guarantee the required resolution (understood broadly). No assumption that f be band-limited (either classically or semiclassically) is required.

In practice f is almost never band-limited, so aliasing artifacts arise regardless of the sampling rate. Some earlier results on the analysis of aliasing artifacts (more precisely, view aliasing artifacts) are in [25] and [1, Section 12.3.2]. They include an approximate formula for the artifacts far from a small, radially symmetric object. More recent results are in [15–17]. These include the prediction of the location and frequency of the artifacts, qualitative analysis of the artifacts generated by various edges (e.g., flat, convex, and a corner), as well as their numerical illustrations.

In this talk we generalize the LRA to the analysis of view aliasing. We call it the Local Aliasing Analysis, or LAA. Our main result is a precise, quantitative formula describing aliasing artifacts. The formula is asymptotic, it is established in the limit as the sampling rate $\epsilon \to 0$ (which is the same assumption as in [15–17]). Similarly to the LRA, the LAA is very flexible. In this talk we consider the generalized Radon transform in $\mathbb{R}^2$ and apply it to functions with jump discontinuities across smooth, convex curves. Similarly to [18–22], we believe that the LAA is generalizable, and that it is capable of predicting aliasing artifacts for a wide range of integral transforms, conormal distributions f, and reconstruction operators.

REFERENCES

[1] C. L. Epstein, *Introduction to the mathematics of medical imaging*. Philadelphia: SIAM, second ed., 2008.

[2] B. Li, G. B. Avinash, and J. Hsieh, "Resolution and noise trade-off analysis for volumetric CT," *Medical Physics*, vol. 34, no. 10, pp. 3732–3738, 2007.

[3] R. Grimmer, J. Krause, M. Karolczak, R. Lapp, and M. Kachelrie, "Assessment of spatial resolution in CT," *IEEE Nuclear Science Symposium Conference Record*, pp. 5562–5566, 2008.

[4] S. N. Friedman, G. S. Fung, J. H. Siewerdsen, and B. M. Tsui, "A simple approach to measure computed tomography (CT) modulation transfer function (MTF) and noise-power spectrum (NPS) using the American College of Radiology (ACR) accreditation phantom," *Medical Physics*, vol. 40, no. 5, pp. 1–9, 2013.

[5] H. Kruse, "Resolution of Reconstruction Methods in Computerized Tomography," *SIAM Journal on Scientific and Statistical Computing*, vol. 10, pp. 447–474, 1989.

[6] L. Desbat, "Efficient sampling on coarse grids in tomography," *Inverse Problems*, vol. 9, pp. 251–269, 1993.

[7] F. Natterer, "Sampling in Fan Beam Tomography," *SIAM Journal on Applied Mathematics*, vol. 53, pp. 358–380, 1993.

[8] F. Natterer, "Sampling and resolution in CT," in *Proceedings of the Fourth International Symposium (CT-93): Novosibirsk, 1993* (M. M. Lavrentév, ed.), pp. 343–354, Utrecht: VSP, 1995.

[9] V. P. Palamodov, "Localization of harmonic decomposition of the Radon transform," *Inverse Problems*, vol. 11, pp. 1025–1030, 1995.

[10] A. Caponnetto and M. Bertero, "Tomography with a finite set of projections: singular value decomposition and resolution," *IEEE Transactions on Information Theory*, vol. 13, pp. 1191–1205, 1997.

[11] A. Faridani and E. Ritman, "High-resolution computed tomography from efficient sampling," *Inverse Problems*, vol. 16, pp. 635–650, 2000.

[12] A. Faridani, "Sampling theory and parallel-beam tomography," in *Sampling, wavelets, and tomography*, vol. 63 of *Applied and Numerical Harmonic Analysis*, pp. 225–254, Boston, MA: Birkhauser Boston, 2004.

[13] A. Rieder and A. Schneck, "Optimality of the fully discrete filtered backprojection algorithm for tomographic inversion," *Numerische Mathematik*, vol. 108, pp. 151–175, 2007.

[14] S. H. Izen, "Sampling in Flat Detector Fan Beam Tomography," *SIAM Journal on Applied Mathematics*, vol. 72, pp. 61–84, 2012.

[15] P. Stefanov, "Semiclassical sampling and discretization of certain linear inverse problems," *SIAM Journal of Mathematical Analysis*, vol. 52, pp. 5554–5597, 2020.

[16] F. Monard and P. Stefanov, "Sampling the X-ray transform on simple surfaces," *ArXiv ID:2110.05761*, 2021.

[17] P. Stefanov, "The Radon transform with finitely many angles," *arXiv:2208.05936v1*, pp. 1–30, 2022.

[18] A. Katsevich, "A local approach to resolution analysis of image reconstruction in tomography," *SIAM Journal on Applied Mathematics*, vol. 77, no. 5, pp. 1706–1732, 2017.

[19] A. Katsevich, "Analysis of reconstruction from discrete Radon transform data in $\mathbb{R}^3$ when the function has jump discontinuities," *SIAM Journal on Applied Mathematics*, vol. 79, pp. 1607–1626, 2019.

[20] A. Katsevich, "Analysis of resolution of tomographic-type reconstruction from discrete data for a class of distributions," *Inverse Problems*, vol. 36, no. 12, 2020.

[21] A. Katsevich, "Resolution analysis of inverting the generalized Radon transform from discrete data in $\mathbb{R}^3$," *SIAM Journal of Mathematical Analysis*, vol. 52, no. 4, pp. 3990–4021, 2020.

[22] A. Katsevich, "Resolution analysis of inverting the generalized N-dimensional Radon transform in $\mathbb{R}^n$ from discrete data," *Journal of Fourier Analysis and Applications*, vol. 29, art. 6, 2023.

[23] A. Katsevich, "Resolution of 2D reconstruction of functions with nonsmooth edges from discrete Radon transform data," *SIAM Journal on Applied Mathematics*, vol. to appear, 2023.

[24] A. Katsevich, "Novel resolution analysis for the Radon transform in $\mathbb{R}^2$ for functions with rough edges," *arXiv:2206.04545*, pp. 1–32, 2022.

[25] P. M. Joseph and R. A. Schulz, "View sampling requirements in fan beam computed tomography," *Medical Physics*, vol. 7, no. 6, pp. 692–702, 1980.

Weighted Radon transforms of vector fields, with applications to magnetoacoustoelectric tomography

LEONID KUNYANSKY

(joint work with E. McDugald and B. Shearer)

We study unweighted and linearly weighted Radon transforms of vector fields. There is a significant body of work on ray transforms of vector and tensor fields [1, 2, 4, 5, 8–10]. However, there are very few publications on the Radon transforms of vector fields [6, 7], with considerations usually restricted to unweighted transforms of potential fields with finitely supported potentials. Here we consider general vector fields (i.e. not purely potential or solenoidal), and we study both unweighted and linearly weighted Radon transforms.

An important tool we use is the Helmholtz decomposition. We work with transversal and longitudinal Radon transforms of the potential and solenoidal parts F^{p} and F^{s} of a general vector field F. The known estimates of the rates of decay of F^{p} and F^{s} at infinity [8] do not guarantee the convergence of the Radon transforms, so we provide improved estimates, that imply the existence of the Radon transforms of the above types.

The longitudinal Radon transforms of a potential field vanish, as does the transversal transform of a solenoidal field. Therefore, reconstructing a general vector field from only the longitudinal or only the transversal transform(s) is not possible. If one of the transform types (longitudinal or transversal) cannot be measured, we assume the knowledge of weighted transforms of the available type.

We present explicit formulas for solving two distinct problems. The first problem is that of reconstructing a general vector field from known values of its transversal transform, and from $d-1$ weighted transversal transforms with linear weights. The second problem (motivated by MAET) is the reconstruction of a vector field from $d-1$ of its longitudinal transforms and one weighted longitudinal transform with a linear weight. The reader is advised to compare our solutions to the results of [2], where a full vector field is reconstructed from a ray transform and a first-moment ray transform.

Consider a continuous function $f(x)$ defined in $\mathbb{R}^d$, subject to the condition $f(x) = \mathcal{O}\left(|x|^{-d}\right)$ at infinity. Define a hyperplane $\Pi(\omega, p)$ by the equation $\omega \cdot x = p$, where $\mathbb{S}^{d-1}$ is the unit sphere in $\mathbb{R}^d$, and $(\omega, p) \in \mathbb{S}^{d-1} \times \mathbb{R}$. The Radon transform $\mathcal{R}f$ is defined as the set of integrals of f over all the hyperplanes:

$$[\mathcal{R}f](\omega, p) \equiv \int\limits_{\Pi(\omega,p)} f(x)\, dA_{\Pi}(x), \quad (\omega, p) \in \mathbb{S}^{d-1} \times \mathbb{R},$$

where $dA_{\Pi}(x)$ is the standard area element on $\Pi(\omega, p)$. Properties of the Radon transform are traditionally studied for functions $f(x)$ from the Schwartz class $\mathcal{S}(\mathbb{R}^d)$. A function $f(x) \in \mathcal{S}(\mathbb{R}^d)$ can be reconstructed from its projections $g = \mathcal{R}f$ using the well known filtered backprojection inversion formula [3]:

$$f = \mathcal{R}^{-1}(g) \equiv \frac{1}{2}(2\pi)^{1-d} I^{-\alpha} \mathcal{R}^{\#} I^{\alpha-d+1} g, \tag{1}$$

where $\mathcal{R}^{\#}$ is the dual Radon transform that acts on a function $g(\omega, p)$ defined on $\mathbb{S}^{d-1} \times \mathbb{R}$ according to the formula

$$[\mathcal{R}^{\#} g](x) = \int\limits_{\mathbb{S}^{d-1}} g(\omega, \omega \cdot x) d\omega,$$

and where $I^{\alpha} f$ is the Riesz potential of a function f.

Let us consider now a continuous vector field $F(x) = (F_1(x), ..., F_d(x))$ defined on $\mathbb{R}^d$, $d \geq 2$, whose components decay fast enough for the existence of integrals over each hyperplane (e.g., $|F(x)| = \mathcal{O}\left(|x|^{-d}\right)$). Below we define several types of Radon transforms of such a field.

The componentwise Radon transform $\mathfrak{R}F$ of F is defined in the obvious way:

$$[\mathfrak{R}F](\omega, p) \equiv (\mathcal{R}\mathcal{F}_1, .., \mathcal{R}\mathcal{F}_d)(\omega, p), \qquad (\omega, p) \in \mathbb{S}^{d-1} \times \mathbb{R}.$$

The transversal Radon transform $\mathcal{D}^{\perp}F$ is the Radon transform of the projection of F onto the normal ω to the plane $\Pi(\omega,p)$:

$$\left[\mathcal{D}^{\perp}F\right](\omega,p) \equiv \int\limits_{\Pi(\omega,p)} \omega\cdot F(x)\,dA_{\Pi}(x) = \left[\mathcal{R}(\omega\cdot F(x))\right](\omega,p).$$

For each fixed direction $\omega\in\mathbb{S}^{d-1}$, let us arbitrarily extend ω to an orthonormal basis $\mathfrak{B}=(\omega,\omega_1,...,\omega_{d-1})$ of $\mathbb{R}^d$, where $\omega_j=\omega_j(\omega)$, $j=1,...,d-1$. To simplify the notation, below we will suppress the dependence of ω_j's on ω. Define the longitudinal Radon transforms $\mathcal{D}^{\shortparallel}_kF$ of F, $k=1,...d-1$, as follows:

$$\left[\mathcal{D}^{\shortparallel}_kF\right](\omega,p) \equiv \int\limits_{\Pi(\omega,p)} \omega_k\cdot F(x)\,dA_{\Pi}(x) = \left[\mathcal{R}(\omega_k\cdot F(x))\right](\omega,p),.$$

For a faster decaying vector field $F(x)$ (e.g. satisfying $|F(x)|=\mathcal{O}\left(|x|^{-d-1}\right)$), one can define the weighted transversal transforms $\mathcal{W}^{\perp}_k$ and longitudinal transforms $\mathcal{W}^{\shortparallel}_k$ with linear weights $\omega_k\cdot x$, $k=1,...d-1$, by the following expressions:

$$\mathcal{W}^{\perp}_kF \equiv \int\limits_{\Pi(\omega,p)} (\omega_k\cdot x)F(x)\cdot\omega\,dA_{\Pi}(x) = \mathcal{D}^{\perp}((\omega_k\cdot x)F(x)), \quad (\omega,p)\in\mathbb{S}^{d-1}\times\mathbb{R},$$

$$\mathcal{W}^{\shortparallel}_kF \equiv \int\limits_{\Pi(\omega,p)} (\omega_k\cdot x)F(x)\cdot\omega_k\,dA_{\Pi}(x) = \mathcal{D}^{\shortparallel}_k((\omega_k\cdot x)F(x)), \quad (\omega,p)\in\mathbb{S}^{d-1}\times\mathbb{R}.$$

The present definitions of the unweighted longitudinal and transversal Radon transforms coincide with those given in [9, 11] (where they are mentioned under the names of "probe" and "normal" transforms, respectively). Our definitions of the weighted transforms appear to be new; they naturally extend the notion of "moments ray transforms" [2, 11] to the case of Radon transforms. Obviously

$$\left[\mathcal{D}^{\perp}F\right](\omega,p)=\omega\cdot\left[\mathfrak{R}F\right](\omega,p), \quad \left[\mathcal{D}^{\shortparallel}_kF\right](\omega,p)=\omega_k\cdot\left[\mathfrak{R}F\right](\omega,p).$$

Consider a vector field $F(x)$ with each component $F_m(x)$ lying in the Schwartz space $\mathcal{S}(\mathbb{R}^d)$. Define the potential φ as the convolution of the divergence Φ of F with the fundamental solution G of the Laplace equation in $\mathbb{R}^d$:

$$\varphi(x)=(\Phi*G)(x)=\int\limits_{\mathbb{R}^d}\Phi(y)G(x-y)dy, \qquad \Phi(x)=\operatorname{div}F(x), \qquad x\in\mathbb{R}^d. \tag{2}$$

Now the potential and solenoidal parts F^{p}, F^{s} are defined as:

$$F^{\mathrm{p}}(x)=\nabla\varphi(x), \qquad F^{\mathrm{s}}(x)=F(x)-F^{\mathrm{p}}(x), \qquad x\in\mathbb{R}^d. \tag{3}$$

Theorem 1. *Suppose that each component $F_k(x)$, $k=1,...,d$ of a vector field $F(x)$ is a function from the Schwartz class $\mathcal{S}(\mathbb{R}^d)$. Then potential φ and fields F^{p} and F^{s} given by equations (2)-(3) have the following decay rates at infinity*

(4)

$$|F^{\cdots}(x)|=\mathcal{O}\left(\frac{1}{|x|^d}\right), \left|\frac{\partial}{\partial x_j}F^{\cdots}(x)\right|=\mathcal{O}\left(\frac{1}{|x|^{d+1}}\right), \left|\frac{\partial^2}{\partial x_j\partial x_k}F^{\cdots}(x)\right|=\mathcal{O}\left(\frac{1}{|x|^{d+2}}\right),$$

where $F^{\cdots}$ stands for either F^{p} or F^{s}, $k = 1, 2, ..., d$. The above estimates guarantee existence of the various Radon transforms of F^{p} and F^{s}, so that

$$\mathfrak{R}F = \mathfrak{R}F^{\mathrm{p}} + \mathfrak{R}F^{\mathrm{s}}, \quad \mathcal{D}^{\perp}F = \mathcal{D}^{\perp}F^{\mathrm{p}} + \mathcal{D}^{\perp}F^{\mathrm{s}}, \quad \mathcal{D}^{\shortparallel}_{k}F = \mathcal{D}^{\shortparallel}_{k}F^{\mathrm{p}} + \mathcal{D}^{\shortparallel}_{k}F^{\mathrm{s}},$$

with $k = 1, 2, ..., d - 1$. Transforms $\mathcal{W}^{\shortparallel}_{k}F^{\mathrm{p}}$, $\mathcal{W}^{\shortparallel}_{k}F^{\mathrm{s}}$, $\mathcal{W}^{\perp}_{k}F^{\mathrm{p}}$, and $\mathcal{W}^{\perp}_{k}F^{\mathrm{s}}$ cannot be defined, in general. Our main results are the following two theorems:

Theorem 2. *If an infinitely differentiable vector field $F(x) = (F_1(x), ..., F_d(x))$ satisfies decay conditions (4), its divergence Φ can be reconstructed from the transversal transform $\mathcal{D}^{\perp}F$ by applying the inversion formula (1) as follows*

$$\Phi(x) = \left[\mathcal{R}^{-1}\left(\frac{\partial}{\partial p}\mathcal{D}^{\perp}F\right)\right](x), \qquad x \in \mathbb{R}^d.$$

The componentwise transform of $\mathfrak{R}F$ can be reconstructed from $\mathcal{D}^{\perp}F$ and weighted transversal transforms $\mathcal{W}^{\perp}_{k}F$, $k = 1, .., d - 1$, as follows:

$$[\mathfrak{R}F](\omega, p) = \omega[\mathcal{D}^{\perp}F](\omega, p) + \sum_{k=1}^{d-1}\omega_k\left(\frac{\partial}{\partial p}[\mathcal{W}^{\perp}_{k}F](\omega, p) - [\mathcal{R}\{(\omega_k \cdot x)\Phi(x)\}](\omega, p)\right)$$

where $(\omega, p) \in \mathbb{S}^{d-1}\times\mathbb{R}$, $j = 1, 2, ..., d$. Finally, field F can be recovered by inverting $\mathfrak{R}F$ componentwise:

$$F_j(x) = \mathcal{R}^{-1}\left(e_j \cdot \mathfrak{R}F\right)(x), \qquad x \in \mathbb{R}^d, \qquad j = 1, 2, ..., d,$$

where vectors $e_{1,}e_2, ..., e_d$ form the canonical orthonormal basis in $\mathbb{R}^d$, and where $\mathcal{R}^{-1}$ is understood as the filtration/backprojection formula (1).

In order to formulate the next theorem, let us denote by Ψ the componentwise Laplacian Ψ of the solenoidal part of the field F^{s}:

$$\Psi(x) \equiv (\Psi_1(x), \Psi_2(x), ..., \Psi_d(x)), \quad \Psi_j(x) = \Delta F^s_j(x), \quad x \in \mathbb{R}^d, \quad j = 1, .., d.$$

Theorem 3. *If an infinitely differentiable vector field $F(x) = (F_1(x), ..., F_d(x))$ satisfies decay conditions (4), the componentwise Laplacian Ψ of its solenoidal part F^{s} and the Radon transform of Ψ can be reconstructed from longitudinal transforms $\mathcal{D}^{\shortparallel}_{j}F$, $j = 1, ..., d - 1$, using the following formulas:*

$$[\mathfrak{R}\Psi](\omega, p) = \frac{\partial^2}{\partial p^2}\sum_{j=1}^{d-1}\omega_j[\mathcal{D}_j{}''F](\omega, p), \quad \Psi_j(x) = \left[\mathcal{R}^{-1}\left(e_j \cdot \mathfrak{R}\Psi\right)\right](x), \quad x \in \mathbb{R}^d.$$

Further, the divergence Φ of the field can be reconstructed from the linearly weighted longitudinal transform $\mathcal{W}^{\shortparallel}_{1}F$ and previously found Ψ as follows:

$$\Phi(x) = \mathcal{R}^{-1}\{\mathcal{R}((x \cdot \omega_1)\omega_1 \cdot \Psi(x)) - \frac{\partial^2}{\partial p^2}\mathcal{W}^{\shortparallel}_{1}F\}, \qquad x \in \mathbb{R}^d,$$

where $\mathcal{R}^{-1}$ is understood as the filtration/backprojection formula (1). Field F is reconstructed from Φ and Ψ by convolving these functions with G and ∇G:

$$F(x) = (\Phi * \nabla G)(x) + \sum_{j=1}^{d} e_j(\Psi_j * G)(x), \quad x \in \mathbb{R}^d.$$

REFERENCES

[1] Krishnan V P, Manna R, Sahoo S-K and Sharafutdinov V A 2019 Momentum ray transforms *Inverse Problems and Imaging* **13**(3) 679–701

[2] Mishra R K 2020 Full reconstruction of a vector field from restricted Doppler and first integral moment transforms in $\mathbb{R}^n$ *Journal of Inverse and Ill-posed Problems* **28**(2) 173–184

[3] Natterer F 2001 *The Mathematics of Computerized Tomography (Classics in Applied Mathematics)* (Society for Industrial Mathematics) p 184

[4] Norton S J 1989 Tomographic reconstruction of 2-d vector fields: application to flow imaging *Geophysical Journal International* **97**(1) 161–168

[5] Norton S J 1992 Unique tomographic reconstruction of vector fields using boundary data *IEEE Transactions on image processing* **1**(3) 406–412

[6] Polyakova A 2015 Reconstruction of a vector field in a ball from its normal Radon transform *Journal of Mathematical Sciences* **205**(3) 418-439

[7] Polyakova A P and Svetov I E 2015 Numerical solution of the problem of reconstructing a potential vector field in the unit ball from its normal Radon transform. *Journal of Applied and Industrial Mathematics* **9**(4) 547–558

[8] Sharafutdinov V A 2012 *Integral geometry of tensor fields*, volume 1. (Walter de Gruyter)

[9] Schuster T 2008 20 years of imaging in vector field tomography: a review *Mathematical Methods in Biomedical Imaging and Intensity-Modulated Radiation Therapy (IMRT)*, volume 7. (CRM), Birkhäuser

[10] Sparr G and Stråhlén K 1999 Vector field tomography: an overview *IMA Volumes in Mathematics and its Applications; Computational Radiology and Imaging: Therapy and Diagnostic* 110

[11] Stråhlén K 1997 Exponential vector field tomography *International Conference on Image Analysis and Processing*, (Springer) 348–355

Injectivity and stability of the inversion of the star transform

GAIK AMBARTSOUMIAN

(joint work with Mohammad J. Latifi)

The star transform is a generalized Radon transform mapping a function (or, more generally, a tensor field) to its integrals along "star-shaped" trajectories, which consist of a finite number of rays emanating from a common vertex. Such operators appear in mathematical models of various imaging modalities based on scattering of elementary particles (e.g. see [1–4, 6]). Our talk presents the results of a comprehensive study of the inversion of the star transform published in [2]. In particular, we describe the necessary and sufficient conditions for invertibility of the star transform defined on scalar fields, introduce an exact, closed form inversion formula, and discuss its stability properties. As an unexpected dividend of our approach, we obtained a proof of a conjecture from algebraic geometry about the zero sets of elementary symmetric polynomials, which is stated at the end of this abstract.

Let $f(x) \in C_c\left(\mathbb{R}^2\right)$ be a compactly supported continuous function, and let γ be a fixed unit vector.

Definition 1. *The divergent beam transform* $\mathcal{X}_\gamma$ *of* f *at* $x \in \mathbb{R}^2$ *is defined as:*

$$\mathcal{X}_\gamma f(x) = \int_0^\infty f(x + t\gamma)\, dt. \tag{1}$$

The *star transform of* f is a linear combination of divergent beam transforms with a set of fixed directions $\gamma_i \in S^1$ and non-zero constants $c_i \in \mathbb{R}$, $i = 1, \dots, m$. More formally,

Definition 2. *The star transform* $\mathcal{S}$ *of* f *at* $x \in \mathbb{R}^2$ *is defined as:*

$$\mathcal{S}f(x) = \sum_{i=1}^{m} c_i\, \mathcal{X}_{\gamma_i} f(x) = \sum_{i=1}^{m} c_i \int_0^\infty f(x + t\gamma_i)\, dt. \tag{2}$$

Two special types of star transforms play a prominent role in our main results presented below. The *symmetric* star transforms comprise the only non-invertible configurations, while the *regular* star transforms contain the operators with the most stable inversions.

Definition 3. *The star transform is called* ***symmetric****, if* $m = 2k$ *for some* $k \in \mathbb{N}$ *and (after possible re-indexing)* $\gamma_i = -\gamma_{k+i}$ *with* $c_i = c_{k+i}$ *for all* $i = 1, \dots, k$.

Theorem 1 (Injectivity)**.** *The star transform* $\mathcal{S} = \sum_{i=1}^{m} c_i \mathcal{X}_{\gamma_i}$ *is invertible* ***if and only if*** *it is not symmetric.*

Corollary 1. *Any star transform with an odd number of rays is invertible.*

Definition 4. *The star transform is called* ***regular****, if* $c_1 = \ldots = c_m = 1$ *and the ray directions* γ_i, $i = 1, \dots, m$ *correspond to the radius vectors of the vertices of a regular* m*-gon.*

Theorem 2 (Inversion)**.** *Consider the star transform* $\mathcal{S}$ *defined in (2) and let*

$$q(\psi) = \frac{-1}{\displaystyle\sum_{i=1}^{m} \frac{c_i}{\langle \psi, \gamma_i \rangle}}, \quad \psi \in S^1. \tag{3}$$

Then the following is true for any unit vector ψ *in the domain of* q*:*

$$\mathcal{R}f(\psi, s) = q(\psi) \frac{d}{ds} \mathcal{R}(\mathcal{S}f)(\psi, s), \tag{4}$$

where $\mathcal{R}$ *denotes the (classical) Radon transform of a function in* $\mathbb{R}^2$.
Therefore, if q *is defined almost everywhere, one can apply* $\mathcal{R}^{-1}$ *to recover* f.

The issues related to the invertibility and stability of the inversion of the star transform boil down to the behavior of the function $q(\psi)$ and its singularities. It is easy to notice that if the star transform is injective, then the singularities appearing in the right-hand side of inversion formula (4) are removable. Namely,

Remark 1. *Let* $\{\psi_i\}_{i=1}^{M}$, $M \geq m$ *be such that*

$$\langle \psi_i, \gamma_j \rangle = 0, \ \textit{for some } j \in \{1, \dots, m\} \tag{5}$$

and/or

$$\sum_{j=1}^{m} c_j \prod_{i\neq j} \langle \psi_i, \gamma_j \rangle = 0, \tag{6}$$

then

$$\lim_{\psi\to\psi_i} \left[q(\psi) \frac{d}{ds} \mathcal{R}(\mathcal{S}f)(\psi, s) \right] = \mathcal{R}f(\psi_i, s) < \infty. \tag{7}$$

Definition 5. *We call ψ_i's satisfying condition (5) singular directions of Type 1 and those satisfying condition (6) singular directions of Type 2. These two types are not mutually exclusive.*

The number and location of singular directions affect the quality of numerical reconstructions. The singular directions of Type 2 correspond to "division by zero" of the processed data $\frac{d}{ds}\mathcal{R}(\mathcal{S}f)$, while those of Type 1 correspond to "multiplication by zero". Hence, it is natural to expect that singular directions of Type 2 will create instability and adversely impact the reconstruction. Our numerical experiments confirm these expectations (see [2]). It is also interesting, that the (totally different) algorithm for inversion of the star transform obtained in [6] produces a relation equivalent to (6) as a necessary and sufficient condition for the instability of that algorithm (see formula (51) on page 18 in [6]).

Since the singular directions of Type 2 are more crucial for the quality of reconstructions, in the next several theorems we discuss the existence of singular directions of Type 2 in the star transforms with different configurations. Here and in what follows, by "configuration" we mean a specific choice of the unit vectors γ_i and constants $c_i \neq 0$, $i = 1, \ldots, m$.

Theorem 3. *Consider the star transform $\mathcal{S} = \sum_{i=1}^{m} \mathcal{X}_{\gamma_i}$ with uniform weights.*

(1) If m is even, $\mathcal{S}$ must contain a singular direction of Type 2.

(2) When m is odd, there exist configurations of $\mathcal{S}$ that contain singular directions of Type 2, as well as configurations that do not contain them.

Theorem 4. *The regular star transform $\mathcal{S}$ with $m = 2k+1$ rays does not have a singular direction of Type 2.*

In a certain sense, such star transforms have the most stable inversions (see [2]).

Theorem 5. *Consider the star transform $\mathcal{S} = \sum_{i=1}^{m} c_i \mathcal{X}_{\gamma_i}$. If m is even, $\mathcal{S}$ must contain a singular direction of Type 2.*

Theorem 6. *Consider a star transform $\mathcal{S} = \sum_{i=1}^{m} c_i \mathcal{X}_{\gamma_i}$, where $m = 2k+1$.*

(a) For any set of specified weights $c_1 \ldots, c_m$, there exist $\gamma_1, \ldots, \gamma_m$ such that $\mathcal{S}$ contains singular directions of Type 2.

(b) Let $m = 3$. For any set of specified weights c_1, c_2, c_3, there exist $\gamma_1, \gamma_2, \gamma_3$ such that $\mathcal{S}$ does not contain singular directions of Type 2.

The generalization of Theorem 6 (b) to the case of $m = 2k + 1 > 3$ is technically more complicated and has not been proven yet.

We finish with a result in algebraic geometry advertised at the beginning of this abstract. Let $e_r(y_1, \ldots, y_m)$ denote the elementary symmetric polynomial of degree r in $\mathbb{R}^m$. In paper [5], the author formulated the following conjecture:

Conjecture. *If r is even then $e_r^{-1}(0)$ contains no real vector subspace of dim r.*

Furthermore, it is stated there that one of the extreme cases is "the case $e_{m-1}(y_1, ..., y_m)$, $m \equiv 1 \pmod 2$, which becomes a task quite hard to tackle".

Our proof of Theorem 4 includes a proof of the aforementioned extreme case. Namely,

Theorem 7 (Zeros of $e_{m-1}(y_1, \ldots, y_m)$ for odd m)**.** *Let $m = 2k + 1$ for some $k \in \mathbb{N}$. Then $e_{m-1}^{-1}(0)$ contains no real vector subspace of dimension $m - 1$.*

REFERENCES

[1] G. Ambartsoumian, *Generalized Radon Transforms and Imaging by Scattered Particles: Broken Rays, Cones, and Stars in Tomography*, World Scientific, 2023.

[2] G. Ambartsoumian, and M. J. Latifi, *Inversion and symmetries of the star transform*, The Journal of Geometric Analysis **31** 11 (2021), 11270–11291.

[3] G. Ambartsoumian, M. J. Latifi, and R. K. Mishra, *Generalized V-line transforms in 2D vector tomography*, Inverse Problems, **36** 10 (2020): 104002.

[4] G. Ambartsoumian, M. J. Latifi, and R. K. Mishra, *Numerical implementation of generalized V-line transforms on 2D vector fields and their inversions*, preprint arXiv:2305.08975 (2023).

[5] A. Conflitti, *Zeros of real symmetric polynomials*, Applied Mathematics E-Notes, **6** (2006), pp 219–224.

[6] Z. Zhao, J. Schotland, and V. Markel, *Inversion of the star transform*, Inverse Problems, **30** 10 (2014), 105001.

Phase Retrieval and Tomographic Reconstruction in X-ray Near-field Diffractive Imaging: Inverse Problems at Work

TIM SALDITT

X-rays can provide information about the structure of matter, on multiple length scales from bulk materials to nanoscale devices, from organs to organelle, from the organism to macromolecule. Due to the widespread lack of suitable lenses, the majority of investigations are rather indirect — apart from classical shadow radiography perhaps. While diffraction problems have been solved since long, the modern era has brought about lensless coherent imaging with X-rays, down to the nanoscale. How much more room for improvement is offered by full exploitation of indirect measurements, sophisticated analysis and high performance algorithms, and how far can this go? In this talk we discuss image formation and reconstruction in the optical far- and near-field, the limits imposed by partial coherence, optical constants, and object constraints, the role of imperfect lenses and photon correlations. We show how solutions and algorithms of mathematics of inverse problems [1–3] help us to meet the challenges of phase retrieval, tomographic reconstruction, and more generally image processing of bulky data. All to the benefit of ambitious imaging projects such as mapping the human brain [4, 6] or fighting infectious diseases [6].

REFERENCES

[1] T. Salditt, A. Egner, and R. D. Luke (Eds.), Nanoscale Photonic Imaging. Springer Nature (2020), TAP, 134, Open Access Book.

[2] L. M. Lohse, A.-L. Robisch, M. Töpperwien, S. Maretzke, M. Krenkel, J. Hagemann, and T. Salditt, *A phase-retrieval toolbox for X-ray holography and tomography.* Journal of Synchrotron Radiation (2020), 27, 3.

[3] S. Huhn, L. M. Lohse, J. Lucht, and T. Salditt, *Fast algorithms for nonlinear and constrained phase retrieval in near-field X-ray holography based on Tikhonov regularization* (2022), `https://arxiv.org/abs/2205.01099`

[4] M. Eckermann, B. Schmitzer, F. van der Meer, J. Franz, O. Hansen, C. Stadelmann, and T. Salditt, *Three-dimensional virtual histology of the human hippocampus based on phase-constrast computed tomography.* Proceedings of the National Academy of Sciences (2021), 118, 48, e2113835118.

[5] M. Eckermann, J. Frohn, M. Reichardt, M. Osterhoff, M. Sprung, F. Westermeier, A. Tzankov, C. Werlein, M. Kuehnel, D. Jonigk, and T, Salditt, *3D Virtual Patho-Histology of Lung Tissue from Covid-19 Patients based on Phase Contrast X-ray Tomography*, eLife (2020).

[6] M. Reichardt, P. M. Jensen, V. A. Dahl, A. B. Dahl, M. Ackermann, H. Shah, F. Länger, C. Werlein, M. P. Kuehnel, D. Jonigk, and T. Salditt, *3D virtual hitopathology of cardiac tissue from Covid-19 patients based on phase-constrast X-ray tomography*, eLife (2021), 10:e71359.

Tomographic inverse problems: which place for deep learning?

VOICHITA MAXIM

In the last years, deep learning has emerged as an area of active research and many publications have already shown very impressive results. While ethical questions have been raised concerning utilization in medicine, experimental results from different teams clearly demonstrate its potential. In parallel, theoretical studies are attempting to elucidate the underlying mechanism of neural networks and to strengthen their interpretability and explainability.

The predominant approach to deep learning tomographic image enhancement is to post-process the analytically reconstructed images. This simple yet effective strategy is applicable to a wide range of situations and can handle large volumes in a clinically compatible time frame. As long as the quality of the initial reconstruction is not overly deteriorated, post-processing may be adequate. Pre-processing of the data is an other option. The place reserved to deep learning and the techniques to achieve image quality improvements can be as diverse as the applications.

We tried several instances of deep networks for inverse problems. For CBCT images from real acquisitions, 2D and 3D U-Nets gave very good results for removing CBCT and metal artefacts from low-dose images. U-Net post-processing can be assimilated to non-linear image filtering in analytical reconstruction and is equally fast. Instead of being hand-crafted by a specialist, the Γ_θ filter, θ being the vector of weights, is learned automatically from a database that is supposed to faithfully represent the distribution of the images. Our test was carried out with a low dose simulated by reducing the number of projections compared with the normal dose acquisition [1]. With continuous acquisition, which is the most widespread technique, it is not possible to produce large sets of low dose / normal dose image pairs of patients, as this would require double irradiation.

At the opposite end of the spectrum is unsupervised learning from a single image. We are currently testing it for estimating the convolution kernel from a pair of sharp (f) and blurred (g) images. The kernel is stored in the structure of a network trained according to a loss function representing the convolution process:

$$\mathcal{L}(\theta) = d(f * \Gamma_\theta(u), g). \tag{1}$$

The network receives an input u which can be an image of noise as in [2]. This technique works well even in the presence of noise on the data, but fails for strongly degraded realistic data. In this case a better option might be supervised learning on Monte-Carlo simulated data, followed by weight refinement during test. This strategy outperforms supervised learning when the training set does not accurately reflect the distribution of the data. Unsupervised learning is an instance of iterative reconstruction, based entirely on a data fidelity cost function. However, an intrinsic regularisation is performed by the network structure and an early stopping [2]. Supervised learning followed by test-time training can be thought of as initial nonlinear filtering of the image, followed by iterative refinement. As in our experiment, the image and the convolution kernel are reconstructed at the same time, this refinement concerns not only the result of the inverse problem but also the formulation of the direct model.

For bimodal PET/MR reconstruction, we are implementing and testing a variational auto-encoder that jointly encodes high-quality PET and MR images. Its role is to improve a pair of low-quality PET/MR images by optimisation within the latent space, at each iteration of an ADMM algorithm. A regularized solution is then obtained by alternating optimisation on data fidelity with careful selection of the value of a latent variable encoding the a priori information.

Considered for some time as a favourite to replace analytical methods in tomographic imaging, iterative methods have the advantage of building on physical models for the data and noise, general priors on the image and a growing body of convergent and efficient optimization algorithms. Whereas much of the noise and artefacts seen in analytically reconstructed images are removed, the texture can be modified and some of the smallest features can be suppressed. Moreover, rather high computing time and memory demands are significant pitfalls for clinical deployment. Despite these drawbacks, iterative methods for regularized reconstruction are still at the forefront of progress in emission tomography, benefiting from the noise properties and the complex nature of the partly unknown direct operator. New approaches in deep learning might go beyond current limitations and still remain interpretable in the sense of analytical or iterative algorithms.

In emission tomography, visualizing the distribution of radiotracers from the emitted gamma rays has a particular importance for the diagnosis of cancer and certain functional diseases, as well as for therapeutic monitoring. New issues are emerging in the context of development of therapies and imaging devices. This is namely the case when the projection model goes beyond the classical paradigm of Radon projection on lines. One example is collimated SPECT detectors that wrap around the patient's body. Compton camera imaging, where projections are acquired on conical surfaces, is another one. The direct operator is in this case partially unknown. It results in unknown, spatially varying and source-dependent point spread functions and low image resolution. Analytical non-linear filtering achieved by supervised learning might not be precise enough in particular when distribution shifts occur. The physical model should be accounted for, either in the learning process or in an iterative algorithm with network-based regularization.

With neural networks we got more flexibility in the choice of filters or priors and new methods pretty much similar to settled ones, although still significantly heuristic.

References

[1] L. Friot--Giroux, *Méthodes de reconstruction avancées en tomographie dentaire par faisceau conique*, PhD thesis, INSA Lyon (2023).

[2] D. Ulyanov, A. Vedaldi, V. Lempitsky, *Deep image prior*, International Journal of Computer Vision **128**, (2020).

[3] T. Leuliet, *Deep Learning for tomographic reconstruction: study and application to computed tomography and positron emission imaging*, PhD thesis, INSA Lyon (2022).

[4] V. Gautier et al, *VAE constrained MR guided PET reconstruction*, 17th International Meeting on Fully 3D Image Reconstruction in Radiology and Nuclear Medicine (2023)

Data-driven approaches to address model inexactness and motion in Compton Scattering Tomography

Gaël Rigaud

(joint work with David Elias Frank)

Compton scattering stands for the collision between a photon and an electron and is the foundation for the so-called Compton scattering tomography (CST). This latter proposes to benefit the recent advances in energy resolved detectors (for instance scintillation crystals) to enhance standard computerized tomography (CT) with the variable energy. Focusing on the first-order scattering which represents the most informative part of the measured spectrum, we obtain a nonlinear generalized-type Radon transform on the electron density f,

$$\mathscr{A}(f,f)(p,\mathbf{d},\mathbf{s},t) := \int_\Omega \mathcal{W}_1(f(\cdot,t))(\mathbf{x},\mathbf{d},\mathbf{s})\ f(\mathbf{x},t)\ \delta(p-\phi(\mathbf{x},\mathbf{d},\mathbf{s}))\ \mathrm{d}\mathbf{x}$$

with $p = \cot\omega$, where $\cot : (0,\pi) \mapsto \mathbb{R}$ and the characteristic function given by

$$\phi(\mathbf{x},\mathbf{d},\mathbf{s}) = \frac{\kappa(\mathbf{x},\mathbf{d},\mathbf{s}) - \rho(\mathbf{x},\mathbf{d},\mathbf{s})}{\sqrt{1-\kappa^2(\mathbf{x},\mathbf{d},\mathbf{s})}} \quad \text{where} \quad \kappa = \frac{(\mathbf{x}-\mathbf{s})}{\|\mathbf{x}-\mathbf{s}\|}\cdot\frac{(\mathbf{d}-\mathbf{s})}{\|\mathbf{d}-\mathbf{s}\|}, \quad \rho = \frac{\|\mathbf{x}-\mathbf{s}\|}{\|\mathbf{d}-\mathbf{s}\|}.$$

We refer to [1] for more details. The function ϕ characterizes the locations of first-order scattering events and corresponds to the inside part of a spindle torus in 3D and to two circular-arcs in 2D between a source $\mathbf{s}$ and a detector $\mathbf{d}$ parametrized by a scalar p (accounting for the energy). The operator $\mathcal{W}_1$ accounts for the physical factors (attenuation and dispersion). To discretize and approximate $\mathscr{A}$, we consider the dynamic discrete (linear) inverse problem

$$g^{\mathrm{dyn}} = Af + \varepsilon \quad \text{with} \quad f := \begin{bmatrix} f_1 \\ \vdots \\ f_{n_t} \end{bmatrix}; \quad g^{\mathrm{dyn}} := \begin{bmatrix} g_1 \\ \vdots \\ g_{n_t} \end{bmatrix}; \quad A := \begin{bmatrix} A_1 & & 0 \\ & \ddots & \\ 0 & & A_{n_t} \end{bmatrix}$$

in which the vector time $t \in \mathbb{R}^{n_t}$ is equally spaced.

Modelling the Compton scattering effect leads to many challenges such as non-linearity of the forward model, multiple scattering and high level of noise for moving targets. To tackle these different issues, we studied and compared in this work two data-driven techniques, namely the regularized sequential subspace optimization and a Bayesian method based on the generalized Golub-Kahan bidiagonalization. We also explored the possibilities to mimic and improve the stochastic approach with deep neural networks.

The Bayesian framework interprets the sought-for images as realizations of a random variable with multivariate Gaussian distribution and was studied for dynamic inverse problems in [2,3]. More precisely, $f \sim \mathcal{N}(\mu, \lambda^{-2}Q)$ and $\epsilon \sim \mathcal{N}(0, R)$ (typically $R = \delta I$). Thereby, the desired structure is implied onto the reconstruction by the choice of the prior assumptions on the Gaussian vector, namely μ, Q, R. We aim to minimize

$$\frac{1}{2}\|A(Qx+\mu) - g^{\mathrm{dyn}}\|^2_{R^{-1}} + \frac{\lambda^2}{2}\|x\|^2_Q \quad \text{with} \quad x \leftarrow Q^{-1}(f-\mu).$$

The Generalized Golub-Kahan bidiagonalization (genGKB) delivers a *singular* system (B_k, U_{k+1}, V_k) which allows us to build regularized solutions $f_k = \mu + QV_k z_k$ with

$$z_k = \arg\min_z \left\{ \frac{1}{2}\|B_k z - e_1\|_2^2 + \frac{\lambda^2}{2}\|z\|_2^2 \right\}$$

with the relation $U_{k+1}e_1 = g^{\mathrm{dyn}}$.

While the Bayesian approach is computationally effective and stable to the different issues of the underlying inverse problem, the approximation and especially the regularization in the low-dimensional minimization problem can lead to very smooth results and loss of details. Therefore, we propose a deep neural network, consisting of two intertwined Deep Image Prior based networks, striving to mimic and enhance the Bayesian approach. In particular, we consider a Encoder - Feature Extraction - Decoder architecture, where the Encoder is given by the generalized Golub-Kahan bidiagonalization. Starting from the projected system of low dimension, the middle part of the network can extract the features similar to the minimization of the Bayesian approach, but with a better control on the smoothing effect. The overall neurons are initialized following the matrix B_k. The proposed neural networks combine the stability and robustness of the Bayesian approach with the power of data-driven machine learning techniques. The neural network

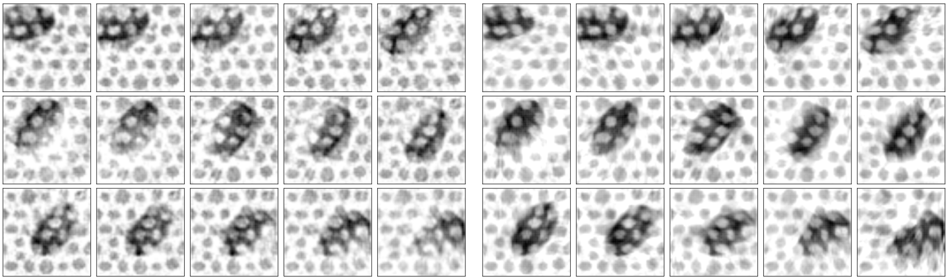

(A) genGKB (B) NNs

Figure 1. Reconstructions using the Bayesian approach and the proposed autoencoder.

is unsupervised, as large databases suitable for Compton scattering tomography do not exist yet. The results are depicted in Fig. 1.

Regularized sequential subspace optimization is an iterative projection-based method able to compensate the model uncertainty of the associated inverse problem due to the linear approximation of the observation model and the multiple scattering, see [4–6]. As a global estimate on the model deviation is not as informative, the method uses a discrete framework to incorporate local inexactness into the reconstruction. The principle can be extended in a straight-forward way to the dynamic case. The changes of the object during the data collection can be seen as deformation of a "true" state, interpreted as model uncertainty and therefore compensated. Depending on the motion, the local model inexactness can thus become quite large. The reconstruction process requires a good prior estimation of these local uncertainties, which are difficult to obtain in realistic applications. The results for one time interval are depicted in Fig. 2. One can see that the RESESOP provides the best reconstruction possible, see Fig. 2(a) and (c), at the cost of perfect estimates of the model uncertainty which is unreallistic. For more reasonable estimates, see Fig. 2(b) and (d), the quality of reconstructions is vastly reduced. One can see the benefits in terms of robustness of the Bayesian approach as depicted in Fig. 1.

References

[1] G. Rigaud and B. Hahn, *3D Compton scattering imaging and contour reconstruction for a class of Radon transforms*, Inverse Problems 34 (2018) 075004 (22pp).

[2] Gdaniec et al. *Detection and Compensation of Periodic Motion in Magnetic Particle Imaging*, IEEE Trans Med Imaging, 36(7) (2017) 1511-1521.

[3] Chung and Saibaba *Generalized hybrid iterative methods for large-scale Bayesian inverse problems*, SIAM Journal on Scientific Computing, 39(5) (2017) pp. 24–46.

[4] F. Schöpfer, T. Schuster and A.K. Louis, *Metric and Bregman projections onto affine subspaces and their computation via sequential subspace optimization methods*, J. Inverse Ill-Posed Problems, 15 (2007), 1–29.

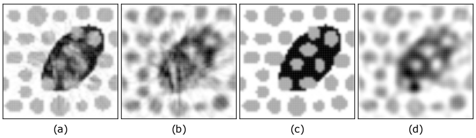

Figure 2. Reconstructions using RESESOP with estimations (1a), (1b), (1c), (1d) respectively.

$$\delta_{s,t} = \begin{cases} A_{s,t}(0,f)_\tau - g^{\mathrm{dyn}}_{s,t} & \text{(1a)} \\ A_{s,t}(0,f^{\mathrm{Bay}})_\tau - g^{\mathrm{dyn}}_{s,t} & \text{(1b)} \\ A_{s,t}(f^{\mathrm{Bay}},f)_\tau - g^{\mathrm{dyn}}_{s,t} & \text{(1c)} \\ A_{s,t}(f^{\mathrm{Bay}},f^{\mathrm{Bay}})_\tau - g^{\mathrm{dyn}}_{s,t} & \text{(1d)} \end{cases}$$

where (s,t) stands for the space/time discretization on data, f the exact solution and f^{Bay} the Bayesian reconstruction.

[5] S. Blanke, B. Hahn and A. Wald, *Inverse problems with inexact forward operator: iterative regularization and application in dynamic imaging*, Inverse Problems, 36 (2020) 124001.
[6] J. Gödeke and G. Rigaud, *Imaging based on Compton scattering: model-uncertainty and data-driven reconstruction methods*, Inverse Problems, 39(3), (2023).

Integrating data-driven techniques and theoretical guarantees for limited angle tomography

Tatiana A. Bubba

(joint work with Mathilde Galinier, Matti Lassas, Marco Prato, Luca Ratti, Samuli Siltanen)

In traditional computed tomography (CT), a series of projection images of an object is collected at different angular directions. Such images are the result of the attenuation of incoming radiation measured by the detector. Mathematically, tomographic imaging is about solving the inverse problem of recovering the information on the internal structure of the object, modelled as a function $f : \mathbb{R}^n \to \mathbb{R}$ with $n > 1$, from the indirect measurements collected by the detector. For instance, in conventional CT, the underlying physical linear model R is given by the X-ray transform:

$$R(f)(s,\omega) = \int_{-\infty}^{\infty} f(s\omega^\perp + t\omega)\,\mathrm{d}t \qquad s \in \mathbb{R},\ \omega,\omega^\perp \in S^1 \tag{1}$$

where $\omega^\perp$ denotes the vector in the unit sphere S^1 obtained by rotating ω counterclockwise by 90° [7].

When the direction vector ω is restricted within a limited angular range $[-\Gamma,\Gamma]$, the inverse problem arising is generally called *limited-angle computed tomography* (LA-CT), in the following denoted by R_Γ. It appears frequently in practical applications, such as dental tomography [5] or breast tomosynthesis [10].

Due to the severe ill-posedness of the LA-CT problem, limited angle geometry is still a testing ground for several theoretical and numerical studies. Microlocal analysis is used to predict which singularities, that is, sharp features of the object being imaged, can be reconstructed in a stable way from limited angle measurements [8]. Even so, the task of robustly recovering the unknown quantity of interest from such partial indirect measurement is a challenging one. Standard techniques like the well-known filtered back-projection (FBP), perform rather poorly due to the lack of a comprehensive measurement set.

Combining iterative schemes with variational regularisation techniques based on promoting sparsity (*i.e.*, reflecting the prior knowledge that the exact solution is expected to have few non-vanishing components, for example, in a suitable wavelet [6] decomposition) allow for accurate reconstructions from fewer tomographic measurements than those usually required by methods like FBP, but still leave room for improvement in terms of reconstruction quality.

In recent years, machine learning approaches, in particular, deep learning, with convolutional neural networks (CNNs) being the most prominent design in the context of imaging, are increasingly impacting the field of inverse problems [1], including LA-CT. In particular, hybrid reconstruction frameworks where the practical advantages of learning-based method are combined with the theoretical understanding that comes from model-based approaches have been widely applied for the solution of ill-posed inverse problems, showing that these approaches are able to significantly surpass both pure model- and more data-based methods.

Following this trend, in this talk a recent work done in collaboration with M. Galinier, M. Lassas, M. Prato, L. Ratti and S. Siltanen [2] is showcased, where a novel convolutional neural network, called ΨDONet, is designed starting from the unrolled iterations of the Iterative Soft Thresholding Algorithm (ISTA), a classical reconstruction algorithm for sparsity promoting regularization [3]. ISTA iteratively creates the sequence $\{w^{(n)}\}_{n=1}^{N}$ as follows:

$$w^{(n)} = \mathcal{S}_{\lambda/L}\left(w^{(n-1)} - \frac{1}{L}K^{(n)}w^{(n-1)} + \frac{1}{L}b^{(n)}\right), \tag{2}$$

where, in our case, $K^{(n)} = WR_\Gamma^* R_\Gamma W^*$, with W wavelet transform associated with an orthogonal family, $b^{(n)} = WR_\Gamma^* m$ and $S_\beta(w)$ is the (component-wise) soft-thresholding operator. ISTA can be applied to (1) to recover $f = W^*w$ from the measurements $m = R(f)$. It is well-known that the unrolled iterations of ISTA can be considered as the layers of a neural network (see [4], where Learned ISTA is introduced).

The novelty of our approach is that ΨDONet takes advantage of the possibility to use small filters encoding a combination of upscaling, downscaling and convolution operations, as it is common practice in deep learning, which can be exactly determined combining the convolutional nature of the limited angle X-ray transform and basic properties defining an orthogonal wavelet system. As a result, it is possible to interpret the operations in (2) as a layer of a CNN, which in turn provides fairly general network architectures that allow to recover standard ISTA for a specific choice of the parameters involved. The name of the network is motivated by the key feature of ΨDONet: the convolutional kernel is split into $K = K_0 + K_1$ where K_0 is the known part of the model (*i.e.*, $K_0 = R_\Gamma^* R_\Gamma$) and K_1 is an unknown pseudodifferential operator ΨDO to be learned. Basically, in K_1 lays the potential to add information in the reconstruction process with respect to the known part of the model K_0, thus inducing a "microlocal regularisation" that smooths away the singularities, effectively improving the reconstruction quality. The convergence of the proposed scheme is ensured by classical results on the convergence theory of ISTA and relies on interpreting our network as a modification or perturbation of ISTA for which we can bound the coefficients of the filters.

ΨDONet is numerically tested on simulated data from limited angle geometry, generated from the ellipse data set. Compared to standard ISTA (and FBP), the improvement provided by our results is mainly in its ability to smooth singularities, while preserving features of interest (like sharp boundaries) and suppressing noise.

In the second part of the talk, more recent numerical results are presented, obtained by "boosting" ΨDONet to reduce the computational burden and allowing for more generality in the learning scheme, while still preserving theoretical guarantees. In particular, the unrolled iteration of ISTA are extrapolated allowing for a learned version of the well-known Fast ISTA (FISTA) algorithm, and the soft-thresholding operator is replaced by learned regularisation through the Plug and Play (PnP) paradigm [9]. Future work will be mostly devoted to addressing convergence of the optimal network for PnP-ΨDONet, and generalization from the training sample.

References

[1] S. Arridge, P. Maass, O. Öktem and C.-B. Schönlieb, *Solving inverse problems using data-driven models*, Acta Numer. **28** (2019), 1–174.

[2] T.A. Bubba , M. Galinier, M. Lassas, M. Prato, L. Ratti and S. Siltanen, *Deep neural networks for inverse problems with pseudodifferential operators: an application to limited-angle tomography*, SIAM J. Imaging Sci. **14**(2) (2021), 470–505.

[3] I. Daubechies, M. Defrise and C. De Mol, *An iterative thresholding algorithm for linear inverse problems with a sparsity constraint*, Commun. Pure Appl. Math. **57** (11) (2004), 1413–1457.

[4] K. Gregor and Y. LeCun, *Learning fast approximations of sparse coding*, Proc. 27th International Conference on Machine Learning (2010), 399–406.

[5] V. Kolehmainen, S. Siltanen, S. Järvenpää, J.P. Kaipio, P. Koistinen, M. Lassas, J. Pirttilä and E. Somersalo, *Statistical inversion for medical x-ray tomography with few radiographs: II. Application to dental radiology*, Phys. Med. Biol. **48**(10) (2003), 1465.

[6] S. Mallat, *A wavelet tour of signal processing*, Elsevier (1999).

[7] F. Natterer, *The mathematics of computerized tomography*, SIAM (2001).

[8] E.T. Quinto, *Singularities of the X-Ray transform and limited data tomography in $\mathbb{R}^2$ and $\mathbb{R}^3$*, SIAM J. Math. Anal. **24**(5) (1993), 1215–1225.

[9] S. Venkatakrishnan, C.A. Bouman and B. Wohlberg, *Plug-and-play priors for model based reconstruction*, 2013 IEEE GlobalSIP, 945–948.

[10] Y. Zhang, H.P. Chan, B. Sahiner, J. Wei, M.M. Goodsitt, L.M. Hadjiiski, J. Ge and C. Zhou, *A comparative study of limited-angle cone-beam reconstruction methods for breast tomosynthesis*, Med. Phys. **33**(10) (2006), 3781–3795.

Mathematical model and stability analysis for an inverse problem in light sheet fluorescence microscopy

Matias Courdurier

(joint work with Pablo Arratia, Victor Castañeda, Evelyn Cueva, Steffen Härtel, Axel Osses and Benjamin Palacios)

In Fluorescence Microscopy a relatively small and almost transparent sample, containing a distribution of fluorophore, is illuminated with a laser to activate the fluorescence. A camera outside the sample measures the irradiated fluorescent light and the final goal is to estimate the fluorophore distribution inside the sample using these exterior measurements (see e.g. [5]). In Light Sheet Fluorescence Microscopy (LSFM), the strategy is to optically slice the sample by illuminating planes perpendicular to the camera sequentially, one at a time, obtaining a reconstruction of the fluorophore distribution by direct imaging (e.g. [6]). The technique of LSFM has some advantages compared to regular confocal fluorescence microscopy, like a reduced photo-toxicity and reduced photo-bleaching effects, but it can be qualitatively observed that blurring artifacts affect the reconstruction of the fluorophore distribution as you move further away from the illumination side, which then requires multiple illumination views (see e.g. [3, 4])

To understand some of the mechanisms behind this blurring effect in LSFM, and to propose possible improvements to this imaging technology, we study a mathematical model for LSFM in two dimensions, including some diffusion in the illumination stage of LSFM, and we then tackle the reconstruction of the fluorophore distribution as an inverse problem (instead of purely direct observations).

For the fluorescence stage we did not included diffusion of light in the model and stayed with a relatively simple transport model with collimated measurements at the camera. It is worth mentioning that more complex models, providing a more complete and accurate physical description of LSFM imaging technique would be of interest, and it is one of possible directions in which the work presented here could be extended. At this point though, we will only consider our intermediate model, since heuristically most of the blurring artifact originate in the illumination stage, and our model is admits reasonable mathematical analysis and numerical treatment.

In this talk I will mention results presented in [1, 2], where we proposed the mathematical model and inverse problem for LSFM mentioned above. In the study of such setting, the inverse problem in LSFM is recast as a backwards heat equation problem in $\mathbb{R} \times [0, \infty)$ with knowledge of the solution on a non-cylindrical set, the observation set being a curve in the space-time variables. For the specific family of backwards heat equations arising from the LSFM inverse problem, we establish the injectivity of the forward operator, hence answering the uniqueness question for the corresponding inverse problem, and we establish a conditional logarithmic stability result.

We also explore some numerical aspects of the inversion for the LSFM inverse problem through computational simulations.

In what follows I present in more details the setting above. Let us consider the domain $D := [0,1] \times [-1,1]$ subset of $\mathbb{R}^2$ and an open convex set $\Omega \subset D$.

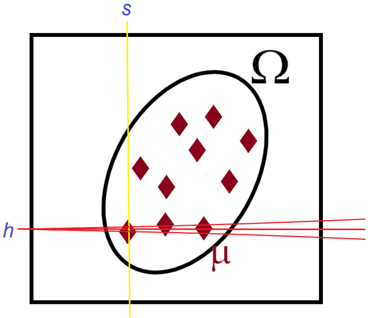

At each height $h \in [-1,1]$ we will illuminate from the left with a laser in an horizontal direction, which will propagate and also widen due to diffusion, activating the fluorophore with support Ω and distributed with an unknown density $\mu(x,y)$. The activated fluorophore will then emit fluorecent light that will be measured up by a collimated camera at pixels in positions $s \in [0,1]$, measuring only light traveling vertically.

The quantity $v(x,y,\theta)$ (or $\sum_{n\in\mathbb{Z}} v(x,y,\theta+2\pi n)$ more precisely) describes the intensity of laser photons at spatial position (x,y) traveling in direction $(\cos(\theta),\sin(\theta))$, where $x \in [0,1], y \in \mathbb{R}, \theta \in \mathbb{R}$. We model the propagation of the laser incoming at height h using the following Fermi pencil beam equation:

$$\Big(\partial_x + \theta\partial_y + a(x,h) - \psi(x,h)\partial_\theta^2\Big) v_h(x,y,\theta) = 0, \quad (x,y,\theta) \in (0,1] \times \mathbb{R} \times \mathbb{R},$$
$$v_h(0,y,\theta) = \delta(y-h)\delta(\theta),$$

where a represent the attenuation and ψ characterizes the diffusion of the laser, both non-negative quantities and ψ also strictly possitive in Ω. Given a non-negative fluorophore density $\mu(x,y)$, the activated fluorescence at position (x,y) is $w_h(x,y) := c\mu(x,y) \int_{\mathbb{R}} v_h(x,y,\theta)$. And finally, the total fluorescence measured up at the camera in the pixel at position s is $\mathcal{P}[\mu](s,h) := \int_{\mathbb{R}} w_h(s,y)dy$.

The qualitative aspect of the illumination and fluorescence activation is exemplified in Figure 1.

This model admits an explicit solution, and the measurement at pixel s when illuminating at height h is

$$\mathcal{P}[\mu](s,h) := c\exp\left(-\int_{\gamma(h)}^{s} a(t,h)dt\right) \int_{\mathbb{R}} \frac{\mu(s,r)}{\sqrt{4\pi\sigma(s,h)}} \exp\left(\frac{-(r-h)^2}{4\sigma(s,h)}\right) dr,$$

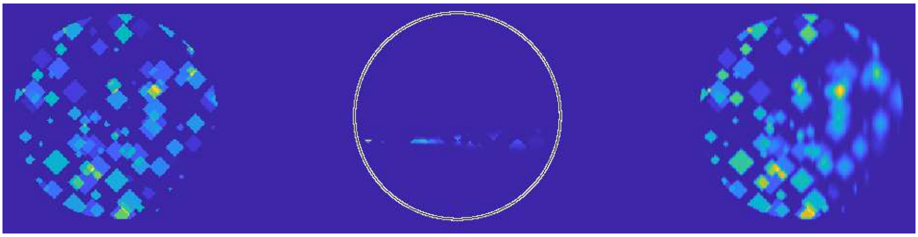

FIGURE 1. Given the fluorophore distribution $\mu(x,y)$ on the left, the middle figure shows $w_h(x,y)$, the fluorophore activated by one laser entering at a given hight h. For visualization purposes, we also show $\int_{-1}^{1} w_h(x,y)dh$ on the right.

with $\gamma(h) = \inf\{t \in [0,1] : (t,h) \in \Omega\}$ and $\sigma(s,h) = \frac{1}{2}\int_{\gamma(h)}^{s}(s-t)^2\psi(t,h)dt$. Assuming that a, ψ are known and that only μ is unknown, the inverse problem in LSFM is the following: for each s fixed, reconstruct $\mu(s,y), y \in [-1,1]$, from the knowledge of $\mathcal{P}[\mu](s,h), h \in [-1,1]$. This can be recast as a backwards heat equation problem. Namely, let $u(y,t)$ be the solution of

$$\begin{aligned} &u_t - \Delta u = 0, \quad t > 0, y \in \mathbb{R},\\ &u(0,y) = u_0(y), \quad y \in \mathbb{R},\\ &\lim_{|y|\to\infty} u(t,y) = 0. \end{aligned}$$

with u_0 supported in $[-1,1]$, let $\sigma(y)$ be a smooth function satisfying $\sigma(y) = 0$ for $|y| > 1$ and $\sigma(y) > 0$ for $|y| < 1$. The inverse problem in LSFM is equivalent to the problem of recovering u_0 from the knowledge of $u(\sigma(y), y), y \in \mathbb{R}$, where the curve σ satisfies some extra conditions. Roughly speaking, in an somewhat imprecise and without mentioning all the hypotheses necessary, the results presented in this talk can be stated as follows:

Theorem. If $u(\sigma(y), y) = 0, \forall y \in \mathbb{R}$, then $u_0(y) = 0, \forall y \in \mathbb{R}$. Which for the LSFM inverse problem means that for each s, knowledge of $\mathcal{P}[\mu](s,h), \forall h \in [-1,1]$, uniquely determines $\mu(s,y), \forall y \in [-1,1]$.

Theorem. Assuming an a priori bound for u_0 in the Sobolev space $H^1(\mathbb{R})$, there exist a constant $C > 0$ and $\kappa \in (0,1)$ such that

$$\|u_0\|_{L^1(\mathbb{R})} \leq C(-\log(\|u\|_{L^2(\{(t,y):t\in[1,2],|y|>2\})})^{-\kappa},$$

which for the inverse problem implies the following stability estimate,

$$\|\mu(s,\cdot)\|_{L^1([-1,1])} \leq \tilde{C}(-\log(\|\mathcal{P}[\mu](s,\cdot)\|_{L^1([-1,1])})^{-\kappa}.$$

References

[1] P. Arratia, M. Courdurier, E. Cueva, A. Osses, B. Palacios, *Lipschitz stability for backward heat equation with application to fluorescence microscopy*, SIAM J. Math. Anal. **53** (7), 2021.

[2] E. Cueva, M. Courdurier, A. Osses, V. Castañeda, B. Palacios, S. Härtel, *Mathematical modeling for 2D light-sheet fluorescence microscopy image reconstruction*, Inverse Problems, **36** (7), 2020.

[3] J. Huisken, *Slicing embryos gently with laser light sheets*, Bioessays, **34**, 406–411, https://doi.org/10.1002/bies.201100120, 2012.

[4] P. Keller, E. Stelzer, *Quantitative in vivo imaging of entire embryos with digital scanned laser light sheet fluorescence microscopy*, Current opinion in neurobiology, **18** (6), 624–632, 2008.

[5] J. Lakowicz, *Principles of Fluorescence Spectroscopy*, Springer, New York, 2013.

[6] P. Santi, *Light sheet Fluorescence microscopy: a review*, Journal of Histochemistry & Cytochemistry, **59** (2), 129–138, 2011.

Bidirectionality and Multiple Scattering Correction in Compton Camera Imaging

Lorenz Kuger
(joint work with Martin Burger)

Compton cameras are an efficient imaging tool for in-situ gamma ray spectrometry that operate without collimation. They therefore attain large sensitivities and allow emission imaging even in low-count or high-background surroundings. Conventionally, Compton cameras are built with separated scattering and absorbing layers of detectors. This setup allows detector materials to be tailored to maximize sensitivity and have good energetic or spatial resolution, but often sacrifices the cameras' ability to produce spatially resolved images in the whole 4π field of view resulting in a de facto collimation. The measurements that a Compton camera makes are energy depositions during coincidences of a Compton scattering event in one detector and subsequent photoelectric absorption of the photon in the material of another detector. In the Compton scattering event, the energy loss of the photon is related to the scattering angle θ through the Compton formula

$$E' = \frac{E}{1 + \frac{E}{mc^2}(1 - \cos\theta)},$$

where E and E' are the photon energies before and after scattering, respectively. In the above ideal measurement, the scattering detector measures $E - E'$ and the absorption detector measures E'. Due to the formula, the energy measurement restrics the source position from which a measured photon originated to the cone surface $\mathcal{C}(\mathbf{x}, \mathbf{y}, E') = \{\mathbf{s} : \angle(\mathbf{y} - \mathbf{x}, \mathbf{x} - \mathbf{s}) = \pi - \theta\}$, where θ and E' as before and $\mathbf{x}$ and $\mathbf{y}$ are scattering and absorption point, respectively.

Formulations of the physical factors that describe the kinematics of a photon in the measurement setup have been carried out in previous works, see e.g. [1]. Gathering these factors in constants $C_1(\mathbf{s}, \mathbf{x})$ and $C_2(\mathbf{x}, \mathbf{y}, E')$ allows us to formulate the forward model, given by a Radon transform $\mathcal{P}$ over cone surfaces

$$\mathcal{P}f(\mathbf{x}, \mathbf{y}, E') = C_2(\mathbf{x}, \mathbf{y}, E') \int_{\mathcal{C}(\mathbf{x}, \mathbf{y}, E')} f(\mathbf{s}) \, \mathrm{d}S(\mathbf{s}).$$

Our main contribution are two extensions to this model. The first one allows detectors to scatter and absorb photons simultaneously. Since the camera's measurements do not give any information about the direction of a coincidence of scattering and absorption, we talk of a bidirectional Compton camera. The additional uncertainty is reflected in the operator describing the forward model: The new expected number of counts for interaction points $\mathbf{x}$ and $\mathbf{y}$ is what we call a biconical Radon transform

$$\mathcal{B}f(\mathbf{x}, \mathbf{y}, E_{\mathbf{x}}, E_{\mathbf{y}}) = \mathcal{P}f(\mathbf{x}, \mathbf{y}, E_{\mathbf{y}}) + \mathcal{P}f(\mathbf{y}, \mathbf{x}, E_{\mathbf{x}}),$$

which is a nonlinearly weighted sum of two conical Radon transforms. To the best of our knowledge, the mapping properties and invertibility of this new integral transform has not been analyzed in the literature up to this point and is an open problem.

The other extension that we propose to consider in the model is motivated by an imaging setup with a Compton camera with relatively large and spatially non-resolved detectors. In these detectors, we show with simulation experiments that multiple scattering events are the predominant case. The coincidences resulting from measurements of multiply scattered photons lead to a model mismatch. We demonstrate that energies deposited in the absorption detector are typically more distributed and smaller than what the model predicts and hence scattering angles are overestimated. We compute a corrected forward model which accounts for double scattering in the first detector. The probabilities for double scattering can be formulated just as the ones for first scattering and are given by the product $C_1(\mathbf{s},\mathbf{x}_1)\tilde{C}_2(\mathbf{x}_1,\mathbf{x}_2,E')C_3(\mathbf{x}_2,\mathbf{y},E',E'')$, with appropriate constants describing physical effects like dispersion, attenuation, polarization and interaction probabilities. This leads to an integral operator formulation of the expected number of measured, twice scattered and subsequently absorbed photons

$$\mathcal{P}^{(2)}(\mathbf{x}_2,\mathbf{y},E'') = \int\limits_{E''}^{E_0} C_3(\mathbf{x}_2,\mathbf{y},E',E'') \int\limits_{\mathcal{C}_2} \tilde{C}_2(\mathbf{x}_1,\mathbf{x}_2,E') \int\limits_{\mathcal{C}_1} f(s)C_1(\mathbf{s},\mathbf{x}_1)\,\mathrm{d}S(\mathbf{x}_1)\mathrm{d}S(\mathbf{s})\mathrm{d}E'$$

for scattering points $\mathbf{x}_1$ and $\mathbf{x}_2$ and cones $\mathcal{C}_1 = \mathcal{C}(\mathbf{x}_1,\mathbf{x}_2,E')$, $\mathcal{C}_2 = \mathcal{C}(\mathbf{x}_2,\mathbf{y},E'')$. Despite the increased complexity, we compute the operator as a forward model, in a way similar as it has been done in PET reconstruction experiments [2]. We show in numerical experiments that it can indeed correct the reconstruction and estimate the position of sources more accurately than the typical single scattering model.

References

[1] V. Maxim, X. Lojacono, E. Hilaire, J. Krimmer, E. Testa, D. Dauvergne, I. Magnin, R. Prost, *Probabilistic models and numerical calculation of system matrix and sensitivity in list-mode MLEM 3D reconstruction of Compton camera images*, Physics in Medicine and Biology **61** **1** (2016), 243–264.

[2] P.J. Markiewicz, M. Tamal, P.J. Julyan, D.L. Hastings, A.J. Reader, *High accuracy multiple scatter modelling for 3D whole body PET*, Physics in Medicine and Biology **52** **3** (2007), 829–847.

Rigid Motion Reconstruction in Parallel Beam and Diffraction Tomography

Denise Schmutz
(joint work with Peter Elbau, Michael Quellmalz, Monika Ritsch-Marte, Otmar Scherzer, Gabriele Steidl)

In our work, we investigate the application of optical microscopy to examine particles that are trapped optically or acoustically. These particles exhibit a continuous rigid motion while undergoing the imaging process. Unlike conventional microscopic imaging, where the specimen is immobilized, this technique enables imaging in a more natural environment. Our objective is to reconstruct the internal structure of the trapped object. However, the precise motion that occurs during the object's illumination is unknown and needs to be determined in advance.

While translations of the object can be recovered to a certain extent, we only describe the reconstruction of the rotation in this abstract. For a comprehensive and in-depth discussion, we direct the reader to [2] and [8]. Currently, I am exploring uniqueness criteria for both parallel beam tomography and diffraction tomography models, which is why the work of my colleagues on diffraction tomography is included in this report.

Both methods take into account the smooth motion over time $t \in [0,T]$ described by a rotation $R \in C^n([0,T];\mathrm{SO}(3))$, where n depends on the underlying model and we denote $R_t := R(t)$. Moreover, in both models we will recover the corresponding angular velocity $\boldsymbol{\omega}\colon [0,T] \to \mathbb{R}^3$ defined by

$$R_t^\top R_t' \boldsymbol{y} = \boldsymbol{\omega}_t \times \boldsymbol{y} \quad \text{for all } t \in [0,T],\ \boldsymbol{y} \in \mathbb{R}^3,$$

with $\boldsymbol{\omega}_t := \boldsymbol{\omega}(t)$. It is convenient to express $\boldsymbol{\omega}_t$ in cylindrical coordinates

$$\boldsymbol{\omega}_t = \begin{pmatrix} \rho_t \boldsymbol{\phi}_t \\ \zeta_t \end{pmatrix}$$

with the azimuth direction $\boldsymbol{\phi}_t \in \mathbb{S}^1_+ := \{(\cos(\alpha), \sin(\alpha))^\top : \alpha \in [0,\pi)\}$, the cylindrical radius $\rho_t \in \mathbb{R}$, and the third component $\zeta_t \in \mathbb{R}$.

1. Parallel beam tomography

In the context of parallel beam tomography, our approach assumes a linear propagation of light through the object g. The light undergoes attenuation due to interaction with the object by refraction and scattering. The measurements can be characterized using the parallel-beam transform

$$m_{PB}(t, x_1, x_2) = \int_{\mathbb{R}} g(R(t)\mathbf{x}) dx_3.$$

According to the Fourier slice theorem, the two-dimensional Fourier transform of the projection image equals a specific central plane of the three-dimensional Fourier transform of the object. This plane is perpendicular to the imaging direction. Consequently, when two projection images at time steps t_1 and t_2 are acquired from distinct imaging directions (or equivalently, from different rotational states of the object), the planes intersect at a *common line* [3, 4].

We utilize this result to derive the following infinitesimal version through differentiation.

Theorem 1. *[2] Let $m_{PB}(t, x_1, x_2)$ be the parallel-beam measurements corresponding to the rotation $R \in C^4([0,T]; SO(3))$. Let $\boldsymbol{\omega} \in C^3([0,T]; \mathbb{R}^3)$ be the associated angular velocity. Then, for all $t \in [0,T]$ satisfying $\rho_t \neq 0$ and all $\lambda \in \mathbb{R}$ the following relation holds*

$$\partial_t \hat{m}_{PB}(t, \lambda \boldsymbol{\phi}_t) = \zeta_t \left\langle \nabla \hat{m}_{PB}(t, \lambda \boldsymbol{\phi}_t), \lambda P^\top \boldsymbol{\phi}_t^\perp \right\rangle,$$

with $P^\top (x_1, x_2)^\top = (x_1, x_2, 0)^\top$ and $\boldsymbol{\phi}_t^\perp = (-\sin(\alpha), \cos(\alpha))^\top$.

Under certain assumptions, the parameters $\boldsymbol{\phi}_t$ and ζ_t can be recovered using this result. For the full reconstruction of the rotation, we will still need to estimate the cylindrical radius ρ_t, which can be done by considering the third order derivative.

2. DIFFRACTION TOMOGRAPHY

In diffraction tomography we assume that the unknown object is illuminated by an incoming plane wave

$$u^{inc}(\boldsymbol{x}) := \mathrm{e}^{\mathrm{i}k_0 x_3},$$

which propagates in direction $\boldsymbol{e}_3 = (0,0,1)^\top$ with wave number k_0. The incident wave generates a scattered wave u^{sca}, which is detected and recorded at the plane $\{x : x_3 = r_M\}$. An approximated scattered wave can be computed as a solution of the Helmholtz equation, taking into account the Sommerfeld radiation condition and the Born approximation. The Born approximation is valid for small objects that exhibit mild scattering. Under these assumptions, we can explicitly express the solution u_t of the Helmholtz equation in the form

$$u_t(\boldsymbol{x}) = \int_{\mathbb{R}^3} \frac{\mathrm{e}^{\mathrm{i}k_0 \|\mathbf{x}-\mathbf{y}\|}}{4\pi \|\mathbf{x}-\mathbf{y}\|} f(R_t \mathbf{y}) u^{inc}(\mathbf{y}) d\mathbf{y},$$

where f is the scattering potential describing the object. Therefore, our measurements can be expressed by:

$$m_{DT}(t, x_1, x_2) = u_t(x_1, x_2, r_M).$$

In this model, a similar result to the Fourier slice theorem, known as the Fourier diffraction theorem, applies. According to the Fourier diffraction theorem, the two-dimensional Fourier transform $\mathcal{F}_2$ of the diffraction measurements corresponds to the three-dimensional Fourier transform $\mathcal{F}_3$ of the object on a hemisphere [1, 5], that is,

$$\mathcal{F}_2[m_{DT}](t, \mathbf{k}) = \sqrt{\frac{\pi}{2}} \mathcal{F}_3[f](R_t h(\mathbf{k})) \frac{\mathrm{i}\mathrm{e}^{i r_M \sqrt{k_0^2 - \|\mathbf{k}\|}}}{\sqrt{k_0^2 - \|\mathbf{k}\|}},$$

where $h(\mathbf{k}) = (k_1, k_2, \sqrt{k_0^2 - \|\mathbf{k}\|} - k_0)^\top$, $\mathbf{k} = (k_1, k_2)$ is the parametrization of the hemisphere with $\|\boldsymbol{k}\| < k_0$.

Similar to the previous scenario, utilizing the fact that these hemispheres at two distinct time steps intersect in a *common circle*, we can derive the following result through differentiation.

Theorem 2. *[8] Let* $\nu_t(k_1, k_2) := \frac{2}{\pi}(\sqrt{k_0^2 - \|\mathbf{k}\|})^2 |\mathcal{F}_2[m_{DT}](t, \boldsymbol{k})|^2$*. Let the rotation* $R \in C^1([0,T]; SO(3))$ *and* $\boldsymbol{\omega} : [0,T] \to \mathbb{R}^3$ *be the associated angular velocity. Then we have for every* $r \in (-k_0, k_0)$ *the relation*

$$\partial_t \nu_t(r\boldsymbol{\phi}_t) = \left(\rho_t \left(k_0 - \sqrt{k_0^2 - r^2}\right) + r\zeta_t\right) \left\langle \nabla \nu_t(r\boldsymbol{\phi}_t), \boldsymbol{\phi}_t^{\perp} \right\rangle,$$

where $\partial \nu_t$ *denotes the partial derivative of* ν_t *with respect to* t*.*

Under certain assumptions all components of the angular velocity may be reconstructed using the above result.

In order to achieve a unique reconstruction of the angular velocity from the given measurements of either model presented, specific assumptions regarding the symmetry of the object are required. If the object possesses high symmetry, the reconstruction of motion parameters may not be unique. While some uniqueness results exist for the method of moments [7] and the common circle method [6], the classification of functions for which the unique recovery of a continuous motion is possible remains an open problem.

3. ACKNOWLEDGMENTS

This research is supported by the Austrian Science Fund (FWF) and the German Research Foundation (DFG) with SFB F68/STE 571/19-1 ('Tomography across the Scales') project F6804-N36 ('Quantitative Coupled Physics Imaging'), project F6806-N36 ('Imaging of Trapped Particles'), project F6807-N36 ('Tomography with Uncertainties') and project 495365311 ('Motion Detection in Tomography and Microscopy').

REFERENCES

[1] Bortel, G., & Tegze, M. (2011). Common arc method for diffraction pattern orientation. *Acta Crystallographica Section A*, 67(6), 533–543.

[2] Elbau, P., Ritsch-Marte, M., Scherzer, O., & Schmutz, D. (2020). Motion reconstruction for optical tomography of trapped objects. *Inverse Problems*, 36(4).

[3] Goncharov, A. B. (1988). Methods of integral geometry and recovering a function with compact support from its projections in unknown directions. *Applied Mathematics and Mechanics*, 11(3), 213–222.

[4] van Heel, M. (1987). Angular reconstitution: a posteriori assignment of projection directions for 3D reconstruction. *Ultramicroscopy*, 21(2), 111–123.

[5] Huldt, G., Szöke, A., & Hajdu, J. (2003). Diffraction imaging of single particles and biomolecules. *Journal of Structural Biology*, 144(1-2), 219–227.

[6] Kurlberg, P. and Zickert, G. (2021). Formal uniqueness in Ewald sphere corrected single particle analysis. *Preprint on ArXiv*, 2104.05371.

[7] Lamberg, L. (2008). Unique recovery of unknown projection orientations in three-dimensional tomography. *Inverse Problems and Imaging*, 2(4), 547–575.

[8] Quellmalz, M., Elbau, P., Scherzer, O., & Steidl, G. (2022). Motion detection in diffraction tomography by common circle methods. Technical Report No. 2209.08086, arXiv. Accepted in *Mathematics of Computation.*

Accounting for model inexactnesses in Magnetic Particle Imaging

Marius Nitzsche

(joint work with Bernadette Hahn, Hannes Albers, Tobias Kluth)

A novel technique in the field of medical imaging is magnetic particle imaging (MPI), which was introduced in 2005 by Gleich and Weizenecker [1]. The stimulation of injected superparamagnetic iron oxide nanoparticles with a magnetic field results in a temporal change of the magnetization of the particles, that induces a voltage in a receiving coil. One of the notable advantages of MPI is its ability to provide both high spatial resolution and incredibly fast measurement times, all without the use of harmful radiation. The magnetic field $H(x,t)$ consists of a static selection field $g(x)$ characterized by a field free point as well as a homogeneous dynamic drive field $h(t)$. Together they move the field free point along Lissajous trajectories.

The resulting inverse problem is described by equation 1

$$v = \int_\Omega c(x)(-a * \mu_0 p^R(x)^T \frac{\partial}{\partial T} \bar{m}(x,\cdot))dx - a * \mu_0 \int_{\mathbb{R}^3} p^R(x)^T \frac{\partial}{\partial T} H(x,\cdot)dx \tag{1}$$

with μ_0 being the constant permeability of vacuum, $\Omega \subset \mathbb{R}^3$ the field of view, $p^R : \Omega \mapsto \mathbb{R}^3$ the receive coil sensitivity, $M : \Omega \times [0,\mathrm{T}] \mapsto \mathbb{R}^3$ the particle magnetization, $H : \mathbb{R}^3 \times [0,\mathrm{T}] \mapsto \mathbb{R}^3$ the applied magnetic field, $c : \Omega \mapsto \mathbb{R}_+ \cup 0$ the tracer concentration, $\bar{m} : \Omega \times [0,\mathrm{T}] \mapsto \mathbb{R}^3$ the mean magnetic moment and $a : [-\mathrm{T},\mathrm{T}] \mapsto \mathbb{R}$ an analog filter. Discretization results in a linear system $Ac = v$ with System Matrix $A \in \mathbb{C}^{M\times N}$, M being the number of temporal points per trajectory and N the number of spatial points.

There are two main challenges in MPI: the identification of the mean magnetic moment $\bar{m}$ from given tupels (c, v) is the calibration problem. The imaging problem is the reconstruction of the concentration $c(x)$ from measurements $v(t)$.

1. Model Inexactnesses in Magnetic Particle Imaging

In reality, there is no perfect model. We look at two instances, that introduce model inexactnesses in MPI. Firstly, there exist two different approaches for the determination of the System Matrix. The commonly used measurement-based approach is the most accurate method. However, it is a very time consuming procedure, which has to be repeated for each imaging sequence. The model-based approach does not need a time consuming acquisition and can be applied to arbitrarily fine sampling grids. On the downside, the simulation of the System Matrix introduces inaccuracies.

Secondly, motion like breathing of the examined specimen diminishes the quality of the reconstructions. Ignoring this problem leads to severe motion artifacts. Due to very fast measurement times, the searched-for concentration $c(x,t)$ can be assumed piecewise constant in time.

Commonly used algorithms like the Kaczmarz method with a Tikhonov regularization are not equipped to compensate those model flaws [2] Therefore, there is a need to use more sophisticated algorithms.

2. Regularized Sequential Subspace Optimization

We apply the Regularized Sequential Subspace Opimization combined with Kaczmarz method (RESESOP-Kaczmarz), which is based on the Sequential Subspace Optimization (SESOP). SESOP is an iterative solver equivalent to metric projections onto intersections of hyperplanes [3].

It is possible to introduce a regularization with the help of the uncertainty levels of the noisy data $||v-v^\delta|| \leq \delta$ as well as the inexact forward operator $||A-A^\eta|| \leq \eta$. The idea is to replace the exact hyperplanes by stripes whose widths are chosen based on the corresponding uncertainty levels. Adding Morozov's discrepancy principle results in a regularization method, as proven in [4] and in more detail in [5].

Blanke, Hahn and Wald additionally proposed to combine the usage of local properties of the inverse problem in the regularization as done in RESESOP with Kaczmarz, which enables the combination of sub-problems [5].

3. Numerical Results

To evaluate the ability of RESESOP-Kaczmarz to compensate for model imperfections in the system function, we conduct experiments using two different three-dimensional simulated system matrices. The size of each matrix is 61 × 61 × 5. The first system matrix, referred to as GT, is a fully simulated operator based on model B3 from Kluth et al. [6]. This model serves as the ground truth for our experiment. The second system matrix, denoted as AO, is a less advanced model operator in comparison to the GT model.

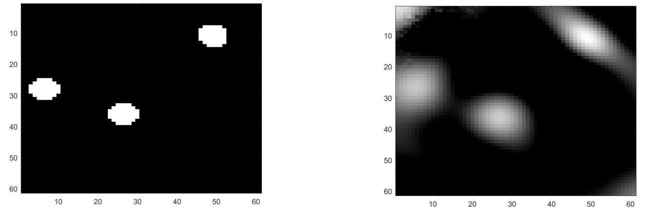

Phantom **AO**: regularized Kaczmarz

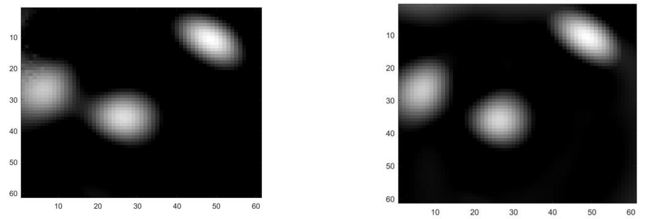

GT: regularized Kaczmarz **AO**: RESESOP-Kaczmarz

Figure 1. Reconstructions with different operators and methods of the given phantom. We depict the same slice of each 3D solution.

The reconstruction quality of regularized Kaczmarz with an imperfect operator is noticeably diminished, particularly at the boundaries and corners of the field of view, as shown in Figure 1. This degradation aligns with the relative operator error. However, RESESOP-Kaczmarz demonstrates the capability to compensate for the model inexactness introduced by the less advanced operator, resulting in a 3D image of nearly the same quality as the ground truth.

Moving on to the algorithm's ability to account for motion, we conduct an experiment using real data from the UKE Hamburg. These three dimensional measurements were obtained using a pre-clinical Bruker scanner and depict a rotating glass capillary with varying rotation frequencies (1 Hz and 7 Hz).

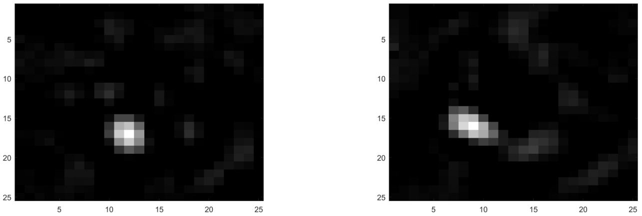

1 Hz rotation frequency. 7 Hz rotation frequency.

Figure 2. 2D slices of the reconstructed image with varying rotation frequencies using Resesop-Kaczmarz

The results presented in Figure 2 exhibit promising improvements compared to the original reconstructions by Gdaniec et al. [2]. However, when dealing with very fast motion, such as a 7Hz rotation, motion artifacts are still visible in the reconstructed images. This occurrence can be attributed to the assumption of a piecewise constant concentration over each trajectory.

Acknowledgement: We gracefully acknowledge financial support by the Deutsche Forschungsgemeinschaft (DFG, project 426078691). We thank Tobias Knopp and his research team at UKE Hamburg for providing real data.

References

[1] B. Gleich, J. Weizenecker, *Tomographic Imaging Using the Nonlinear Response of Magnetic Particles*, Nature **435** (2005), 1214-7.

[2] N. Gdaniec, *Detection and Compensation of Periodic Motion in Magnetic Particle Imaging*, IEEE Transactions on Medical Imaging **36** (2017), 1511-1521.

[3] F. Schoepfer, T. Schuster, A. Louis, *Metric and Bregman projections onto affine subspaces and their computation via sequential subspace optimization methods*, J. Inv. Ill-Posed Problems **15** (2007), 1-29.

[4] F. Schoepfer, T. Schuster, *Fast regularizing sequential subspace optimization in Banach spaces*, Inverse Problems **25** (2009), 015013.

[5] S. Blanke, B. Hahn, A. Wald *Inverse Problems with inexact forward operator: Iterative regularization and application in dynamic imaging*, Inverse Problems **36** (2020).

[6] T. Kluth et al, *Towards accurate modeling of the multidimensional magnetic particle imaging physics*, New Journal of Physics **21** (2019), 103032.

Dealing with field imperfections for field-free line magnetic particle imaging

STEPHANIE BLANKE
(joint work with Christina Brandt)

1. INTRODUCTION

Magnetic particle imaging (MPI) is a tracer-based medical imaging modality invented by Gleich and Weizenecker [1]. Different scanner implementations having different magnetic field properties exist. Regarding field-free line (FFL) scanner [2] and discrete line rotation, the space- and time-dependent magnetic field

$$\mathbf{H}(\mathbf{r},\varphi,t) = \left(-G\,\mathbf{r}\cdot\mathbf{e}_\varphi + A\Lambda_\varphi(t)\right)\mathbf{e}_\varphi\,,$$

features an FFL, which for data generation is sequentially translated through the field of view and rotated in between measurements. Thereby, A and G denote constants determining the maximum displacement of the FFL to the origin $s_{\mathrm{FFL}}\left(t\right) = \frac{A}{G}\Lambda_\varphi\left(t\right)$ with $\Lambda_\varphi\left(t\right)$ being an excitation function usually chosen to be sinusoidal. Further, φ respectively $\mathbf{e}_\varphi$ specifies the direction of the FFL.
Assuming static particle concentrations c as well as spatially homogeneous receive coil sensitivities $\mathbf{p}_l$, the measured voltage signal u_l induced in the l-th receive coil can be expressed in terms of the magnetic permeability μ_0, the mean magnetic moment $\overline{\mathbf{m}}$, and the applied magnetic field $\mathbf{H}$. Using the Langevin model of paramagnetism [3], the signal equation for an FFL scanner thus can be written as

$$u_l\left(\varphi,t\right) = -\mu_0\,\mathbf{e}_\varphi\cdot\mathbf{p}_l\int c(\mathbf{r})\frac{\partial}{\partial t}\overline{m}\left(-G\,\mathbf{r}\cdot\mathbf{e}_\varphi + A\Lambda_\varphi(t)\right)\,\mathrm{d}\mathbf{r}. \tag{1}$$

For convenience we neglect signal filtering and refrain from removing the direct feed-through of the excitation signal. We recommend to consult [3] for further details.
With respect to this measurement setup the scanning geometries of MPI and computerized tomography, a well-known medical imaging technique, become similar. Considering the idealized setting above, it has been shown that MPI data can be traced-back to the Radon transform of the particle concentration [4], i.e. we can write

$$u_l\left(\varphi,t\right) = -\mu_0\,\mathbf{e}_\varphi\cdot\mathbf{p}_l\,A\Lambda'_\varphi(t)\left(\overline{m}'\left(G\,\cdot\right) * \mathcal{R}c\left(\varphi,\cdot\right)\right)\left(s_{\mathrm{FFL}}\left(t\right)\right),$$

where $\mathcal{R}$ denotes the Radon transform mapping c to the set of its line integrals

$$\mathcal{R}c\left(\varphi,s\right) = \int c\left(\mathbf{r}\right)\delta\left(\mathbf{r}\cdot\mathbf{e}_\varphi - s\right)\,\mathrm{d}\mathbf{r}.$$

The aim of our work is to investigate the setting of more realistic assumptions. Here, we concentrate on magnetic field imperfections that might lead to image artifacts when being neglected in the reconstruction process.

2. Methods

The idea is to link ideal and deformed magnetic fields via deformation functions that can be obtained with the aid of image registration techniques. First, we create a link between MPI data and an adapted version of the Radon transform not necessarily integrating along straight lines. To this end, we assume that the real magnetic field can approximately be written in terms of the ideal field using diffeomorphic mappings $\Gamma_{\varphi,t}$, i.e.

$$\mathbf{H}^{\text{real}}(\mathbf{r},\varphi,t) \approx \mathbf{H}^{\text{ideal}}(\Gamma_{\varphi,t}\mathbf{r},\varphi,t)\,. \tag{2}$$

Motivated by the similar scanning geometry, the approach roots from methods applied in dynamic CT (e.g. [5], [6], [7]). Furthermore, to some extent data obtained from measurements with deformed magnetic fields can be reinterpreted as data obtained from measurements with deformed objects. Inserting (2) into the FFL signal equation (1) yields

$$\begin{aligned} u_l^{\text{real}}(\varphi,t) \approx& -\mu_0\,\mathbf{e}_\varphi\cdot\mathbf{p}_l \int c(\mathbf{r})\frac{\partial}{\partial t}\overline{m}\left(-G\,\Gamma_{\varphi,t}\mathbf{r}\cdot\mathbf{e}_\varphi + A\Lambda_\varphi(t)\right)\,\mathrm{d}\mathbf{r}\\ =& -\mu_0\,\mathbf{e}_\varphi\cdot\mathbf{p}_l\,A\Lambda_\varphi'(t)\int c(\mathbf{r})\,\overline{m}'\left(-G\,\Gamma_{\varphi,t}\mathbf{r}\cdot\mathbf{e}_\varphi + A\Lambda_\varphi(t)\right)\,\mathrm{d}\mathbf{r}\\ &+\mu_0\,\mathbf{e}_\varphi\cdot\mathbf{p}_l\,G\int c(\mathbf{r})\left(\Gamma_{\varphi,t}\right)'\mathbf{r}\cdot\mathbf{e}_\varphi\,\overline{m}'\left(-G\,\Gamma_{\varphi,t}\mathbf{r}\cdot\mathbf{e}_\varphi + A\Lambda_\varphi(t)\right)\,\mathrm{d}\mathbf{r}. \end{aligned} \tag{3}$$

For the moment, we presume the second term to be negligible compared to the remaining part. Inspired by [4] and [7], we rewrite our expression for $u_l^{\text{real}}(\varphi,t)$ in terms of an adapted version of the Radon transform $\mathcal{R}^\Gamma$ as

$$u_l^{\text{real}}(\varphi,t) \approx -\mu_0\,\mathbf{e}_\varphi\cdot\mathbf{p}_l\,A\Lambda_\varphi'(t)\left(\overline{m}'(G\,\cdot) * \mathcal{R}^\Gamma c(\varphi,\cdot)\right)\left(s_{\text{FFL}}(t)\right)$$

with

$$\mathcal{R}^\Gamma c(\varphi,s) = \int c(\mathbf{r})\,\delta\left(\Gamma_{\varphi,t}\mathbf{r}\cdot\mathbf{e}_\varphi - s\right)\,\mathrm{d}\mathbf{r}.$$

In the following, we will write $u_l^{\text{real}} = \mathcal{K}_l v^\Gamma$ with $v^\Gamma = \mathcal{R}^\Gamma c$ and $\mathcal{K}_l$ being the corresponding convolution operator.

3. Results

For first proof-of-concept results, we will regard the time- and angle-independent deformation function

$$\Gamma_{\varphi,t}\begin{pmatrix}x\\y\end{pmatrix} = \begin{pmatrix}x\\y-100x^2\end{pmatrix}.$$

Thus, the second term in (3) vanishes. Motivated by [8] we jointly reconstruct Radon data and particle concentration by means of total variation regularization

$$\min_{c\geq 0,\,v^\Gamma\geq 0}\frac{1}{2}\sum_l\left\|\mathcal{K}_l v^\Gamma - u_l^{\text{real}}\right\|_{L_2}^2 + \frac{\alpha_1}{2}\left\|\mathcal{R}^\Gamma c - v^\Gamma\right\|_{L_2}^2 + \alpha_2\,\mathrm{TV}(c) + \alpha_3\,\left\|v^\Gamma\right\|_{L_1}.$$

Ignoring the non-ideal magnetic field by choosing $\Gamma_{\varphi,t} = \mathrm{Id}$, the field deformation transfers to a deformed phantom reconstruction (Figure 1b). Incorporation of the exact $\Gamma_{\varphi,t}$ yields a well-reconstructed image (Figure 1c). Determining the deformation function via linking the ideal and deformed magnetic fields using the image registration package FAIR [9] and the corresponding add-on LagLDDMM [10] available at `https://github.com/C4IR/FAIR.m`, we get promising results (Figure 1d) justifying our approach for dealing with magnetic field imperfections. Next steps would be the investigation of more realistic deformation functions and the application of our method to experimental magnetic field data.

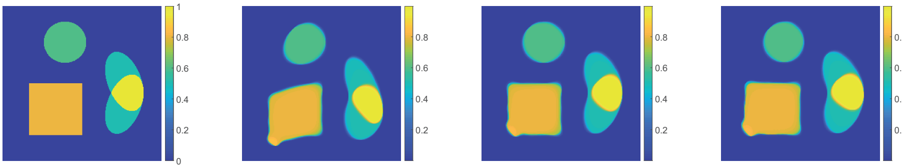

(A) Phantom. (B) $\Gamma_{\varphi,t} = \mathrm{Id}$. (C) Exact $\Gamma_{\varphi,t}$. (D) Estimated $\Gamma_{\varphi,t}$.

FIGURE 1. Phantom reconstructions for different choices for $\Gamma_{\varphi,t}$.

ACKNOWLEDGMENT

The authors acknowledge the support by the Deutsche Forschungsgemeinschaft (DFG) within the Research Training Group GRK 2583 “Modeling, Simulation and Optimization of Fluid Dynamic Applications”.

REFERENCES

[1] B. Gleich, J. Weizenecker, *Tomographic imaging using the nonlinear response of magnetic particles*, Nature **435** (2005), 1214–1217.
[2] J. Weizenecker, B. Gleich, and J. Borgert, *Magnetic particle imaging using a field free line*, Journal of Physics D: Applied Physics **41** (2008), 105009.
[3] T. Knopp, T.M. Buzug, *Magnetic particle imaging: an introduction to imaging principles and scanner instrumentation*, Springer (2012).
[4] T. Knopp, M. Erbe, T.F. Sattel, S. Biederer, T.M. Buzug, *A Fourier slice theorem for magnetic particle imaging using a field-free line*, Inverse Problems **27** (2011), 095004.
[5] B. Hahn, *Reconstruction of dynamic objects with affine deformations in computerized tomography*, Journal of Inverse and Ill-posed Problems **22** (2014), 323–339.
[6] B.N. Hahn, *Motion Estimation and Compensation Strategies in Dynamic Computerized Tomography*, Sensing and Imaging **18** (2017), 1–20.
[7] B.N. Hahn, *Motion Compensation Strategies in Tomography* in *Time-dependent Problems in Imaging and Parameter Identification*, Springer (2021), 51–83.
[8] R. Tovey, M. Benning, C. Brune, M.J. Lagerwerf, S.M. Collins, R.K. Leary, P.A. Midgley, and C.-B. Schönlieb, *Directional sinogram inpainting for limited angle tomography*, Inverse Problems **35** (2019), 024004.
[9] J. Modersitzki, *FAIR: flexible algorithms for image registration*, SIAM (2009).
[10] A. Mang, L. Ruthotto, *A Lagrangian Gauss–Newton–Krylov Solver for Mass- and Intensity-Preserving Diffeomorphic Image Registration*, SIAM Journal on Scientific Computing **39** (2017), B860–B885.

Retrospective Redundancy-based motion estimation in MRI using Deep CNNs

Mathias S. Feinler
(joint work with Bernadette N. Hahn)

Suitable algorithms for motion correction are highly relevant for medical imaging applications such as Magnetic Resonance Imaging (MRI). During data acquisition involuntary motion can occur due to non-cooperative patients or induced by respiratory and cardiac motion. Since most procedures are designed for a static setup, the most convenient way of motion compensation is a retrospective one.

The motion affected data acquisition can be modelled as

$$y^c(t) = A(t)\mathcal{F}[S_c U(s,t)] =: \mathcal{A}(U,s,t), \qquad c = 1,\dots,N^{\text{coils}}$$

where the deformations $U \in \mathcal{D}_{\text{U}}$ and the image $s \in \mathcal{D}_{\text{s}}$ are unknowns, $\mathcal{F}$ is the Fourier transform and $A(t)$ specifies which Fourier coefficient is acquired at time t. We assume that coil sensitivities S_c are available by some pre-computation procedure [2] and only time dependent data y^c are available. By artificially separating the data, bearing in mind that the continuous data acquisition allows us to balance the temporal resolution retrospectively, we can write the data acquisition as

$$y_i^c = A_i\mathcal{F}[S_c U_i(s)], \qquad i = 1,\dots,N^{\text{exc}}, \quad c = 1,\dots,N^{\text{coils}}$$

using the assumption that the object is quasi static during the acquisition of some small subset of Fourier coefficients specified by the sampling pattern A_i.

We aim to reconstruct the image s as well as deformation-fields $U = \{U_i\}_{i=1}^{N^{\text{exc}}}$ from a single acquisition of one slice in MRI.

To enable motion estimation in a verifiable manner, we need redundantly sampled information. This can be achieved by the selection of sampling patterns A_i. For the static case several attempts have been made to find optimal sampling patterns for sparse reconstruction [3]. For the dynamic case it is still an open issue to find an optimal sampling pattern that guarantees successful motion estimation for predefined spaces of deformations and images.

A radial acquisition scheme is well-known to be slightly motion resistant. The angle of each spoke can be chosen according to a greedy criterion w.r.t the coverage of the k-space. Thus, if we combine consecutive spokes we achieve a homogeneous coverage of the k-space. Since for rotations of the image, the k-space is rotated as well, we can guarantee that, using coil sensitivity information, the central part of the k-space is sampled redundantly. This enables redundancy based motion estimation [1].

1. Methodology

Motion estimation is mostly formulated in variational form. The problem is that local optima could prevent global convergence to the desired solution when local optimization techniques are used. Therefore, we first focus on the prediction of coarse estimates for the true deformation fields. Using prohibitively sparse data $y_i = \{y_i^c\}_c$ we can compute CG-SENSE reconstructions s_i. Even though we cannot expect to recover the true image s in high quality, the coarse configuration is usually already encoded. By comparison of all s_i we are able to infer coarse deformation estimates using a Deep CNN. The used network architecture resembles FlowNet 2.0 [4] where now in contrast all images $\{s_i\}_{i=1}^{N^{\mathrm{exc}}}$ are plugged in at once.

In case of challenging deformations like free form deformations, this estimate has to be refined further. It is crucial to use a projected gradient descent procedure, since a pure application of gradients not necessarily leads to compliant deformations. This projection procedure is, dependent on the space of deformations, hard to implement in an analytic manner. Instead, a neural network can be used to learn a suitable projection operation by using training data that samples this space.

The refinement can be pursued via unrolled iterative or multiscale procedures.

2. RESULTS

We apply the proposed procedure to simulated MRIs of the abdomen. To model potential breathing motion for MRIs of the abdomen, we use free form deformations. Only after the correction procedure, the estimated motion allows to produce reconstructions with sharp edges. Results are visualized in Figure 1.

After the motion estimation procedure, the residual value

$$y^c(t) - \mathcal{A}(\bar{U}, \bar{s}, t)$$

can be computed, where $\bar{s}$ and $\bar{U}$ are the predicted image and deformation-fields, respectively. Even if convergence can not be guaranteed for this procedure, the residual value together with the appearance of the predicted deformations allows to verify the plausibility of the predicted reconstruction. This is for instance crucial to allow a reliable diagnosis in medical imaging.

static reconstruction

predicted image

predicted deformation-field

FIGURE 1. Result of proposed procedure on a simulated motion corrupted MRI of the abdomen using synthetic free form deformations, 5% additive Gaussian measurement noise, $N^{\mathrm{exc}} = 16$, image resolution 192×192.

References

[1] M.S. Feinler and B.N. Hahn *Retrospective Motion Correction in Gradient Echo MRI by Explicit Motion Estimation Using Deep CNNs*, arXiv, (2023), 2303.17239.

[2] M.J. Allison, S. Ramani, and J.A. Fessler, *Accelerated regularized estimation of mr coil sensitivities using augmented lagrangian methods*, IEEE Trans. Med. Imaging, **32** (2013), 556–564.

[3] F. Sherry et al., *Learning the Sampling Pattern for MRI*, IEEE Trans. Med. Imaging, **39**, 12, (2020), 4310–4321.

[4] E. Ilg et al., *Flownet 2.0: Evolution of optical flow estimation with deep networks*, arXiv, (2016), 1612.01925.

Convergent Data-driven Regularization for CT Reconstruction

SAMIRA KABRI

(joint work with Alexander Auras, Danilo Riccio, Hartmut Bauermeister,
Martin Benning, Michael Moeller, Martin Burger)

In the context of inverse problems, regularization is the key tool for stable reconstruction of unknown data from noisy measurements. Examples range from general formulations, such as Tikhonov regularization, to model specific approaches, like incorporating regularizing filters into filtered back-projection. In applications where hand-crafting a precise mathematical description of the considered data spaces is impractical to impossible, data-driven approaches aim to find suitable regularizers by exploiting the structure of a finite set of data examples (see [1] for an overview).

We consider compact linear operators $A : \mathcal{U} \to \mathcal{V}$ on two Hilbert spaces $\mathcal{U}, \mathcal{V}$ and denote its nullspace by $\mathcal{N}(A)$ and its range by $\mathcal{R}(A)$. Such operators can be decomposed into a singular system $\{\sigma_n;\ u_n,\ v_n\}_{n\in\mathbb{N}}$, where $\sigma_n > 0$ are the singular values in non-increasing order, $\{u_n\}_{n\in\mathbb{N}} \subset \mathcal{U}$ and $\{v_n\}_{n\in\mathbb{N}} \subset \mathcal{V}$ form orthonormal bases of $\mathcal{N}^\perp(A) \subseteq \mathcal{U}$, or $\mathcal{R}(A) \subseteq \mathcal{V}$, respectively, and

$$Au = \sum_{n\in\mathbb{N}} \sigma_n \langle u, u_n\rangle u_n.$$

For such operators A with an infinite dimensional range, the Moore-Penrose inverse $A^\dagger : \mathcal{D}(A^\dagger) := \mathcal{R}(A)\dot{+}\mathcal{R}(A)^\perp \to \mathcal{N}(A)^\perp$, which is defined for $f \in \mathcal{D}(A^\dagger)$ by

$$A^\dagger f = \sum_{n\in\mathbb{N}} \frac{1}{\sigma_n}\langle f, v_n\rangle u_n,$$

is discontinuous, which leads to uncontrollable reconstruction errors, even for very small measurement errors. Therefore, for noisy measurements $f^\delta = Au + \nu$, where u is a random variable, drawn from a data distribution and ν is a random variable, drawn from a distribution with zero mean that is parametrized by $\delta > 0$, we want to analyze the linear spectral regularizer

$$R(f^\delta, \bar{g}) = \sum_{n\in\mathbb{N}} \bar{g}(\sigma_n)\langle f^\delta, v_n\rangle u_n,$$

where the function $\bar{g} : \mathbb{R}_0^+ \to \mathbb{R}_0^+$ minimizes the expected squared L^2-error with respect to the data and noise distributions, i.e.,

$$\bar{g} \in \operatorname*{argmin}_{g:\mathbb{R}_0^+ \to \mathbb{R}_0^+} \mathbb{E}_{u,\nu}\left[\|u - R(f^\delta, g)\|^2\right]. \tag{1}$$

Due to the simple structure of the regularizer, the minimizing function is unique at the evaluation points σ_n and can be computed explicitely as

$$\bar{g}(\sigma_n) = \frac{\sigma_n}{\sigma_n^2 + \frac{\Delta_n}{\Pi_n}}$$

with $\Pi_n = \mathbb{E}_u\left[\langle u, u_n\rangle^2\right]$ and $\Delta_n = \mathbb{E}_\nu\left[\langle \nu, v_n\rangle^2\right]$, as long as $\Pi_n, \Delta_n > 0$ for all $n \in \mathbb{N}$.

We show that under reasonable conditions, the resulting family of operators are a regularization method in the stochastical sense.

Assumption 1. *The variance of the noise is bounded by δ^2, more precisely,*

$$\sup_{n\in\mathbb{N}} \Delta_n = \delta^2.$$

Assumption 2. *The data is smoother than the considered noise, more precisely there exist $c > 0$ and $n_0 \in \mathbb{N}$ such that*

$$\Delta_n \geq c\,\delta^2\,\Pi_n$$

for all $n \geq n_0$ and $\delta > 0$, where we note that Δ_n depends on δ in the sense of Assumption 1

Assumption 3. *The sequence of Π_n is summable, i.e., $\sum_n \Pi_n < \infty$.*

Under these assumptions, the obtained reconstruction operator is a regularization method, meaning it is continuous and converges to the Moore-Penrose inverse in the no-noise limit.

Theorem. *Let Assumptions 1-3 hold. Then $R(\cdot;\,\bar{g})$ is continuous and*

$$\lim_{\delta\to 0} \mathbb{E}_\nu\left[\left\|A^\dagger f - R\left(f^\delta, \bar{g}\right)\right\|^2\right] = 0$$

for every $f \in \mathcal{D}(A^\dagger)$.

Proof. The proof can be found in [2, Thm. 3]. □

Although the data-driven regularizer is chosen to be optimal with respect to (1), it introduces a bias towards smoother reconstructions. This can be illustrated by computing the variance coefficients of the reconstructed data, i.e.,

$$\tilde{\Pi}_n = \mathbb{E}_{u,\nu}\left[\left\langle R(f^\delta, \bar{g}), u_n\right\rangle^2\right].$$

Inserting Assumption 2 reveals that

$$\tilde{\Pi}_n = \frac{\sigma_n^2 \Pi_n}{\sigma_n^2 \Pi_n + \Delta_N} \Pi_n \leq \frac{1}{1 + \frac{c\delta^2}{\sigma_n^2}} \Pi_n,$$

thus, compared to the original data, the variance of the reconstructions is damped to account for the noise. Since the singluar values σ_n decrease with increasing n, this effect is stronger for higher frequencies and can therefore be interpreted as oversmoothing. Despite the simple form of the considered regularizer, it appears naturally in practical applications, for example in filtered back-projection, where the function to optimize in dependence on given data would be the so-called filter.

In the future, we would like to extend the considered framework to more general approaches which could allow for lower computational costs and a higher expressivity of the obtained regularizers. A first direction could be to substitute the singular value expansion by a diagonal frame decomposition, which have been studied in [3]. Furthermore, to strengthen the connection to supervised learning, we want to study how well the regularizers generalize in the case of finite data.

References

[1] S. Mukherjee, A. Hauptmann, O. Öktem, M. Pereyra, C.B. Schönlieb, *Learned Reconstruction Methods With Convergence Guarantees: A survey of concepts and applications.* IEEE Signal Processing Magazine, 40(1), 164-182 (2023) `https://arxiv.org/abs/2206.05431`

[2] S. Kabri, A. Auras, D. Riccio, H. Bauermeister, M. Benning, M. Moeller, and M. Burger, *Covnergent Data-driven Regularizations for CT Reconstruction* (2022), `https://arxiv.org/abs/2212.07786`

[3] A. Ebner, J. Frikel, D. Lorenz, J. Schwab, M. Haltmeier, *Regularization of Inverse Problems by Filtered Diagonal Frame Decomposition* (2022) `https://arxiv.org/abs/2008.06219`

Uncertainty Quantification of Inclusion Boundaries

Yiqiu Dong
(joint work with Babak M. Afkham, Nicolai A. Riis, Per Christian Hansen)

Computed tomography (CT) imaging is the task of reconstructing a positive attenuation field (in the form of an image) from a finite number of projections (e.g., sinograms). CT reconstruction is often followed by an image segmentation step to partition the image into piecewise smooth/constant regions. The boundaries between such regions often carry valuable information.

In this talk, we will describe a Bayesian framework for reconstructing the boundaries of piecewise constant regions in the CT problem in an infinite-dimensional setting. Since the regularity of boundaries carries crucial information in many inverse problem applications, e.g., in medical imaging for identifying malignant tissues or in the analysis of electroencephalogram for epileptic patients, we characterize the regularity of the boundary by means of its fractional differentiability. The proposed Bayesian formulation has a hierarchical structure, which simultaneously estimates the boundary and its regularity. In addition, we quantify the uncertainties in the estimates.

Our approach is goal oriented, meaning that we directly detect the discontinuities from the data, instead of reconstructing the entire image. This drastically reduces the dimension of the problem, which makes the application of Markov Chain Monte Carlo (MCMC) methods feasible.

We will show that the proposed method provides an excellent platform for challenging X-ray CT scenarios (e.g., in case of noisy data, limited angle, or sparse angle imaging). Furthermore, this framework can be extended to reconstruct 2D surfaces, track the changes of the boundaries, and handle other types of noise. This work has been published or submitted, see [1, 2].

REFERENCES

[1] B. M. Afkham, Y. Dong, P. C. Hansen, *Uncertainty Quantification of Inclusion Boundaries in the Context of X-Ray Tomography*, SIAM Journal on Uncertainty Quantification **11** (2023), 31–61.

[2] B. M. Afkham, N. A. Riis, Y. Dong, P. C. Hansen, *Inferring Features with Uncertain Roughness*, Submitted, http://arxiv.org/abs/2305.04608.

A Bayesian level-set inversion method for simultaneous reconstruction of absorption and diffusion coefficients in diffuse optical tomography

ANUJ ABHISHEK
(joint work with Thilo Strauss, Taufiquar Khan)

Diffuse Optical Imaging (DOT) is a non-destructive medical imaging modality used to probe bio-medical tissues. In a DOT system, we illuminate the surface of the medium we are interested in imaging, by low-energy infra-red light by guiding the light through certain optical fiber channels called optodes. As the light is propagated through the medium, we measure the transmitted intensity at other optode locations. Based on such boundary measurements, the idea is to reconstruct the following two optical characteristics of the medium: diffusion (or, scattering) and absorption. This allows us to detect anomalies in the interior, e.g. the diffusion parameter of a tumor is different from that of surrounding healthy tissues and likewise the absorption coefficient of a benign tumor may be different from that of a malignant tumor. One may find more details about the use of DOT in the field of medical imaging in the following references [1, 2].

One particularly useful mathematical model for studying DOT is the so-called frequency diffusion approximation to the Radiative Transfer Equation. In this model, the photon density $u(x)$ in the medium Ω is related to the diffusion and absorption effects by the following equation,

$$-\nabla \cdot (a(x)\nabla u(x)) + \left(b(x) + i\frac{\omega}{c}\right) u(x) = 0 \quad \text{in } \Omega. \tag{1}$$

Here ω is the laser modulation frequency, which is non-zero in the alternating current case, whereas, $\omega = 0$ in the direct current case. Note that in the equation above, c is the speed of light, $a(x)$ is the diffusion coefficient, and $b(x)$ is the absorption coefficient. For setting up the inverse problem in this work, we study the model under the assumption that $\omega = 0$. Thus the equation under study is:

$$-\nabla \cdot (a(x)\nabla u(x)) + b(x)u(x) = 0 \quad \text{in } \Omega. \tag{2}$$

Before we describe the discrete measurement set-up for the inverse problem, we will describe an idealized inverse problem with Neumann and Robin data. In an idealized inverse problem set-up, we assume knowledge of *all* possible Robin and Neumann data pairs on the boundary $\partial\Omega$, i.e., $-a\frac{\partial u}{\partial \nu}|_{\partial\Omega}$ is the source photon density (Neumann data) going into the medium through the boundary and $(u(x) + 2a\frac{\partial u}{\partial \nu})|_{\partial\Omega}$ is the measured photon density (Robin data) on the boundary respectively. The goal is to then infer the coefficients $a(x)$, and $b(x)$ from such boundary measurements, given equation (2) is satisfied. However, in [3] it was shown that if $a(x)$ and $b(x)$ are smooth and $a(x) = 1$ near the boundary $\partial\Omega$, then there is a non-uniqueness in the solution for the inverse problem. In spite of this non-uniqueness result for the case of smooth parameters, in [4] it was shown that if one considers $a(x)$ which are piecewise constants and $b(x)$ is piecewise analytic, then the inverse problem has a unique solution.

Inspired by this result, in our present work we consider a Bayesian inference method for reconstruction of optical parameters, $a(x)$ and $b(x)$ that are piecewise constants. For this we consider the case where diffusive and absorptive coefficients are expressed as:

$$a(x) = \sum_{i=1}^{M} a_i \mathbb{I}(\Omega_i^d), \qquad b(x) = \sum_{i'=1}^{N} b_{i'} \mathbb{I}(\Omega_{i'}^a) \tag{3}$$

for some $M, N \in \mathbb{N}$. Here, $\mathbb{I}(S)$ denotes the characteristic function of some set $S \subset \Omega$. Also, for $i \neq k$, and $i' \neq k'$, $\Omega_i^d \cap \Omega_k^d = \emptyset$, $\Omega_{i'}^a \cap \Omega_{k'}^a = \emptyset$. Besides, $\cup_{i=1}^{M} \Omega_i^d = \Omega = \cup_{i'=1}^{N} \Omega_{i'}^a$. The constants a_i and $b_{i'}$ are bounded, strictly positive numbers such that $a(x) \in \mathcal{A}(\Omega)$ and $b(x) \in \mathcal{A}(\Omega)$.

We will now describe the semi-discrete mathematical formulation of the problem, similar to that introduced for electrical impedance tomography (EIT) [5]. Let $\Omega \in \mathbb{R}^2$ be the region to be imaged with its boundary denoted by $\partial\Omega$. Let the photon-density measurements be made on L optodes, $\{O_l\}_{l=1}^{L}$, placed along $\partial\Omega$. We will denote by U_l, the measured photon density on the l^{th} optode and by $\bar{F}_l$, the average photon density across the l^{th} optode. We assume that the parameters $a(x)$, $b(x)$ are real valued, positive, bounded functions in $L^\infty(\bar{\Omega})$. The measurement set-up is then given by:

$$-\nabla \cdot (a(x)(\nabla u(x))) + b(x)u(x) = 0, \quad x \in \Omega \tag{4}$$

$$u(x) + 2a\frac{\partial u}{\partial \nu} = U_l, \quad x \in O_l, \quad l \in \{1, \ldots, L\} \tag{5}$$

$$a\frac{\partial u}{\partial \nu} = 0 \quad \text{on } \partial\Omega \setminus \bigcup_{l=1}^{L} O_l. \tag{6}$$

We also assume that the average value of applied photon density on each optode, denoted by $\bar{F}_l = \frac{1}{|O_l|}\int_{O_l} -a\frac{\partial u}{\partial \nu} dS$ is known. Here dS is the surface measure on $\partial\Omega$ and $|O_l|$ is the surface measure of the l^{th} optode O_l. Since $|O_l|$ is known, hence we assume that the applied photon flux satisfies:

$$\int_{O_l} -a\frac{\partial u}{\partial \nu} dS = F_l \tag{7}$$

where $F_l = \bar{F}_l \times |O_l|$. Formally, for each $j \in \{1, \dots, J\}$, let us represent the true photon density, $U^{(j)}$, corresponding to the applied flux $F^{(j)}$ on the optodes by:

$$U^{(j)} = \mathcal{G}_j(a, b) \tag{8}$$

Consider the case, when the measured data is corrupted by a Gaussian noise. Let y_j denote the noisy measurements of the photon density on the boundary:

$$y_j = \mathcal{G}_j(a, b) + \eta_j; \quad j \in \{1, \dots, J\} \quad \text{and } \eta_j \sim N(0, \Gamma_0) \ \textit{i.i.d.} \tag{9}$$

Here $N(0, \Gamma_0)$ is used to denote a Gaussian random variable with mean 0 and variance Γ_0. Concatenating all the vectors $y_j \in \mathbb{R}^L$ we can write:

$$y = \mathcal{G}(a, b) + \eta \tag{10}$$

where $y \in \mathbb{R}^{LJ}$ and $\eta \sim N(\mathbf{0}, \Gamma)$ where $\Gamma = \mathrm{diag}(\Gamma_0, \dots, \Gamma_0)$. The statistical inverse problem can now be formulated as recovery of the parameters, a and b, from observed (noisy) data y.

In this work, we prove that the Bayesian inverse problem so stated is well-posed wherein we use level set-prior models for the optical parameters $a(x)$ and $b(x)$. This follows the paradigm introduced in [6, 7]. Furthermore, we also provide a numerical implementation of the proposed method which is based on an MCMC sampling strategy devised in [8] for sampling very high dimensional spaces.

REFERENCES

[1] S. Arridge, *Optical tomography in medical imaging*, Inverse Problems **15** (1999), R41–R93.

[2] S. Arridge, J. Schotland *Optical tomography: forward and inverse problems*, Inverse Problems **25** (2009).

[3] S. Arridge, W. Lionheart *Nonuniqueness in Diffusion-Based Optical Tomography*, Optics letters **23** (1998).

[4] B. Harrach, *On uniqueness in diffuse optical tomography*, Inverse Problems **25** (2009).

[5] M. Cheney,D. Isaacson, E. Somersalo *Existence and uniqueness for electrode models for electric current computed tomography*, SIAM Journal on Applied Mathematics **52** (1992).

[6] A. Stuart, *Inverse problems: a Bayesian perspective*, Acta Numerica **19** (2010).

[7] M. Dunlop,A. Stuart, *The Bayesian formulation of EIT: analysis and algorithms*, Inverse Problems and Imaging **10** (2016).

[8] S. Cotter, G. Roberts, A. Stuart,A. White *MCMC methods for functions: modifying old algorithms to make them faster*, Statistical Science. A Review Journal of the Institute of Mathematical Statistics **28** (2013).

Recent approaches in nano-CT using inexact models and deep learning

ANNE WALD

(joint work with Stephanie Blanke, Bernadette Hahn-Rigaud, Florian Hartmann, Alice Oberacker)

We consider an inverse problem

$$A(f) = g, \quad A : \mathcal{D}(A) \subseteq X \to Y,$$

where the given data g^δ are subject to noise with *noise level*

$$\|g^\delta - g\| \leq \delta.$$

In addition, we assume that only an *inexact version* A^η of A is given with *inexactness* $\eta > 0$, such that

$$\|A^\eta(f) - A(f)\| \leq \eta \cdot \rho \quad \text{for all } f \in B_\rho(0) \subseteq \mathcal{D}(A).$$

In particular, we consider linear inverse problems

$$A^{(t)} f = g(t)$$

with *time-dependent data* $g(t)$ and *forward operator* $A^{(t)}$. The quantity f is assumed to be static.

If measurements are taken at time instances t_k, $k = 1, ..., K$, we obtain the *semi-discrete setting*

$$A_k f = g_k, \quad \|A_k - A_k^\eta\| \leq \eta_k, \quad \|g - g^{\delta_k}\| \leq \delta_k \quad k = 1, ..., K,$$

where $A^{(t_k)} \rightsquigarrow A_k$.

- If the model is accurate at $t = t_k$, we choose $\eta(t_k) = 0$.
- Changes in the physical setting may be incorporated in the choice of η.
- Periodic time-dependent changes in the model lead to periodic functions $\eta(t)$.

As an example, we consider *motion in computerized tomography (CT)*: The investigated object undergoes a *deformation during data acquisition.*
Typical examples from medicine:

- Breathing: periodical deformation of the entire body (global motion)
- Heartbeat: local periodical motion

Motion in nano-CT:

- relative motion between object and scanner due to, e.g., vibrations, manufacturing tolerances, object drift

In dynamic CT, we interpret the motion of the object as a model inexactness in comparison to a static problem:
We consider the dynamic model for an X-ray beam, parametrized by the angle φ of the tomograph and the detector point s,

$$g^\Gamma(\varphi, s) = R^\Gamma f_0(\varphi, s) = \int_{\mathbb{R}^2} f_0(\Gamma_\varphi x)\delta(s - x^T\omega(\varphi))\,\mathrm{d}x,$$

where Γ is the (unknown) motion, f_0 is the initial state of the object, and R^Γ is the dynamic Radon operator. For the inexactness η in

$$\left\|R^\Gamma(\varphi, s) - R(\varphi, s)\right\| \leq \eta(\varphi, s)$$

we have several options:

- $\eta(\varphi, s) = \bar{\eta}$ with some constant $\bar{\eta} > 0$
- $\eta(\varphi, s) = \eta(\varphi)$: inexactness depends on the position of the tomograph, i.e., on time
- $\eta(\varphi, s) = \eta(s)$: inexactness depends on offset and is affected by local behavior of the object
- $\eta(\varphi, s) = \eta(\varphi, s)$: local time-dependent inexactness

To solve such inverse problems in dynamic computerized tomography, for example in nano-CT, we adapt sequential subspace optimization (see, e.g., [1]) as a regularization technique for semi-discrete linear inverse problems with inexact forward operators as presented in [2]. We present numerical results for simulated as well as real measured data.

In addition, we show that using sequential subspace optimization and local modelling errors may yield a basis for motion identification as well as data-driven post-processing to improve the reconstruction quality.

References

[1] T. Schuster, F. Schöpfer, A. K. Louis, *Metric and Bregman projections onto affine subspaces and their computation via sequential subspace optimization methods*, Journal of Inverse and Ill-Posed Problems **16** (2008), 479–506.

[2] S. E. Blanke, B. N. Hahn, A. Wald, *Inverse problems with inexact forward operator: iterative regularization and application in dynamic imaging*, Inverse Problems **36** (2020), 124001.

Ill-Posed Inverse Problems in Low-Dose Dental Cone-Beam Computed Tomography

Jin Keun Seo

(joint work with Hyoung Suk Park)

Dental cone-beam computed tomography (CBCT) is a specialized type of CT imaging device designed specifically for dental applications. Recently, low-dose dental cone-beam computed tomography (CBCT) has become an increasingly popular imaging technique in dental clinics as an alternative to standard multi-detector CT (MDCT). This is due to several advantages of CBCT, including: (i) lower cost, as dental CBCT is typically less than one-tenth the cost of MDCT; (ii) greater convenience for patients, as they can be scanned while seated or standing, requiring less space in the dental office; and (iii) lower radiation exposure for patients, as dental CBCT exposes them to less radiation than MDCT.

However, the advantages of dental CBCT come at the expense of reduced data quality and more ill-posed inverse problem compared to MDCT. Dental CBCT systems use a fixed array of detectors and scan the head in one revolution, taking longer than MDCT's continuous table movement with a fast rotation time. This longer scanning time can result in motion artifacts. In order to obtain a larger field of view while using a small detector, most dental CBCT devices utilize an offset detector with a short subject-to-detector distance. However, this short distance between the subject and detector can result in scattering and cone-beam artifacts, which can negatively impact the quality of the reconstructed image.

Due to the prevalence of metallic implants in dental patients, metal artifact reduction (MAR) is a critical issue in dentistry. However, MAR is a highly challenging, non-linear problem in dental CBCT. This is because the global structure of metal artifacts is influenced not only by local metal geometry, but also by various complex factors associated with metal-bone and metal-teeth interactions, FOV truncation, scattering, and nonlinear partial volume effects, among others. Metallic objects in the CBCT field of view produce streaking artifacts that significantly degrade the reconstructed CT image, resulting in a loss of crucial information on the teeth and other anatomical structures.

Developing robust CT reconstruction algorithms using MAR is a complex and challenging task that involves addressing uncertainties resulting from the forward model mismatch. Despite several MAR methods that have been suggested over the last four decades, existing approaches may not be sufficient to effectively reduce metal artifacts in low-dose dental CBCT environments, emphasizing the critical need for further research in this area.

A dental CBCT scan involves directing a cone-shaped X-ray beam through a patient's head as they are positioned between an X-ray source and a flat-panel detector. The X-ray source and detector are housed in a gantry that is rotated, allowing the beam to pass through the patient's head from various angles. As the beam passes through the patient, a planar detector acquires the CBCT projection data denoted as $\mathrm{P}(\varphi, u, v)$, where $\varphi \in [0, 2\pi)$ represents the projection angle, and (u, v) represents the position of the planar detector. The position is scaled using the ratio of the distance between the X-ray source and the detector plane to the distance between the source and the rotation axis.

The incident X-ray beams used in most dental CBCT scans consist of photons with varying energies, ranging from the minimum energy (e.g., 0 keV) up to the peak energy (e.g., between 60 keV and 120 keV). The X-ray attenuation coefficients denoted by μ also vary with the photon energy level E, where the μ value of metal objects exhibits significant variation with E, while the μ of soft tissue remains relatively constant with E. Consider a path of the X-ray beam from a source position $\mathbf{o}_\varphi$ to a detector position $\boldsymbol{x}_{\varphi,u,v}$ in the world coordinates. Due to the polychromatic nature of X-ray beams, the projection data $\mathrm{P}(\varphi, u, v)$ follows the Lambert-Beer law [1, 3]:

$$(1) \qquad \mathrm{P}(\varphi, u, v) = -\ln\left(\int_{\mathbb{R}} \eta(E)\exp(-\alpha\int_0^1 \mu((1-s)\mathbf{o}_\varphi + s\boldsymbol{x}_{\varphi,u,v})ds)dE\right),$$

where $\alpha = \|\mathbf{o}_\varphi - \boldsymbol{x}_{\varphi,u,v}\|$ represents the distance between the source and the detector cell, and $\eta(E)$ represents the fractional energy at photon energy E in the spectrum of the X-ray source [5], with its support being the interval $[E_{min}, E_{max}]$, and $\int_{\mathbb{R}} \eta(E)dE = 1$. When the X-ray beam encounters a metal object, the higher energy photons are absorbed less compared to the lower energy photons, resulting in a *beam hardening* effect. As a result, the lower energy photons are absorbed more, while the higher energy photons penetrate through the metal object, causing distortion in the CT image. This can lead to streak-like artifacts extending from the metal object.

All existing CT reconstruction methods are typically based on the monochromatic assumption, where $\eta(E)$ is simplified to a Dirac delta function, representing a single energy value. Under this idealized assumption, there exists a linear X-ray transform denoted by $\mathcal{T}_{\text{forward}}$, such as the Radon transform or cone-beam transform, that maps the CT image to the projection data as follows:

$$\mathrm{P} = \mathcal{T}_{\text{forward}}\ \mu. \tag{2}$$

The CT image μ can then be reconstructed by inverting the forward operator. The standard reconstruction methods, such as the filtered back-projection (FBP) algorithm [2] and Feldkamp-Davis-Kress Algorithm (FDK) [4], can be viewed as an inverse of the forward operator $\mathcal{T}_{\text{forward}}$, which assumes that the data P lies in the range space of the forward operator. However, in practical dental CBCT scenarios, the data P associated with polychromatic X-ray beams does not necessarily lie in the range space of the forward operator. Hence, there is no CT image μ that satisfies the forward model (2) and the inconstent data P results in the model mismatch:

$$(\mathcal{T}_{\text{forward}}^{-1}\mathcal{T}_{\text{forward}})\mathrm{P}\ \neq\ \mathrm{P}. \tag{3}$$

Due to this mismatch, the process of projecting the data into the range space during the inversion of the forward operator often generates artifacts, such as streaking and shadowing artifacts. These artifacts are spread globally, resulting in overall degraded image quality.

Recently, there have been numerous attempts to leverage deep learning approaches as heuristic image regularizers, and these methods have shown remarkable performance in sparse-view CT scenarios. However, their efficacy in dental CBCT environments is limited when there are multiple metal inserts occupying a significant area. Existing methods that rely on initially reconstructed images by the standard reconstruction algorithm appear to have fundamental limitations in our setting due to the highly corrupted input images in neural networks. Therefore, it is crucial to reconsider the standard reconstruction algorithms, such as FDK and FBP, which are designed based on the ideal forward model (2). This model assumes that the data lies in the range space of the forward operator, which is an idealistic assumption. However, in practical scenarios, there is often a discrepancy between this ideal assumption and the actual data, resulting in serious artifacts in the reconstructed images. These artifacts are widespread and can lead to overall degraded image quality. Lessons learned from the last three decades have shown that conventional regularization methods struggle to effectively handle severe artifacts.

Taking inspiration from the recent success of neural radiance fields (NeRF) in computer vision [6], one may consider to utilize a neural representation of CT images while accounting for the energy dependence of the attenuation distribution. Unlike traditional approaches that rely on the inversion formula, neural representation focuses on a compact 3D CT image representation denoted by f_Θ, which maps a 3D point $\boldsymbol{x} = (x, y, z)$ to a scalar value $\mu(\boldsymbol{x})$ representing the attenuation coefficient at position $\boldsymbol{x}$, where the parameter Θ determines the function f within the neural network. Using the function f_Θ as a neural network instead of the standard point-wise expression μ is crucial because it provides a much more compact representation, while still giving the same $\mu(\boldsymbol{x})$ value. This compact implicit expression allows for the solution of highly ill-posed inverse problems, which is a significant advantage of MAR-NeRF over traditional methods.

References

[1] A. Beer, *Betimmug der absoption des rothen lichts in farbigen flussigkeiten*, Annalen der Physik (1852)

[2] O. G. Bracewell, *Symposium on the physico-chemical transformation of sulphur compouns in the atmosphere and formation of acid smogs*, Mainz Germanyu (1967)

[3] J. H. Lambert and E. Anding, *Lamberts Photometrie: Photometria, Sive De Mensura et Gradibus Luminis, Colorum et Umbrae*, W. Engelmann (1892)

[4] L.A . Feldkamp, L. C. Davis, and J. W. Kress, *Practical cone-beam algorithm*, JOSA A, 1(6):612–619 (1984)

[5] G. T. Herman and S. S. Trivedi, *A comparative study of two postreconstruction beam-hardening correction methods*, IEEE Transactions on Medical Imaging (1983)

[6] R. Martin-Brualla, N. Radwan, M. S. Sajjadi, J. T. Barron, A. Dosovitskiy, and D. Duckworth *Nerf in the wild: Neural radiance fields for unconstrained photo collections*, Proceedings of the IEEE/CVF Conference on Computer Vision and Pattern Recognition (2021)

[7] H. S. Park, C. M. Hyun, and J. K. Seo, *Nonlinear ill-posed problem in low-dose dental cone-beam computed tomography*, arXiv preprint arXiv:2303.01678 (2023)

Diffractive tensor field tomography as an inverse problem for a transport equation

THOMAS SCHUSTER

(joint work with Lukas Vierus)

Diffractive tensor field tomography (DTT) means the reconstruction of tensor fields from integral data along geodesic curves in a refracting (inhomogeneous) medium, i.e., with variable refractive index $n(x)$. Since the data are scalar this inverse problem is intrinsically underdetermined and ill-posed. The mathematical model follows Fermat's principle and demands for tools from Riemannian geometry. The refractive medium is characterized by the pair (M, g) where $M \subset \mathbb{R}^d$, $d = 2, 3$, is a compact Riemannian manifold with strictly convex boundary ∂M and the metric g is given as $g_{ij} = n^2(x)\delta_{ij}$, where $n : M \to \mathbb{R}^+$ represents the refractive index. Let ΩM be the pairs $(x, \xi) \in TM$ with unit tangent vectors $|\xi|_{g(x)} = 1$. We define the *inflow and outflow boundaries* by

$$\partial_\pm \Omega M = \{(x, \xi) \in \Omega M : x \in \partial M; \pm\langle \xi, \nu(x)\rangle \geq 0\}.$$

Let $(x, \xi) \in \Omega M$ and $\gamma = \gamma_{x,\xi} : [\tau_-(x, \xi), \tau_+(x, \xi)] \to M$ be a geodesic curve with initial conditions $\gamma_{x,\xi}(0) = x$, $\dot{\gamma}_{x,\xi}(0) = \xi$. If in addition M has the property that for any $x \in M$ and and non-zero vector $\xi \in T_x M$, the geodesic curve $\gamma_{x,\xi}(t)$ cannot be extended further than to a finite interval $[\tau_-(x, \xi), \tau_+(x, \xi)]$, then (M, g) is called a *compact dissipative Riemannian manifold* (CDRM). This means that geodesics must have a finite length. We furthermore postulate that all geodesics enter and leave the boundary at well-defined points. Then, the interval limits can be written as

$$\tau_-(x,\xi) = \max\{\tau \in (-\infty,0] : \gamma_{x,\xi}(t) \cap \partial M \neq \emptyset\}$$
$$\tau_+(x,\xi) = \min\{\tau \in [0,\infty) : \gamma_{x,\xi}(t) \cap \partial M \neq \emptyset\}.$$

Given an attenuation $\alpha \in L^\infty(\Omega M)$ with $\alpha(x,\xi) \geq \alpha_0 > 0$ a.e. in ΩM we define the *attenuated ray transform* $\mathcal{I}_\alpha : L^2(S^m\tau_M') \to L^2(\partial_+\Omega M)$ of a m-tensor field $f = (f_{i_1\cdots i_m})$ by

$$(\mathcal{I}_\alpha f)(x,\xi) = \int_{\tau_-(x,\xi)}^0 \langle f(\gamma_{x,\xi}(\tau)), \dot{\gamma}_{x,\xi}^m(\tau)\rangle \exp\Big(-\int_\tau^0 \alpha(\gamma_{x,\xi}(\sigma),\dot{\gamma}_{x,\xi}(\sigma))\mathrm{d}\sigma\Big)\mathrm{d}\tau.$$

The *attenuated dynamic ray transform*

$$\mathcal{I}_\alpha^d : L^2(0,T;L^2(S^m\tau_M')) \to L^2(0,T;L^2(\partial_+\Omega M))$$

of a m-tensor field $f = (f_{i_1\cdots i_m})$ is defined by

$$(\mathcal{I}_\alpha^d f)(t,x,\xi) = \int_{\tau_-(x,\xi)}^0 \langle f(t+\tau,\gamma_{x,\xi}(\tau)), \dot{\gamma}_{x,\xi}^m(\tau)\rangle \exp\Big(-\int_\tau^0 \alpha(\gamma_{x,\xi}(\sigma),\dot{\gamma}_{x,\xi}(\sigma))\mathrm{d}\sigma\Big)\mathrm{d}\tau.$$

We extend the function $u = \mathcal{I}_\alpha f$ to T^0M, where $T^0M = \big\{(x,\xi) \in TM : \xi \neq 0\big\}$, by

$$u(x,\xi) = \int_{\tau_-(x,\xi)}^0 \langle f(\gamma_{x,\xi}(\tau)), \dot{\gamma}_{x,\xi}^m(\tau)\rangle \exp\Big(-\int_\tau^0 \alpha(\gamma_{x,\xi}(\sigma),\dot{\gamma}_{x,\xi}(\sigma))\mathrm{d}\sigma\Big)\mathrm{d}\tau.$$

This way $u = 0$ in $\partial_-\Omega M$ and $u = \mathcal{I}_\alpha f$in $\partial_+\Omega M$. In the same way we can extend $\mathcal{I}_\alpha^d f$ to $[0,T]\times T^0M$. If $f \in \mathcal{C}(S^m\tau_M')$, then u satisfies the boundary value problem

$$\big(\mathcal{H} + \alpha(x,\xi)\big)u(x,\xi) = \langle f(x), \xi^m\rangle, \text{ on } \Omega M,$$

$$\begin{aligned} u(x,\xi) &= (\mathcal{I}_\alpha f)(x,\xi) =: \phi(x,\xi), & (x,\xi) &\in \partial_+\Omega M,\\ u(x,\xi) &= 0, & (x,\xi) &\in \partial_-\Omega M, \end{aligned}$$

where $\mathcal{H}$ is the *geodesic vector field* $\mathcal{H}u = \xi^i\frac{\partial u}{\partial x^i} - \Gamma^i_{jk}(x)\xi^j\xi^k\frac{\partial u}{\partial \xi^i}$. If f is continuous in time, then u satisfies a corresponding initial boundary value problem. We consider the forward operator $F : \mathcal{D}(F) \subseteq L^2(S^m\tau_M') \to L^2(\partial_+\Omega M)$ with $F = \gamma_+ \circ \mathcal{T}$, where $\mathcal{T}(f) := u$ is the parameter-to-solution map and $\gamma_+ : H^1(\Omega M) \to L^2(\partial_+\Omega M)$ denotes the trace operator on $\partial_+\Omega M$. Unique (classical) solutions exist under smoothness assumptions to n and f (envelopes, method of characteristics , see, e.g., [2]). We study weak solutions. Let the bilinear form $a : H^1(\Omega M) \times H^1(\Omega M) \to \mathbb{R}$ be given as

$$a(u,v) := \int_{\Omega M} \big(-\Gamma^i_{jk}(x)\xi^j\xi^k\frac{\partial u}{\partial \xi^i}v + \langle \nabla_x u, \xi\rangle v + \alpha uv\big)\,\mathrm{d}\Sigma$$

and the linear functional $b : H^1(\Omega M) \to \mathbb{R}$ as

$$b(v) := \int_{\Omega M} \langle f, \xi^m\rangle v\,\mathrm{d}\Sigma.$$

The weak formulation then reads as

$$a(u,v) = b(v) - a(\hat{\phi}, v), \qquad v \in H^1_0(\Omega M)$$

where $\hat{\phi} \in H^1(\Omega M)$ is such that $\gamma_+ \hat{\phi} = \phi$. Set $u_\phi := u + \hat{\phi}$. Unfortunately the bilinear form a is not H^1-coercive. To this end we define (approximate), weak viscosity solutions u_ε by

$$-\varepsilon \Delta u_\varepsilon + \mathcal{H} u_\varepsilon + \alpha u_\varepsilon = \langle f, \xi^m \rangle$$

for small $\varepsilon > 0$. The weak formulation then reads as

$$a_\varepsilon(u_\varepsilon, v) = b^\varepsilon_\phi(v), \qquad v \in H^1_0(\Omega M),$$

where $a_\varepsilon : H^1(\Omega M) \times H^1(\Omega M) \to \mathbb{R}$ is given as

$$a_\varepsilon(u,v) := \int_{\Omega M} \frac{\varepsilon}{n^2(x)} \langle \nabla u, \nabla v \rangle \, \mathrm{d}\Sigma + a(u,v)$$

and $b^\varepsilon_\phi := b - a_\varepsilon(\hat{\phi}, \cdot)$. Again we set $u_{\phi,\varepsilon} := u_\varepsilon + \hat{\phi}$. Let $\varepsilon > 0$, $\alpha \in L^\infty(\Omega M)$ with $\alpha(x,\xi) \geq \alpha_0 > 0$ a.e. in ΩM, $\phi \in L^2(\partial_+ \Omega M)$, $n \in C^1(M)$ and $f \in L^2(S^m \tau'_M)$. If

$$\sup_{x \in M} \frac{|\nabla n(x)|}{n(x)} < \alpha_0,$$

then the variational problem

$$a_\varepsilon(u_\varepsilon, v) = b^\varepsilon_\phi(v) \quad \forall v \in H^1_0(\Omega M)$$

has a unique solution in $H^1_0(\Omega M)$. That means that there is a unique, viscous weak solution if n varies only slowly. For $\alpha_0 \to 0$ we obtain the uniqueness result for $n = 1$ (cf. [1]). An analogue result can be proven for viscous weak solutions in the dynamic setting, see [3]. It is an (by now) open question whether $\lim_{\varepsilon \to 0} u_\varepsilon$ exists (and in which topology) and, if the answer is positive, whether the limit solves the original transport equations.

The inverse problem of DTT using viscosity solutions can now be re-formulated as $F_\varepsilon f = \phi$ for given $\phi \in H^{1/2}(\partial_+ \Omega M)$, where the forward operator $F_\varepsilon : L^2(S^m \tau'_M) \to L^2(\partial_+ \Omega M)$ is given by $F_\varepsilon = \gamma_+ \circ \mathcal{T}_\varepsilon$ and $\mathcal{T}_\varepsilon : L^2(S^m \tau'_M) \to H^1_{0,-}(\Omega M)$ is the parameter-to-solution map mapping f to the unique (weak) viscosity solution $u_{\phi,\varepsilon}$ of the transport equation.

For general $n(x)$ it is difficult to obtain analytic expressions for the adjoints (backprojections) $\mathcal{I}^*_\alpha$, $(\mathcal{I}^d_\alpha)^*$ which are necessary for many inversion formulas and numerical solution methods (such as Filtered Backprojection, Landweber's method, Tikhonov regularization). But we can characterize them using the adjoint PDEs. For $\phi \in L^2(\partial_+ \Omega M)$ we have that

$$(\mathcal{I}^*_\alpha \phi)(x) = \int_{\Omega_x M} w(x,\xi) \xi^m \, \mathrm{d}\sigma(\xi)$$

where $w \in H^1(\Omega M)$ is the weak solution of the boundary value problem

$$-\langle \nabla w, \xi \rangle + \Gamma^k_{ij} \xi_i \xi_j \frac{\partial w}{\partial \xi_k} + (\alpha + \Xi_n(x,\xi))\, w = 0, \quad (x,\xi) \in \Omega M,$$

with boundary conditions

$$w(x,\xi) = \frac{\phi(x,\xi)}{\langle \nu_x, \xi\rangle}\,,\ (x,\xi) \in \partial_+\Omega M$$

$$w(x,\xi) = k_\phi(x,\xi)\exp\Big(- \int_0^{\tau_+(x,\xi)} \big(\alpha + \Xi_n\big)(\gamma_{x,\xi}(\tilde{\tau}), \dot{\gamma}_{x,\xi}(\tilde{\tau}))\mathrm{d}\tilde{\tau}\Big)\,,\ (x,\xi) \in \partial_-\Omega M,$$

where

$$k_\phi(x,\xi) = \frac{\phi(\gamma_{x,\xi}(\tau_+(x,\xi), \dot{\gamma}_{x,\xi}(\tau_+(x,\xi))}{\langle \nu_{\gamma_{x,\xi}(\tau_+(x,\xi))}, \dot{\gamma}_{x,\xi}(\tau_+(x,\xi)\rangle}\,,$$

and

$$\Xi_n(x,\xi) = \begin{cases} \frac{1}{2}n^{-1}(x)\langle \nabla n(x), \xi\rangle, & d=2 \\ n^{-1}(x)\langle \nabla n(x), \xi\rangle, & d=3 \end{cases}\,.$$

A similar representation exists for $(\mathcal{I}^d_\alpha)^*$, see [3]. Numerical results using the damped Landweber method with Nesterov acceleration reconstruction scheme show that indeed even a slightly varying $n(x)$ can not be neglected.

References

[1] E.Y. Derevtsov, Y.S. Volkov, and T. Schuster, *Generalized attenuated ray transforms and their integral angular moments*, Applied Mathematics and Computation, **409** (2021).

[2] L.C. Evans, *Partial Differential Equations*, 2nd ed., AMS, Providence (2010).

[3] L. Vierus and T. Schuster, *Well-defined forward operators in dynamic diffractive tensor tomography using viscosity solutions of transport equations*, Electronic Transactions on Numerical Analysis (ETNA), **57** (2022), 80–100.

Semiclassical methods in tomography

Plamen Stefanov

We review the use of semiclassical analysis in tomography. Microlocal analysis has been recognized as an important tool to describe which singularities are visible, and which are not and to help reconstruct them; in particular to help with detection of edges. Semiclassical analysis is microlocal in nature as well but instead of looking at the asymptotic expansion as the dual variable ξ approaches infinity, it is interested, roughly speaking, in what happens on the way there. We consider $h > 0$ to be a small parameter; which in the standard use of this calculus is the Planck constant. The semiclassical wavefront set $\mathrm{WF}_h(f)$ of f which may depend on h, consists of those (x,ξ) so that the windowed *semiclassical* Fourier transform $\widehat{\psi f}(\xi/h)$ does not decay rapidly as $h \to 0$. Intuitively, $\mathrm{WF}_h(f)$ consists of points and (co)directions corresponding to high oscillations at a rate ξ/h there.

We show that (classical) pseudo-differential and Fourier Integral operators (FIOs) resolve $\mathrm{WF}_h(f)$ away from $\xi = 0$. Our motivating example is the weighted Radon transform but the theory applies to much more general operators. We present several applications on the calculus.

Discretization/sampling. We describe briefly the results in [4]. In many numerical calculations, we would represent a given function $f(x)$ on a finite grid, i.e., we take $\{f(x_j)\}$ to be an approximate representation of f. If h is proportional to the step size sh, we think of it as an asymptotic process as $h \to 0$. Then we show that there is a semiclassical version of the sampling theory assuring a reconstruction of f from the samples via a Whittaker–Shannon type of interpolation formula up to an $O(h^\infty)$ error if the step satisfies the Nyquist condition $s < \pi/B$. Here, $B > 0$ is the semiclassical band-limit, finite by assumption, defined as the least B so that $\hat{f}(\xi/h)$ is essentially supported in $[-B, B]^n$.

If A is an FIO, we show that the **sampling requirements for** Af are related to those of f by the canonical relation of A. In particular, this tells us how dense we need to sample Af having a priori information about the "smallest detail" f has. If A is elliptic, associated to a canonical relation which is locally a diffeomorphism, we can apply the same arguments to the parametrix A^{-1}. We apply this to the Radon transform, in particular, to recover earlier applied math results by other authors. That also tells us how much **resolution** on f we can possibly have, given the resolution (the sampling rate) of the data Af. **Aliasing** is well understood in classical sampling theory, and it turns out to be a semiclassical FIO in our setting. When applying an FIO A as above, or its parametrix A^{-1}, aliasing of the end-result is also a semiclassical FIO with a canonical relation that can be computed by Egorov's theorem. In the case of Radon transform R we compute explicitly the aliasing artifacts of the reconstructed f given an undersampled Rf. It turns out that semiclassical singularities can jump from one place to another with or without changing the frequency as well. This makes aliasing a non-local phenomenon! We illustrated that with many numerical simulations. Finally, we study the effect of small local averaging, or regularization, of the data Af on the reconstructed f. We model that by a Friedrichs mollifier with $\phi_h(x) = h^{-n}\phi(x/h)$, where $\hat{\phi} \in C_0^\infty$. That convolution is actually a semiclassical pseudo-differential operator, and the reconstructed f from regularized data is asymptotically given by $Q(x, hD)f$, where Q is again such an operator with a principal symbol $\phi(\xi)$ pulled back by the canonical relation of A. It can be described as an x-dependent, anisotropic, in general, regularization of f.

Sampling theory in principle requires Whittaker–Shannon interpolation (or a modification of it) to get an accurate interpolation. If we want to do this numerically, to convert samples to a "continuous function," we need to pass to a much finer grid. It turns out [3] that when using the filtered backprojection formula for the Radon transform $Rf(p, \omega)$ with discrete values ω_j of the angles, and all p, there is no need of interpolation. This is due to the Poisson summation formula and even though there is no interpolation, the reconstruction can be explained by the asymptotic sampling theory.

We applied this theory to the **geodesic X-ray transform** in [2]. We showed that the behavior of the Jacobi fields, and in particular the curvature, play a fundamental role in the way this problem should be discretized.

Semiclassical analysis is useful in analyzing propagation of **noise** under inversion, as done in [5]. If we add white noise to the data, or even other type of noise, one can describe the spectral density of the noise by the semiclassical "defect measure." For white noise, it is constant over the Nyquist range of the (discrete) noise. Apply A (or A^{-1}) however maps that noise to noise with a defect measure that can be computed from the one applied to the data, knowing the canonical relation of A. The result is noise changing from point to point, also possibly direction dependent. The calculus allows us to compute the characteristics of the noise added to f, like the standard deviation, locally or even microlocally. One could consider non-additive noise as well.

In [1], those methods were applied to Thermoacoustic Tomography.

References

[1] C. Mathison. Sampling in thermoacoustic tomography. *J. Inverse Ill-Posed Probl.*, 28(6):881–897, 2020.

[2] F. Monard and P. Stefanov. Sampling the X-ray transform on simple surfaces. *arXiv:2110.05761*, 2022.

[3] P. Stefanov. The Radon transform with finitely many angles. *arXiv:2208.05936.*

[4] P. Stefanov. Semiclassical sampling and discretization of certain linear inverse problems. *SIAM J. Math. Anal.*, 52(6):5554–5597, 2020.

[5] P. Stefanov and S. Tindel. Sampling linear inverse problems with noise. *Asymptot. Anal.*, 132(3-4):331–382, 2023.

Photoacoustic and Ultrasonic Tomography for Breast Imaging

Felix Lucka

(joint work with the PAMMOTH team)

New high-resolution, three-dimensional imaging techniques are being developed that probe the breast without delivering harmful radiation and without requiring painful compression. In particular, photoacoustic tomography (PAT) and ultrasound tomography (UST) promise to give access to high-quality images of tissue parameters with important value for the detection and diagnosis of breast cancer. However, the involved inverse problems are very challenging from an experimental, mathematical and computational perspective. In this talk, we want to give an overview of these challenges and illustrate them with data from an ongoing clinical feasibility study that uses the PAMMOTH scanner for combined PAT and UST.

Mathematically, the forward problem of PAT can be modeled in four steps: Firstly, the breast is illuminated by a short pulse of near-infrared laser light. The transport, scattering and absorption of photons in the breast tissue can be modeled by the radiative transfer equation (RTE):

$$(v \cdot \nabla + \mu_a(x) + \mu_s(x))\, \Phi(x,v) = q(x,v) + \mu_s(x) \int \Theta(v,v')\Phi(x,v')\, dv' \tag{1}$$

Here, $\Phi(x,v)$ denotes the photon transport density in location x and direction v, μ_a and μ_s denote absorption and scattering coefficients, q models the laser source and Θ is the scattering kernel. The photoacoustic effect describes how the rapid

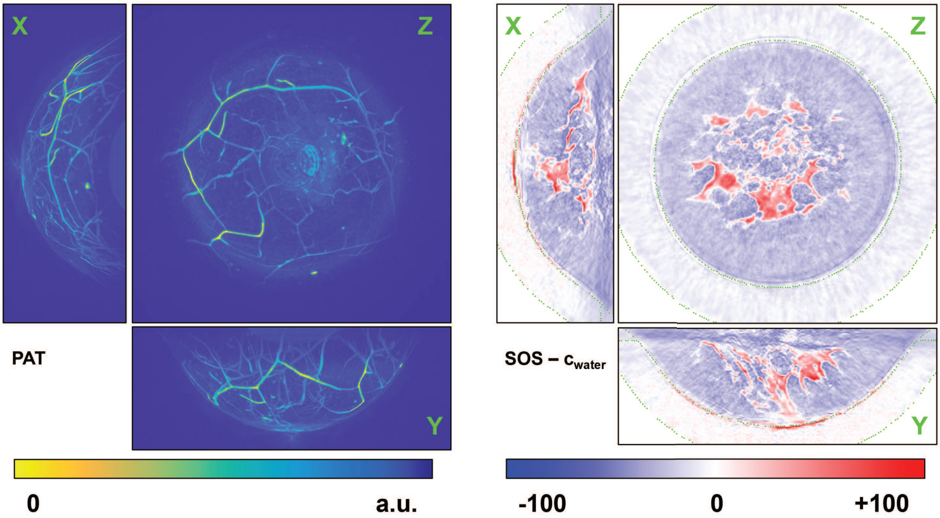

FIGURE 1. Examples of preliminary *in-vivo* results. Left: 3D reconstruction of p_0 with a spatial resolution of 0.4mm, visualized as maximum intensity projections. Right: 3D reconstruction of $c - c_{water}$ using TD-FWI with a spatial resolution of 0.6mm, visualized as slice views.

absorption of the optical energy leads to a thermoelastic expansion of the tissue, which induces a pressure increase:

$$p_0(x) = \Gamma(x)\mu_a(x) \int \Phi(x, v')\, dv' \quad , \tag{2}$$

where Γ describes the efficiency of this conversion of optical into acoustic energy. The initial pressure p_0 travels through the tissue as ultrasonic waves

$$\left(c(x)^{-2}\partial_t^2 - \Delta\right) p(x,t) = 0, \qquad p(x,0) = p_0(x), \qquad \partial_t p(x,0) = 0 \tag{3}$$

which can be measured once they reach the detection surface of the scanner:

$$f = Mp \tag{4}$$

PAT inversion consists of two coupled inverse problems: First, ones tries to recover p_0 from f, which corresponds to solving an acoustic initial value problem (3) with boundary data (4). More details on this linear inverse problem can be found in [1]. We formulate its solution as a variational regularization problem

$$\min_{p_0 \in \mathcal{C}} \|MAp_0 - f\|_W^2 + \mathcal{R}(p_0) \quad , \tag{5}$$

where the linear operator A maps p_0 to the solution of (3), and use first-order optimization schemes with early stopping (*accelerated proximal gradient descent*, see [2] for more details). We illustrate how using accurate models of the ultrasound transducers improve the reconstructed images, validate the results using experimental phantoms and show *in-vivo* results of volunteers and patients, cf. Fig 1. In a second step, we try to recover μ_a from p_0, which corresponds to an optical parameter identification problem (1) with internal data (2). More details on this non-linear inverse problem can be found in [3].

In UST, we emit ultrasonic waves from $i = 1, \ldots, N_s$ sources supported on the measurement surface and capture the transmitted and scattered waves as

$$f_i = M_i p_i, \qquad \left(c(x)^{-2}\partial_t^2 - \Delta\right) p_i(x,t) = s_i(x,t), \qquad p(x,0) = \partial_t p(x,0) = 0 \tag{6}$$

Recovering the *speed-of-sound* c from $\{f_i\}_{i=1}^{N_s}$ is an acoustic parameter identification problem with boundary data. There are different approaches to solve this non-linear inverse problem, typically accounting for different aspects of the complex wave physics underlying the data generation. For instance, *travel time tomography* is based on a geometrical optics approximation and relies on travel time differences of the transmitted waves as the main source of information. It leads to a robust and computationally efficient inversion scheme, see [4] for more details. However, the approximation limits the spatial resolution obtainable. *Time-domain full waveform inversion* (*TD-FWI*) relies on numerical wave solvers and formulates the solution to (6) as a variational regularization problem

$$\min_{c\in\mathcal{C}} \sum_{i}^{N_s} \|M_i \underbrace{\left(c(x)^{-2}\partial_t^2 - \Delta\right)^{-1} s_i(x,t)}_{p_i(c)} - f_i\|_2^2 + \mathcal{J}(c) \quad . \tag{7}$$

To solve this large-scale, non-convex optimization problem via first-order optimization schemes, the adjoint state method can be used to compute

$$\nabla_c \|M_i p_i(c) - f_i\|_2^2 = 2\int_0^T c(x)^{-3}\partial_t^2 p_i(x,t) q_i^*(x,t)\, dt \quad , \tag{8}$$

where $q_i^*(x,t)$ solves $\left(c(x)^{-2}\partial_t^2 - \Delta\right) q^*(x,t) = s^*(x,t)$ and $s^*(x,t)$ is time-reversed data discrepancy $M_i p_i - f_i$. For high resolution 3D UST ($\sim$ 0.5mm isotropic resolution), using TD-FWI holds three key challenges: Firstly, the computation of the gradient for a single source i has a restrictively large memory footprint. Secondly, the number of sources N_s used in the PAMMOTH patient protocol is 18.000. Lastly, the structure of (7) may result in slow progression of the solver and convergence to a local minimum. We describe a comprehensive computational strategy to overcome these challenges in [5], discuss its translation to experimental data and illustrate preliminary results for experimental phantoms and breast cancer patients, *cf.* Fig 1.

REFERENCES

[1] P. Kuchment, L. Kunyansky, *Mathematics of Photoacoustic and Thermoacoustic Tomography*, Handbook of Mathematical Methods in Imaging (O. Scherzer) **32** (2011), 817–865.

[2] S.R. Arridge, M.M. Betcke, B.T. Cox, F. Lucka, B.E. Treeby, *On the adjoint operator in photoacoustic tomography*, Inverse Problems **32(11)** (2016), 115012.

[3] B. Cox, J.G. Laufer, S.R. Arridge, P. Beard *Quantitative spectroscopic photoacoustic imaging: a review*, Journal of Biomedical Optics **17(6)** (2012), 061202-1–061202-22.

[4] A. Javaherian, F. Lucka, B.T. Cox, *Refraction-corrected ray-based inversion for three-dimensional ultrasound tomography of the breast*, Inverse Problems **36(12)** (2020), 125010.

[5] F. Lucka, M. Pérez-Liva, B.E. Treeby, B.T. Cox, *High resolution 3D ultrasonic breast imaging by time-domain full waveform inversion*, Inverse Problems **38(2)** (2021), 025008.

Is BMD by DXA or CT reliable?

Ming Jiang

Bone mineral density (BMD) is the amount of bone mineral in bone tissue. BMD measurement is used in clinic as an indirect indicator of osteoporosis and fracture risk [1]. "*Dual-energy x-ray absorptiometry (DXA) is the most widely used and most thoroughly studied BMD technology*" [2], in spite of its controversial reliability [3].

DXA measures two projections at two energies, respectively, but only for one single direction. When soft tissue absorption is subtracted out, the BMD is estimated from the resulting absorption, which is assumed to that of bone [2]. It is natural that the higher the BMD, the bigger the projection in DXA measurement, because the Radon transform is monotone, i.e., $R(f) \geq R(g)$ if $f \geq g$, where both inequality holds in the sense of pointwise order [4, §1.37]. Although DXA only measures one projection at one single direction, we can mathematically pretend that all the projection at all directions are available, without loss of generality, to simplify the presentation.

A mathematical problem appears naturally with DXA: does bigger projections conclude higher BMDs? Mathematically, this is equivalent to the following problem: is the inverse R^{-1} of the Radon transform monotone, i.e., does it hold that $R^{-1}(p) \geq R^{-1}(q)$ if $p \geq q$, where both inequality is defined in the sense of pointwise order. In this preliminary study, we assume that the Radon transform is defined on $L^2(\Omega)$ where Ω is the 2D disk of $\mathbb{R}^2$. The inverse of the Radon transform is well defined on a subspace of the weighted Hilbert space $L^2([-1,1] \times S^1, w^{-1})$, where $w(s) = \sqrt{1-s^2}$ [7].

It is then found that the inverse Radon transform is not monotone by an order-theoretic approach. We need some notations from order theory to proceed. Let X be a poset. For any two elements x and $y \in X$, $x \wedge y$ is the infimum of them, if it exists. By [4, Lemma 2.27, p. 47], if both $f : X \to Y$ and $f^{-1} : Y \to X$ are monotone, then for any x and $y \in X$, if $x \wedge y$ exists, then $f(x) \wedge f(y)$ exists, and

$$f(x \wedge y) = f(x) \wedge f(y). \tag{1}$$

Then we can show that (1) does not hold for the Radon transform. Let Ω_1 and Ω_2 be two disjoint sub-domain of Ω such that $\texttt{dist}(\Omega_1, \Omega_2) > 0$. Let $u \in C_0^\infty(\Omega_1)$ and $v \in C_0^\infty(\Omega_2)$ such that $0 \leq u \leq 1$ and $0 \leq v \leq 1$. u and v can also be chosen to be the the characteristic functions of Ω_1 and Ω_2, respectively. Because $\Omega_1 \cap \Omega_2 = \emptyset$, we have $u \wedge v = \mathbf{0}$, where $\mathbf{0}$ is the function identically equal to 0 and the same in the following even for different domains. Hence, the left side of (1) for the Radon transform is

$$R(u \wedge v) = R(\mathbf{0}) = \mathbf{0}. \tag{2}$$

For the Radon transform R of u and v, we have

$$R(u) \geq \mathbf{0},\ R(v) \geq \mathbf{0},\ R(u) \wedge R(v) \geq \mathbf{0} \text{ but } R(u) \wedge R(v) \neq \mathbf{0}. \tag{3}$$

Note that in the case of DXA with only one projection in one single direction, we can rotate Ω_1 and Ω_2 so that x-ray beams pass through both of them and the above inequalities hold. Hence, (1) does not holds for the Radon transform with the two functions u and v. If follows that the inverse of the Radon transform cannot be monotone.

The above order-theoretic can be applied to other transforms such as the ray transform and x-ray transform and leads to the same conclusion that the inverse is not monotone, and might be applied to other inverse problems, when the inverse exists. For incomplete data, the inverse does not exist and depends how the inversion is performed. A related study is the work initiated by L. Collatz in [8] and well summarized in [9].

The conclusion that the Radon transform fails to be monotone implies that bigger projections do not conclude higher BMDs, or comparable projections do not imply comparable reconstructed images. Hence, there are *monotone-ghosts* such that they are non-positive but with non-negative projections because the linearity of the Radon transform, i.e.,

$$g \ngeq 0, \text{ but } R(g) \geq 0. \tag{4}$$

The term *monotone-ghost* is coined to imitate the term *ghost* for the null space in the case of finite number of projections [5–7]. The monotone-ghosts destroy the monotone inversion while Louis' ghosts destroying the uniqueness.

Given the imperfection of DXA, x-ray CT techniques, especially, quantitative CT (QCT) and high-resolution peripheral quantitative computed tomography (HR-pQCT), have been developed for diagnosing osteoporosis [10]. In spite of efforts of decades, QCT/HR-pQCT is not approved for clinical use at present [10,11]. It is found that that there are many potential sources of error in BMD estimates from QCT [12]. The existence of monotone-ghosts could be a reason for this issue because its potential effect on image contrast resolution.

The order-theoretic approach only qualitatively demonstrates that the existence of monotone-ghosts. With the SVD of the Radon transform R from $L^2(\Omega)$ to $L^2([-1,1] \times S^1, w^{-1})$, we can construct explicitly some monotone-ghosts. Use the same notations for the SVD as in [7, §2.1]. Let $\{v_{m,\lambda}, u_{m,\lambda}; \sigma_{m,\lambda}\}$, for $0 \leq \lambda \leq m$ with $m + \lambda$ even, be the SVD of the Radon transform, i.e.,

$$R\left(v_{m,\lambda}\right) = \sigma_m u_{m,\lambda}, \tag{5}$$

where the singular value $\sigma_{m,\lambda} = \sigma_m = 2\sqrt{\frac{\pi}{m+1}}$.

Because low trabecular bone density is directly related to both compressive strength and fracture risk [13], it is necessary to image the fine structure of spongy bone together with sufficient spatial and contrast resolutions for trabecular bone density estimate. Higher order eigenfunctions (HEF) $v_{m,\lambda}$ are significant for representing the spongy trabecular structure. However, their contributions can be diminished at measurement because the decay of singular values $\sigma_{m,\lambda}$ and if the accuracy and signal-to-noise ratio of the imaging detector is not high enough. Therefore, such HEFs are unobservable by reconstruction. This can be one potential reason for the error in BMD estimates from QCT because of missing the significant components after imager reconstruction.

Any technique has its limitation. The reporter is not to conclude naively that either DXA or QCT is not useful, but only to show mathematically why they do not work reliably as expected. This presentation is based on a on-going work conducted through discussions with A. K. Louis, P. Maaß, E. T. Quinto. The reporter takes the full responsibility for any mistake and error in the presentation and in this abstract.

References

[1] Wikipedia contributors (2023b). Bone density — Wikipedia, the free encyclopedia. https://en.wikipedia.org/wiki/Bone_density.

[2] Wikipedia contributors (2023a). Dual-energy x-ray absorptiometry — Wikipedia, the free encyclopedia. https://en.wikipedia.org/wiki/Dual-energy_X-ray_absorptiometry

[3] Bolotin, H. H. (2007). DXA in vivo BMD methodology: an erroneous and misleading research and clinical gauge of bone mineral status, bone fragility, and bone remodelling. *Bone*, 41(1):138–154.

[4] Davey, B. A. and Priestley, H. A. (2002). *Introduction to lattices and order*. Cambridge University Press, New York, second edition.

[5] Louis, A. K. (1981). Ghosts in tomography—the null space of the Radon transform. *Mathematical Methods in the Applied Sciences*, 3(1):1–10.

[6] Louis, A. K. (1984). Nonuniqueness in inverse Radon problems: the frequency distribution of the ghosts. *Mathematische Zeitschrift*, 185(3):429–440.

[7] Louis, A. K. (2019). Uncertainty, ghosts, and resolution in Radon problems. In *The Radon transform—the first 100 years and beyond*, volume 22 of *Radon Ser. Comput. Appl. Math.*, pages 169–188. Walter de Gruyter, Berlin.

[8] Collatz, L. (1952). Aufgaben monotoner Art. *Archiv der Mathematik*, 3:366–376.

[9] Berman, A. and Plemmons, R. J. (1994). *Nonnegative matrices in the mathematical sciences*, volume 9 of *Classics in Applied Mathematics*. Society for Industrial and Applied Mathematics (SIAM), Philadelphia, PA.

[10] Pennington, Z., Ehresman, J., Lubelski, D., Cottrill, E., Schilling, A., Ahmed, A. K., Feghali, J., Witham, T. F., and Sciubba, D. M. (2021). Assessing underlying bone quality in spine surgery patients: a narrative review of dual-energy X-ray absorptiometry (DXA) and alternatives. *Spine Journal*, 21(2):321–331.

[11] Link, T. M. and Kazakia, G. (2020). Update on imaging-based measurement of bone mineral density and quality. *Current Rheumatology Reports*, 22(5).

[12] Brunnquell, C. L., Winsor, C., Aaltonen, H. L., and Telfer, S. (2021). Sources of error in bone mineral density estimates from quantitative CT. *European Journal of Radiology*, 144.

[13] Carter, D. R. and Hayes, W. C. (1976). Bone compressive strength: the influence of density and strain rate. *Science*, 194(4270):1174–1176.

Fast Inversion Formulae for Some Ray Transforms in Vector and Tensor Tomography

Alfred K. Louis

Ray transforms, besides X-ray transforms, have been studied for a long time, especially in connection with vector and tensor tomography. Reconstruction formulae are already studied in the seminal book of Sharafutdinov [8] and the many papers connected to the field, see e.g. [7]. Also different scanning geometries are studied like those known from X-ray tomography, as fan beam or cone beam transforms. Formulae for the three-dimensional problem are studied for so-called incomplete data problems, where incomplete here means that not all possible data are available, but sufficiently many for unique and stable reconstruction, as in X-ray applications. Sharafutdinov, [8], bases his inversion formula on applying first the backprojection and then manipulating the outcome. From a mathematical point of view this is exact. Here we aim for an inversion formula where first the data is filtered and then a suitable backprojection is applied.

In this report we restrict our consideration to the longitudinal ray transform defined in 2D for a vector field f as

$$(\mathbf{P_1}f)(\theta,s)=\int_{\mathbb{R}}\theta^\top f(s\theta^\perp+t\theta)dt=\theta^\top\mathbf{P}f(\theta,s)$$

where $\mathbf{P}f$ is the x-ray transform of the components of f. Similar results hold for the transversal ray transform. We restrict the considerations to compactly supported vector fields with 0 boundary conditions, the Helmholtz-Hodge decomposition then gives

$$f=\nabla\psi+{}^sf$$

where ${}^sf$ is the solenoidal part. The potential part $\nabla\psi$ is in the null space of the longitudinal transform, hence only the solenoidal part can be recovered from the longitudinal transform. Using the representation

$${}^sf=\nabla^\perp\varphi$$

we make use of formulas presented by Prince [6] and Derevtsov [1]

$$\mathbf{P_1}{}^sf=\mathbf{P_1}\nabla^\perp\varphi=\frac{\partial}{\partial s}\mathbf{P}\varphi$$

The right-hand side is part of the inversion formula of the x-ray transform resulting in

$$\varphi=\mathbf{P}^{-1}\mathbf{P}\varphi=\frac{1}{4\pi}\mathbf{P}^*\mathbf{H}\frac{\partial}{\partial s}\mathbf{P}\varphi$$

where $\mathbf{H}$ denotes the Hilbert transform. Consequently the solenoidal part can be determined by

$${}^sf=\frac{1}{4\pi}\nabla^\perp\mathbf{P}^*\mathbf{H}\mathbf{P_1}{}^sf$$

Using the L_2 dual operator of $\mathbf{P_1}$

$$(\mathbf{P_1})^*g(x)=\int_{S^1}\theta g(\theta,x^\top\theta^\perp)d\theta$$

and the intertwining property of $\nabla^{\perp}$ and $\mathbf{P}^*$

$$\nabla \mathbf{P}^* = (\mathbf{P_1})^* \frac{\partial}{\partial s}$$

we find the new inversion formula.

Theorem
The following inversion formula for the longitudinal ray transform

$$(\mathbf{P_1})^{-1} = \frac{1}{4\pi}(\mathbf{P_1})^* \mathbf{I}^{-1}$$

where $\mathbf{I}^{-1}$ denotes the Riesz-potential of order -1, see [5].

For more details and inversion formulae for tensor tomography and slice-by-slice tomography in three dimensions, see [4].

For deriving an inversion formula we apply the following strategy:

- represent the functions orthogonal of the null space as the application of a differential operator D^1 to a 'potential'
- derive a relation of type Prince-Derevtsov formula relating the ray transform of the functions perpendicular to the null space as a differential operator D^2 applied to the x-ray transform
- invert the x-ray transform to get the 'potential' and apply the differential operator D^1
- find an intertwining property for the differential operator D^1 applied to the backprojection to give the adjoint operator of the ray transform applied to a differential operator D^3

for suitable differential operators D^1, D^2, D^3.

REFERENCES

[1] E. Y. Derevtsov. *Certain problems of non-scalar tomography.* Siberian Èlektron. Mat. Izv., **7**:C.81–C.111, 2010.

[2] E. Y. Derevtsov and I. E. Svetov. *Tomography of tensor fields in the plain.* Eurasian J. Math. Comput. Appl., **3**:24–68, 2015.

[3] A. K. Louis. *Feature reconstruction in inverse problems.* Inverse Problems, **27**(6):065010, 2011.

[4] A.K.. Louis, *Inversion Formulae for Ray Transforms in Vector and Tensor Tomography Inverse Problems*, Inverse Problems **38** (2022), 065008.

[5] F. Natterer. *The Mathematics of Computerized Tomography.* Teubner and Wiley, Stuttgart, 1986.

[6] J.L. Prince, *Tomographic reconstruction of 3-D vector fields using inner product probes*, IEEE TMI **3** (1994), 216–219.

[7] T. Schuster. *The 3d doppler transform: elementary properties and computation of reconstruction kernels.* Inverse Problems, **16**(3):701–722, 2000.

[8] V. A. Sharafutdinov. *Integral Geometry of Tensor Fields.* VSP, 1994.

On a cylindrical scanning modality in three-dimensional Compton scatter tomography

JAMES W. WEBBER

1. INTRODUCTION

Compton Scatter Tomography (CST) is an imaging technique which uses Compton scattered photons to recover an electron density, which has applications in security screening, medical and cultural heritage imaging [1–5].

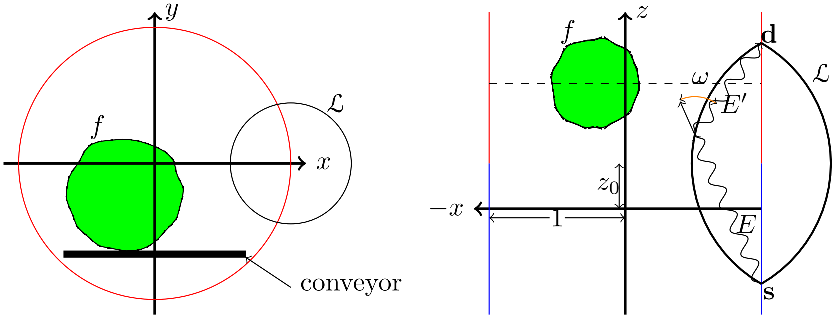

FIGURE 1. (x, y) and (x, z) plane cross sections of the proposed cylindrical scanning geometry. The cylinder has unit radius. TThe sources ($\mathbf{s}$) are located on the bottom half of the cylinder, highlighted in blue, and the detectors ($\mathbf{d}$), highlighted in red, are located on the upper half. $z_0 \in \mathbb{R}$ is the z component of the center of $\mathfrak{L}$.

We introduce a new scanning modality in 3-D CST, whereby monochromatic (e.g., gamma ray) sources and energy-sensitive detectors on a cylindrical surface scan a density passing through the cylinder on a conveyor. See figure 1. The incoming photons, emitted from $\mathbf{s}$ with energy E, Compton scatter from charged particles (usually electrons) with energy E', and are measured by the detector, $\mathbf{d}$; meanwhile, the electron charge density, f (represented by a real-valued function), passes through the cylinder in the z direction on a conveyor belt. The scattered energy, E', is given by the equation

$$E' = \frac{E}{1 + (E/E_0)(1 - \cos\omega)}, \tag{1}$$

where E is the initial energy, ω is the scattering angle and $E_0 \approx 511$keV denotes the electron rest energy. If the source is monochromatic (i.e., E is fixed) and we can measure the scattered energy, E', i.e., the detectors are energy-sensitive, then the scattering angle, ω, of the interaction is fixed and determined by equation (1). This implies that the surface of Compton scatterers is the surface of rotation of a circular arc, which we denote as a lemon, $\mathfrak{L}$. Thus, we model the Compton scattered intensity as integrals of f over lemons. See, e.g., [2] for other work which models the Compton intensity in this way.

2. MAIN RESULTS

We analyze the generalized Radon transform, $\mathcal{R}$, defined by

$$\mathcal{R}f(\mathbf{s},\mathbf{d},E',z_0)=\int_{\mathcal{L}(\mathbf{s},\mathbf{d},E',z_0)} f\mathrm{d}S, \tag{2}$$

where $\mathcal{L}=\mathcal{L}(\mathbf{s},\mathbf{d},E',z_0)$ denotes a lemon surface, parameterized by $(\mathbf{s},\mathbf{d},E',z_0)$, as in figure 1, and $\mathrm{d}S$ denotes the surface measure on $\mathcal{L}$. We consider only the $\mathcal{L}$ with central axis parallel to z. In total, we vary four parameters, namely $\mathbf{s}$ and $\mathbf{d}$ (i.e., the positions of the tips of the lemon), the scattered energy, E', which determines ω, and z_0, which translates $\mathcal{L}$ in direction z. Equivalently, z_0 controls the position of f on the conveyor.

2.1. **Injectivity.** Let $C_\epsilon=\{\sqrt{x^2+y^2}<1-\epsilon\}$, for some small offset $0<\epsilon<1$, and let $L^2_c(C_\epsilon)$ denote the set of square integrable functions with compact support in C_ϵ. Then, we have the following theorem.

Theorem 2.1. *Let $0<\epsilon<1$ be fixed. Then, the lemon Radon transform, $\mathcal{R}$, is injective on domain $L^2_c(C_\epsilon)$.*

Theorem 2.1 shows that any $f\in L^2_c(C_\epsilon)$ can be recovered uniquely from $\mathcal{R}f$. To prove Theorem 2.1, we first take a Fourier decomposition of $\mathcal{R}$ on the cylinder, which reduces $\mathcal{R}$ to a set of one-dimensional Volterra operators of the first kind. After which, we apply the theory of [6] to prove injectivity of $\mathcal{R}$, and derive an inversion formula using Neumann series. The support of f is required to be bounded away from the cylinder surface (i.e., by distance ϵ) to avoid singularities (division by zero) in the Volterra equation kernel.

2.2. **Microlocal analysis.** We state our main microlocal theorem below.

Theorem 2.2. *$\mathcal{R}$, on domain $L^2_c(C_0)$, is an FIO which satisfies the Bolker condition*

Theorem 2.2 shows that there are no added, unwanted edges in a reconstruction from $\mathcal{R}f$ data, for functions $f\in L^2_c(C_0)$. In particular, we prove that any added image edge artifacts are reflections of the true image edge map through planes tangent to the boundary of C_0. Thus, if f is supported within C_0, the added artifacts must lie outside of C_0, and do not interfere with the scanning region. We can also use our theory to predict precisely where artifacts will occur. For example, see figure 2a, where we show the artifacts predicted by our theory in reconstructions of delta functions. A delta function is supported at a single point, and has edges in all directions. The artifacts due to Bolker, in this case, are embedded in the (x,y) plane and appear on cardiod type curves which lie outside of C_0.

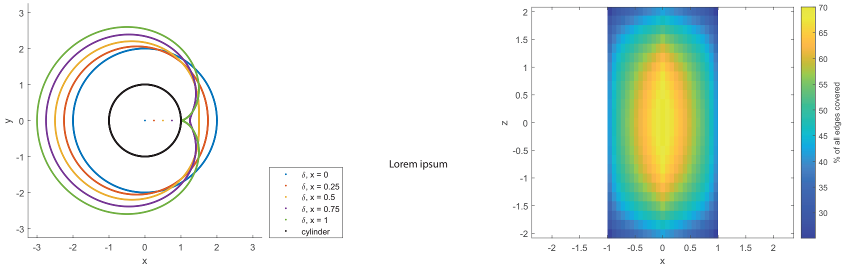

(A) Bolker (B) edge detection

FIGURE 2. Left - Predicted artifacts due to Bolker when reconstructing delta functions ($f = \delta$) from $\mathcal{R}f$. Right - The percentage of edges detectable by $\mathcal{R}$ within C_0. We set the height of C_0 as 4.

2.2.1. *Edge detection.* We investigate the edge detection capabilities of $\mathcal{R}$ within C_0 using microlocal analysis. See figure 2b. For every point $\mathbf{x} \in C_0$, we calculate the proportion of directions $\boldsymbol{\xi} \in S^2$ which are detectable by $\mathcal{R}$. A value closer to 1 on the colorbar means greater edge detection, and conversely for values closer to 0. We see that, as we go closer to the center of C_0, the edge detection ability of $\mathcal{R}$ is greatest, and this tapers off quite significantly near the boundary and top and bottom of C_0. Nowhere in C_0 are 100% of edges detectable, and thus the problem is one of limited-angle tomography, which are often severely ill-posed [8].

REFERENCES

[1] Redler, Gage, Kevin C. Jones, Alistair Templeton, Damian Bernard, Julius Turian, and James CH Chu. "Compton scatter imaging: A promising modality for image guidance in lung stereotactic body radiation therapy." Medical physics 45, no. 3 (2018): 1233-1240.

[2] Rigaud, Gaël. "Compton scattering tomography: feature reconstruction and rotation-free modality." SIAM Journal on Imaging Sciences 10, no. 4 (2017): 2217-2249.

[3] Cebeiro, Javier, Mai K. Nguyen, Marcela Alejandra Morvidone, and Albert Noumowé. "New "improved" Compton scatter tomography modality for investigative imaging of one-sided large objects." Inverse Problems in Science and Engineering 25, no. 11 (2017): 1676–1696.

[4] Guerrero Prado, Patricio, Mai K. Nguyen, Laurent Dumas, and Serge X. Cohen. "Three-dimensional imaging of flat natural and cultural heritage objects by a Compton scattering modality." Journal of Electronic Imaging 26, no. 1 (2017): 011026-011026.

[5] Webber, James, and Eric L. Miller. "Compton scattering tomography in translational geometries." Inverse Problems 36, no. 2 (2020): 025007.

[6] Tricomi, Francesco Giacomo. Integral equations. Vol. 5. Courier corporation, 1985.

[7] Ambartsoumian, Gaik, Jan Boman, Venkateswaran P. Krishnan, and Eric Todd Quinto. "Microlocal analysis of an ultrasound transform with circular source and receiver trajectories." American Mathematical Society, series= Contemporary Mathematics 598 (2013): 45-58.

[8] Krishnan, Venkateswaran P., and Eric Todd Quinto. "Microlocal Analysis in Tomography." Handbook of mathematical methods in imaging 1 (2015): 3.

Ray tracing approximations to the acoustic propagation in weakly nonlinear regime with applications in HIFU

Marta M. Betcke
(joint work with Matt G. Foster, Ben T. Cox)

In High Intensity Focused Ultrasound (HIFU), sound waves are fired from a focused bowl transducer into the body causing local cell necrosis near the focus while leaving the rest of the tissue unharmed. The intensities used indicate a weakly nonlinear regime in which the harmonics of the fundamental frequency are generated causing steepening of the sinusoidal source waveform as it progresses through the medium to become a sawtooth wave. Resolution of the harmonics poses computational difficulties to finite element or finite difference solvers, which require a set number of grid points per wavelength, quickly leading to computationally infeasible grid sizes in particular in three dimensions.

Here we propose to reduce the computational requirement to a solution of a family of 1D equations by extending the linear ray theory [1] into the nonlinear regime. These rays propagate through the medium following an equation for the phase called the Eikonal equation, and can bend depending on both the medium properties and, possibly also the amplitude of the wave. The rays then give the phase of the wave at set points and a 1D equation is solved along each ray to obtain the amplitude of the wave. This can then be interpolated to obtain the waveform in the focus region of the transducer.

The weakly nonlinear ray derivation starts from the standard governing equations, the conservation of mass and inviscid conservation of momentum [2]. These are paired along side an equation of state which relates the pressure to the density

$$p(\rho) = p|_{\rho_0} + c_0^2\rho + \frac{c_0^2}{\rho_0}\frac{B}{2A}\rho^2,$$

where $\frac{B}{A}$ is known as the nonlinearity parameter and $A = \rho_0\left(\frac{\partial p}{\partial \rho}\right)_{s,0}$ and $B = \rho_0^2\left(\frac{\partial^2 p}{\partial \rho^2}\right)_{s,0}$. The two conservation laws and the pressure density relation can be written in a matrix vector form using Einstein notation,

$$\mathcal{A}(\mathbf{x},t,\mathbf{u},\rho)\mathbf{v}_t + \mathcal{B}^\alpha(\mathbf{x},t,\mathbf{u},\rho)\mathbf{v}_{x_\alpha} + \mathcal{C}(\mathbf{x},t,\mathbf{u},\rho)\mathbf{v} = 0,$$

where $\mathbf{v}$ is the vector composed of the density ρ and the wave velocity $\mathbf{u}$, $\mathbf{v} = (\rho, \mathbf{u}^{\mathrm{T}})^{\mathrm{T}}$. The variables in $\mathbf{v}$ are all defined as their acoustic values i.e. as small perturbations of the ambient conditions such as the medium density ρ_0, and velocity $\mathbf{u}_0$. Hence, we expand the vector $\mathbf{v}$ in the limit of a small parameter $\varepsilon \to 0$

$$\text{(WNE)} \qquad \mathbf{v}(\mathbf{x},t;\varepsilon) = \varepsilon\mathbf{v}_1(\varepsilon^{-1}\phi(\mathbf{x},t),\mathbf{x},t) + \varepsilon^2\mathbf{v}_2(\varepsilon^{-1}\phi(\mathbf{x},t),\mathbf{x},t) + O(\varepsilon^3),$$

with the long space and time $\mathbf{x}, t = O(1)$. We further define the long phase $\theta(\mathbf{x},t) := \varepsilon^{-1}\phi(\mathbf{x},t)$ and refer to any derivatives of $\mathbf{v}_1$ ect. with respect to this variable as $\mathbf{v}_{1\theta}$. Substituting (WNE) into the governing equations gives, up to the second order,

$$[\phi_t \mathcal{A}(\mathbf{v}) + \phi_{x_\alpha} \mathcal{B}^\alpha(\mathbf{v})]\mathbf{v}_{1_\theta} + \varepsilon\big[(\phi_t \mathcal{A}(\mathbf{v}) + \phi_{x_\alpha} \mathcal{B}^\alpha(\mathbf{v}))\mathbf{v}_{2_\theta} \\ + \mathcal{A}(\mathbf{v})\mathbf{v}_{1_t} + \mathcal{B}^\alpha(\mathbf{v})\mathbf{v}_{1_{x_\alpha}} + \mathcal{C}(\mathbf{v})\mathbf{v}_1\big] = O(\varepsilon^2).$$

Note that all the matrices are still evaluated at $\mathbf{v}$ rather than e.g. $\mathbf{v}_1$. Different choices of the evaluation points will yield two differing ray formulations equivalent to those obtained by Hunter (1995) [3] and Prasad (2002) [6], respectively.

The Hunter formulation can be obtained by taking a Taylor expansion of the matrices around $\mathbf{0}$. This leaves two equations of order $O(\varepsilon^0)$ and $O(\varepsilon^1)$. The $O(\varepsilon^0)$ equation simplifies to the linear Eikonal equation,

$$\phi_t + c_0|\nabla\phi| = 0,$$

which we rewrite as a Hamiltonian system and solve computing bi-characteristics $(\mathbf{x}(s), \hat{\mathbf{n}}(s))$, where s is the ray coordinate, $\mathbf{x}(s)$ is the ray trajectory and $\hat{\mathbf{n}}(s)$ is the momentum

$$\frac{d\mathbf{x}}{ds} = c_0(\mathbf{x})\frac{\hat{\mathbf{n}}}{|\hat{\mathbf{n}}|} \qquad \mathbf{x}(0) = \mathbf{x}_0; \qquad \frac{d\hat{\mathbf{n}}}{ds} = -|\hat{\mathbf{n}}|\nabla c_0(\mathbf{x}) \qquad \hat{\mathbf{n}}(0) = \hat{\mathbf{n}}_0.$$

The above ray equations prescribe that ray moves at a speed c_0 in the direction of $\hat{\mathbf{n}}$ which turns depending on the gradient of the sound speed, ∇c_0. The order $O(\varepsilon^1)$ equation for the amplitude of the vector $\mathbf{v}_1$ along each ray is given by,

$$\text{(NTR)} \qquad a_s + \mathcal{G}aa_\theta + \mathcal{H}a = 0$$

$$\mathcal{G} = \frac{1}{\sqrt{2}\rho_0}\left(1 + \frac{B}{2A}\right) \qquad \mathcal{H} = \frac{1}{c_0}\frac{dc_0}{ds} + \frac{1}{2}\frac{1}{q}\frac{dq}{ds}.$$

We highlight the corresponding roles of the variables and operators: space-like role of the long phase θ, the time-like role of the ray parameter s, accumulation of the nonlinearity $\mathcal{G}$, and ray geometry $\mathcal{H}$ with $q(s)$ a measure of the geometrical spreading of the rays calculated using ray tubes [4]. Equation (NTR) can be transformed into the inviscid Burgers' equation using integral operators which transform the variables and the amplitude of the Burgers' solution. The Burger's solution itself only depends on the sound speed along the ray, the geometrical spreading and the initial condition. We obtain the solution of (NTR) by applying the ray dependent transformations to the the corresponding Burgers' solution. The waveform is, as expected, steepening towards the focus which is inherited from the Burgers' solution.

While this model seems very useful and applicable, as the ray equations are the same as in the linear ray theory, the rays only bend due to the sound speed of the medium. Hence for a focused source, such as the transducer used in HIFU, and a homogeneous background sound speed all the rays will cross at the focus point causing a caustic. This does not correspond to the reality where the rays are diffracted near the focus. To remedy this shortcoming, we artificially inject the diffraction into the model by numerically generating a background sound speed corresponding to linear diffraction. To this end we compute linear wave propagation from a curved bowl transducer for time harmonic initial condition with

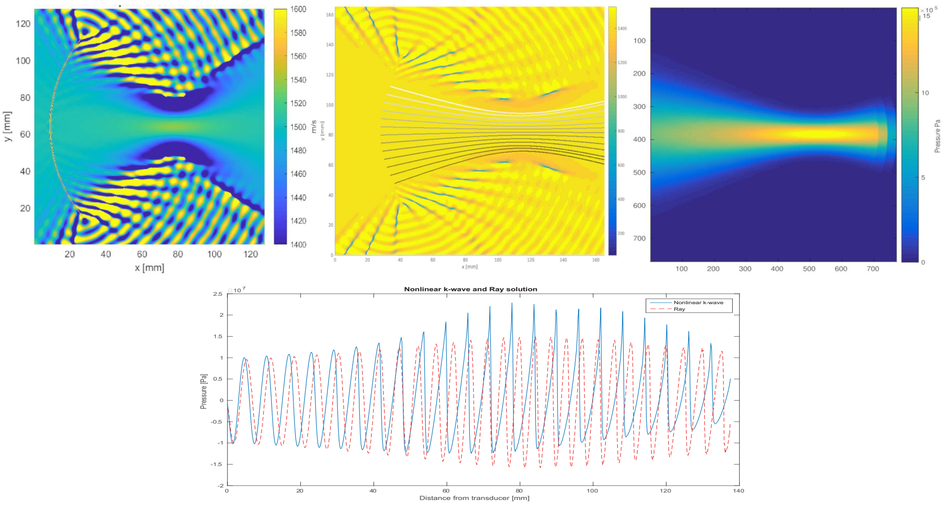

FIGURE 1. a) Diffracting background sound speed generated from linear solution using the Eikonal equation. b) Linear rays traced from focused bowl transducer through the diffracting sound speed in a). c) Nonlinear amplitude interpolated from the nonlinear amplitudes along the rays. d) Nonlinear ray amplitude versus nonlinear Westervelt k-Wave solution along the central ray.

frequency $\omega = 0.25MHz$ and homogeneous sound speed $1500m/s$ using an efficient method such as implemented in Acoustic Field Propagator function in k-Wave [5]. This provides a phase map for the entire wave which can be unwrapped and transformed into a diffracting sound speed using the Eikonal equation $c_0 = \frac{\omega}{|\nabla\phi(x)|}$. Tracing linear rays, as in Hunter's formulation, through this diffracting sound speed, causes them to bend away from the focus and each other eliminating the nonphysical caustic.

There are two limitations of the Hunter's ray model: i) the ray geometry is not affected by the wave amplitude, and ii) it does not model the phase shift of the harmonics at the focus. The first limitation is circumvented by Prasad's formulation [6], while the second is a fundamental limitation of ray based approaches.

REFERENCES

[1] B. Engquist and O. Runborg. *Acta Numerica*, (2003) 12, 181-266
[2] M.F. Hamilton and D.T. Blackstock. Nonlinear Acoustics: Theory and Applications. **Chp 3**, *Elsevier Science Publishing Co Inc*, (1998) 41-63
[3] J.K. Hunter. *Surveys in Applied Mathematics*, (1995) 2, 167–276
[4] V. Cerveny. Seismic ray theory, **110** *Cambridge University Press*, (2001)
[5] B.E. Treeby and B.T. Cox. *Journal of Biomedical Optics*, (2010), 15(2), 021314
[6] P.Prasad. Nonlinear Hyperbolic Waves in Multi-Dimensions, **Chp 4**, *Chapman and Hall/CRC*, (2002) 143-171

Duality for Neural Network Inverse Problems through Reproducing Kernel Banach Spaces

Christoph Brune
(joint work with Len Spek, Tjeerd Jan Heeringa)

Reproducing Kernel Hilbert spaces (RKHS) have been a very successful tool in various areas of machine learning. Recently, Barron spaces have been used to prove bounds on the generalization error for neural networks. Unfortunately, Barron spaces cannot be understood in terms of RKHS due to the strong nonlinear coupling of the weights. This can be solved by using the more general Reproducing Kernel Banach spaces (RKBS). We show that these Barron spaces belong to a class of integral RKBS. This class can also be understood as an infinite union of RKHS spaces. Furthermore, we show that the dual space of such RKBSs, is again an RKBS where the roles of the data and parameters are interchanged, forming an adjoint pair of RKBSs including a reproducing kernel. This enables the construction of saddle point problems for neural networks and potentially active learning techniques for inverse problems.

References

[1] L. Spek, T. J. Heeringa, F. Schwenninger, and C. Brune, *Duality for Neural Networks through Reproducing Kernel Banach Spaces* (2023), `https://arxiv.org/abs/2211.05020`

Directional regularization for the limited-angle Helsinki Tomography Challenge with the Core Imaging Library (CIL)

Jakob Sauer Jørgensen
(joint work with Gemma Fardell, Laura Murgatroyd, Evangelos Papoutsellis and Edoardo Pasca)

Last year the Finnish Inverse Problems Society organized the *Helsinki Tomography Challenge 2022* - an open competition for researchers to submit reconstruction algorithms for a challenging series of real-data limited-angle computed tomography problems [1]. This talk describes an algorithm submitted by the developer team of the Core Imaging Library (CIL) [2, 3] that made it to the third place in the competition. The algorithm consists of multiple stages: First, preprocessing including beam-hardening correction and data renormalization; second a purpose-built directional regularization method exploiting prior knowledge of the scanned objects; and finally a multi-Otsu segmentation method. The algorithm was fully implemented using the optimization prototyping capabilities of CIL and its performance assessed and optimized on the provided training data ahead of submission. The algorithm performed well on limited-angle data down to an angular range of 50 degrees, and in the competition was beaten only by two machine learning based strategies involving generation of very large sets of synthetic training data. In the spirit of open science, all the data sets are available from the challenge website [1] as well as Zenodo [4] and the submitted CIL algorithm code from [5].

References

[1] S. Latva-Äijö, A. Meaney, F. Moura, S. Rautio, S. Siltanen and T. Heikkilä, *Helsinki Tomography Challenge 2022*, `https://fips.fi/HTC2022`.

[2] J. S. Jørgensen, E. Ametova, G. Burca, G. Fardell, E. Papoutsellis, E. Pasca, K. Thielemans, M. Turner, R. Warr, W. R. B. Lionheart and P. J. Withers, *Core Imaging Library – Part I: a versatile Python framework for tomographic imaging*, Philosophical Transactions of the Royal Society A **379** (2021), 20200192. `https://doi.org/10.1098/rsta.2020.0192`.

[3] E. Papoutsellis, E. Ametova, C. Delplancke, G. Fardell, J. S. Jørgensen, E. Pasca, M. Turner, R. Warr, W. R. B. Lionheart and P. J. Withers, *Core Imaging Library – Part II: multichannel reconstruction for dynamic and spectral tomography*, Philosophical Transactions of the Royal Society A **379** (2021), 20200193. `https://doi.org/10.1098/rsta.2020.0193`.

[4] A. Meaney, F. Moura and S. Siltanen, *Helsinki Tomography Challenge 2022 open tomographic dataset (HTC 2022) (1.1.1)* [Data set]. Zenodo. `https://doi.org/10.5281/zenodo.6984868`.

[5] G. Fardell, J. S. Jørgensen, L. Murgatroyd, E. Papoutsellis and E. Pasca, *CIL-HTC2022-Algo2* [Software]. Github. `https://github.com/TomographicImaging/CIL-HTC2022-Algo2`.

Inversion Methods for Strain and Stiffness Reconstruction in Quantitative Optical Coherence Elastography

Ekaterina Sherina

(joint work with Lisa Krainz, Simon Hubmer, Otmar Scherzer, Wolfgang Drexler)

Elastography, as an imaging modality in general, aims at mapping the mechanical properties of a given sample. This modality is widely used in Medicine, in particular for the non-invasive identification of malignant formations inside the human skin or tissue biopsies during surgeries. In term of diagnostics accuracy, one is interested in quantitative values of strain and stiffness mapped on top of the visualization of a sample, rather than only in qualitative images.

In this work, we focus on optical coherence elastography (OCE), which requires the extraction of mechanical parameters from optical coherence tomographic (OCT) imaging data during compression of a sample. OCE is an emerging research area, however, it still lacks precision and reproducibility, which are important for clinical applications. Here, we are interested in quantitative OCE from the perspective of Inverse Problems. We propose and analyse inversion methods for strain and stiffness reconstruction. Moreover, we investigate the data quality and properties of reconstruction methods required for the successful application of this modality. Finally, inversion methods are compared to engineering approaches and the results are validated against the ground truth for 12 silicone elastomer phantoms obtained using both a tensile testing machine and macroscopic analysis.

Typically, OCE is implemented in two steps, mathematically formulated as two inverse problems - a reconstruction of the mechanical displacement (or strain) from OCT data of a sample undergoing a static compression, and a reconstruction of stiffness (the Young's modulus) from the displacement (or strain), see Figure 1(A).

Standard methods for strain extraction include cross-correlation, computer vision tools like optical flow, and registration methods. However, it was observed in [2] that standard tools display high inaccuracy when applied to imaging data

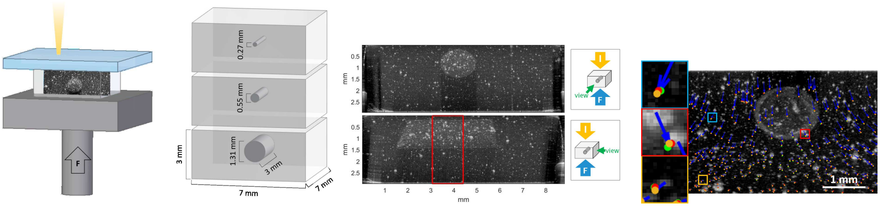

(A) (B) (C) (D)

Figure 1. (A) Schematic elastographic experiment - compression force from below, scanning from top. (B) Schematic phantoms. (C) Example of OCT imaging data. (D) A zoomed overlay of the tracked particle movement (yellow, blue), the simulated movement from the elastic model with ground truth (green) and in case the phantom were homogeneous (red) (taken from [1]).

from elastographic experiments. A-priori information about the underlying physics is required to accurately estimate the strain. We propose and analyse a novel computational method called elastographic optical flow method (EOFM), which combines particle tracking, physical boundary conditions, and background material assumptions into standard optical flow, see [2,3] for details. We compute the displacement field $\mathbf{u}$ as a sum of the homogeneous field $\mathbf{u}^{bg}$ (calculated from a homogeneous stiffness guess) and the update field $\mathbf{u}^{upd}$ minimizing

$$J(\mathbf{u}^{upd}) := \left\| I_t + \nabla I \cdot \mathbf{u}^{upd} + \nabla I \cdot \mathbf{u}^{bg} \right\|^2_{L^2(\Omega)} + \alpha \left\| \nabla \mathbf{u}^{upd} \right\|^2_{L^2(\Omega)}$$
$$+ \beta \sum_{i=1}^{n} \int_{\Omega} g_\sigma(\mathbf{x}, \hat{\mathbf{x}}^i) \left| \mathbf{u}^{upd} + \mathbf{u}^{bg} - \hat{\mathbf{u}}^i \right|^2 d\mathbf{x},$$

where I is an image intensity, $(\hat{\mathbf{x}}^i, \hat{\mathbf{u}}^i)$ are coordinates and displacement vectors of tracked particles, g_σ is a Gaussian function, and α, β are regularization parameters. Figure 2 shows the axial and lateral strains reconstructed using EOFM from imaging data, cf. Figure 1(C), for phantoms with geometry as in Figure 1(B) and silicone elastomers of three stiffnesses denoted by S10, S20 and S30.

Unknown mechanical properties of the sample can be subsequently estimated from computed displacements (or strains). However, it was observed in [1,4] that an elastographic experiment with a single compression allows for unique reconstruction of only one parameter such as Young's modulus. Moreover, the inverse problem is sensitive to data noise, which is illustrated in Figure 1(D) by the similarity between the three fields. Thus, a-priori information about the sample is required for successful parameter estimation. In this work, we look at four different reconstruction methods. First, we apply a full inversion method with nonlinear Landweber iteration from [4] to EOFM displacements. Second, we propose and

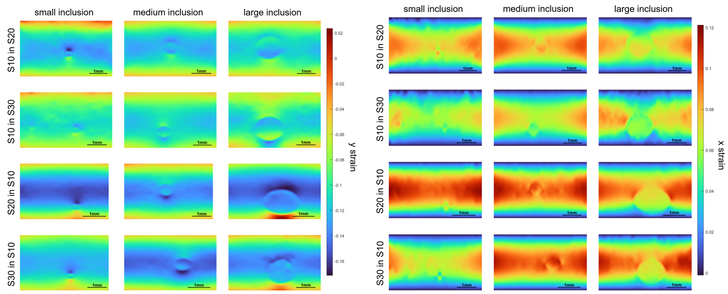

Figure 2. Axial and lateral components of the strain maps calculated from EOFM displacement fields (taken from [1]).

analyse the intensity-based inversion method (IIM) [1] formulated as a minimization of

$$G(E,\nu) := \|I_1(\mathbf{x}+\mathbf{u}(E,\nu)) - I_2(\mathbf{x})\|^2_{L^2(\Omega)} + \alpha\,\|(E,\nu)\|^2_{L^2(\Omega)}\,,$$

where I_1 and I_2 are OCT intensity images before and after compression, $\mathbf{u}$ is the displacement from the deformation model depending on Young's modulus E and Poisson's ratio ν, and α is the regularization parameter. Additional priors are included into IIM from segmentation and then one unknown per area of inclusion and background is estimated. We benchmark the IIM results against the results of two engineering approaches - a simple uniaxial reconstruction method and a EOFM strain-map based method with uniform stress assumption. The performance of the proposed inversion methods is demonstrated in Figure 3 on 12 silicone elastomer phantoms with inclusions of varying size and stiffness. We observe that IIM ben-

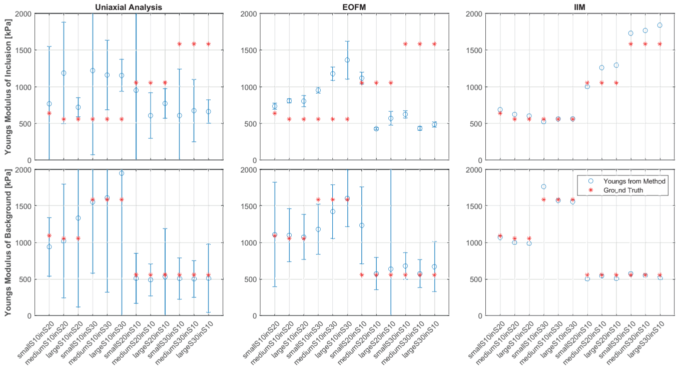

Figure 3. Comparison of the results from all three methods. The blue circles mark the values derived using 1D analysis, EOFM strain maps and IIM, respectively (taken from [1]).

efits from avoiding direct differentiation or division of the data (in comparison to full inversion or engineering approaches) and from taking into account the impact of the lateral sample expansion. Moreover, IIM is not limited to the model of linear elasticity used here, but can also be applied with any deformation model suitable for a specific experiment.

References

[1] L. Krainz, E. Sherina, S. Hubmer, M. Liu, W. Drexler and O. Scherzer, *Quantitative Optical Coherence Elastography: A novel Intensity-based Inversion Method versus Strain-based Reconstructions*, IEEE J. Sel. Top. Quantum Electron: Biophotonics **29(4)** (2023), 1–16.

[2] E. Sherina, L. Krainz, S. Hubmer, W. Drexler, and O. Scherzer, *Challenges for Optical Flow Estimates in Elastography*, In: A. Elmoataz, J. Fadili, Y. Quéau, J. Rabin, L. Simon (eds) Scale Space and Variational Methods in Computer Vision. SSVM 2021. Lecture Notes in Computer Science **12679** (2021), 128–139.

[3] E. Sherina, L. Krainz, S. Hubmer, W. Drexler, and O. Scherzer, *Displacement field estimation from OCT images utilizing speckle information with applications in quantitative elastography*, Inverse Probl. **36(12)** (2020), 124003.

[4] S. Hubmer, E. Sherina, A. Neubauer, and O. Scherzer, *Lamé Parameter Estimation from Static Displacement Field Measurements in the Framework of Nonlinear Inverse Problems*, SIAM J. Imaging Sciences **11(2)** (2018), 1268–1293.

Inverse problems for nonlocal PDEs with applications to quantum optics

John C. Schotland

We consider the following model for the interaction between a quantized field and a collection of two-level atoms [1]. The Hamiltonian H of the system is given by

$$H = H_F + H_A + H_I \ . \tag{1}$$

The Hamiltonian of the field, H_F, is of the form

$$H_F = \hbar c \int (-\Delta)^{1/2} \phi^\dagger(\mathbf{x})\phi(\mathbf{x}) \mathrm{d}\mathbf{x} \ , \tag{2}$$

where ϕ is a scalar bose field that obeys the usual commutation relations. The Hamiltonian of the atoms, H_A, is given by

$$H_A = \hbar\Omega \int \rho(\mathbf{x})\sigma^\dagger(\mathbf{x})\sigma(\mathbf{x}) \mathrm{d}\mathbf{x} \ , \tag{3}$$

where Ω is the atomic resonance frequency, $\rho(\mathbf{x})$ is the number density of the atoms, and σ is the atomic lowering operator. The Hamiltonian describing the interaction between the field and the atoms, H_I, is taken to be

$$H_I = \hbar g \int \rho(\mathbf{x}) \left(\phi^\dagger(\mathbf{x})\sigma(\mathbf{x}) + \sigma^\dagger(\mathbf{x})\phi(\mathbf{x})\right) \mathrm{d}\mathbf{x} \ , \tag{4}$$

where g is the strength of the atom-field coupling.

We suppose that the system is in a single-excitation state of the form

$$|\Psi\rangle = \int \mathrm{d}\mathbf{x} \left[\psi(\mathbf{x},t)\phi^\dagger(\mathbf{x}) + \rho(\mathbf{x})a(\mathbf{x},t)\sigma^\dagger(\mathbf{x})\right] |0\rangle \ , \tag{5}$$

where $|0\rangle$ is the combined vacuum state of the field and the ground state of the atoms. Here $a(\mathbf{x}, t)$ denotes the probability amplitude for exciting an atom at the point $\mathbf{x}$ at time t and $\psi(\mathbf{x}, t)$ is the amplitude for creating a photon. The state $|\Psi\rangle$ obeys the time-independent Schrodinger equation $H|\Psi\rangle = \hbar\omega|\Psi\rangle$, where $\hbar\omega$ is the energy. It follows that the amplitudes a and ψ, which are independent of time, obey the equations

$$c(-\Delta)^{1/2}\psi + g\rho(\mathbf{x})a = \omega\psi \ , \tag{6}$$

$$g\psi + \Omega a = \omega a \ . \tag{7}$$

By eliminating a from the above system, we immediately obtain the equation obeyed by ψ, which is given by

$$(-\Delta)^{1/2}\psi + V(\mathbf{x})\psi = k\psi \ , \tag{8}$$

where $k = \omega/c$ and $V(\mathbf{x}) = g^2/(c(\omega - \Omega))\rho(\mathbf{x})$.

We have considered the inverse problem of recovering the coefficient V from suitable measurements. We have shown that this is possible under a smallness condition on the measurements, which also guarantees the stability of the recovery. The reconstruction is based on inversion of the Born series, which expresses the solution to the inverse problem as an explicitly computable functional of the measured data. We note that this method has been extensively studied in the context of inverse problems for linear PDEs. The extension to the nonlocal setting involves a substantial reworking of the theory, especially the combinatorial structure of the Born series itself.

REFERENCES

[1] J. Kraisler and J. Schotland. Collective Spontaneous Emission and Kinetic Equations for One-Photon Light in Random Media. J. Math. Phys. **63**, 031901 (2022).

Reporters: Stephanie Blanke, Samira Kabri

Participants

Dr. Anuj Abhishek
Department of Mathematics
University of North Carolina
at Charlotte
9201 University City Boulevard
Charlotte, NC 28223-0001
UNITED STATES

Prof. Dr. Gaik Ambartsoumian
Department of Mathematics
University of Texas at Arlington
P. O. Box 19408
Arlington TX 76019-0408
UNITED STATES

Prof. Dr. Simon R. Arridge
Department of Computer Science
University College London
Gower Street
London WC1E 6BT
UNITED KINGDOM

Dr. Marta M. Betcke
Department of Computer Science
University College London
90 High Holborn
London WC1V 6LJ
UNITED KINGDOM

Stephanie Blanke
Department Mathematik
Universität Hamburg
Bundesstr. 55
20146 Hamburg
GERMANY

Prof. Dr. Jan Boman
Matematiska Institutionen
Stockholms Universitet
106 91 Stockholm
SWEDEN

Prof. Dr. Christoph Brune
Department of Applied Mathematics
Faculty of Electrical Engineering,
Mathematics and Computer Science
University of Twente
Drienerlolaan 5
P.O. Box 217
7500 AE Enschede
NETHERLANDS

Dr. Tatiana Bubba
Dept. of Mathematical Sciences
University of Bath
Claverton Down
BA2 7AY Bath
UNITED KINGDOM

Prof. Dr. Martin Burger
Department Mathematik
Universität Erlangen-Nürnberg
Cauerstraße 11
91058 Erlangen
GERMANY

Dr. Matias Courdurier
Facultad de Matématicas
Pontificia Universidad Católica de Chile
Avda. Vicuna Mackenna 4686, Macul
7820436 Santiago
CHILE

Dr. Alejandro Coyoli
PTC
121 Seaport Blvd
Boston, MA 02210
UNITED STATES

Dr. Yiqiu Dong
DTU Compute
Technical University of Denmark
Bldg. 303
2800 Lyngby
DENMARK

Mathias Feinler
Fachbereich Mathematik
Universität Stuttgart
Pfaffenwaldring 57
70569 Stuttgart
GERMANY

Prof. Dr. Jürgen Frikel
Department of Computer Science
and Mathematics
OTH Regensburg
Galgenbergstraße 32
93053 Regensburg
GERMANY

Prof. Dr. Bernadette Hahn
Fachbereich Mathematik
Universität Stuttgart
Pfaffenwaldring 57
70569 Stuttgart
GERMANY

Prof. Dr. Markus Haltmeier
Department of Mathematics
University of Innsbruck
Technikerstraße 13
6020 Innsbruck 6020
AUSTRIA

Assoc. Prof. Dr. Andreas Hauptmann
Research Unit of Mathematical Sciences
University of Oulu
FI-90014 University of Oulu
Pentti Kaiteran katu 1
P.O.Box 8000
90014 Oulu
FINLAND

Prof. Dr. Tapio Helin
Department of Computational
Engineering
LUT University
53851 Lappeenranta
FINLAND

Prof. Dr. Ming Jiang
School of Mathematical Sciences
Peking University
5 Yi He Yuan Street
Beijing 100 871
CHINA

Samira Kabri
Department Mathematik
Universität Erlangen-Nürnberg
Cauerstr. 11
91058 Erlangen
GERMANY

Prof. Dr. Alexander Katsevich
Department of Mathematics
University of Central Florida
Orlando, FL 32816-1364
UNITED STATES

Lorenz Kuger
Department Mathematik
Universität Erlangen-Nürnberg
Cauerstr. 11
91058 Erlangen
GERMANY

Prof. Dr. Leonid Kunyansky
Department of Mathematics
University of Arizona
617 N. Santa Rita
Tucson AZ 85721-0089
UNITED STATES

Prof. William R.B. Lionheart
Department of Mathematics
University of Manchester
Alan Turing Building
Oxford Rd.
Manchester M13 9PL
UNITED KINGDOM

Prof. Dr. Alfred K. Louis
Fakultät für Mathematik und Informatik
Universität des Saarlandes
66041 Saarbrücken
GERMANY

Dr. Felix Lucka
Centrum Wiskunde & Informatica
(CWI)
Science Park 123
1098 XG Amsterdam
NETHERLANDS

Prof. Dr. Peter Maaß
FB 3 - Mathematik und Informatik
Zentrum für Technomathematik
Universität Bremen
Postfach 330 440
28334 Bremen
GERMANY

Prof. Dr. Voichita Maxim
CREATIS and Centre de Mathématiques
INSA Lyon
21, avenue Jean Capelle
69621 Villeurbanne Cedex
FRANCE

Marius Nitzsche
Fachbereich Mathematik
Universität Stuttgart
Pfaffenwaldring 57
70569 Stuttgart
GERMANY

Prof. Dr. Eric Todd Quinto
Department of Mathematics
Tufts University
177 College Avenue
Medford, MA 02155
UNITED STATES

Prof. Dr. Ronny Ramlau
Industrial Mathematics Institute
Johannes Kepler University
Altenberger Strasse 69
4040 Linz
AUSTRIA

Prof. Dr. Andreas Rieder
Fakultät für Mathematik
Institut für Angewandte und
Numerische Mathematik
Karlsruher Institut für Technologie
(KIT)
Englerstraße 2
76131 Karlsruhe
GERMANY

PD Dr. Gaël Rigaud
Fachbereich Mathematik
Universität Stuttgart
Pfaffenwaldring 57
70569 Stuttgart
GERMANY

Prof. Dr. Tim Salditt
Georg-August-Universität Göttingen
Institut für Röntgenphysik
Friedrich-Hund-Platz 1
37077 Göttingen
GERMANY

Dr. Jakob Sauer Jørgensen
Department of Applied Mathematics and
Computer Science
Technical University of Denmark
Richard Petersens Plads, Building 324
Lyngby 2800
DENMARK

Prof. Dr. Otmar Scherzer
Fakultät für Mathematik
Universität Wien
Oskar-Morgenstern-Platz 1
1090 Wien
AUSTRIA

Denise Schmutz
Institut für Mathematik
Universität Wien
Oskar-Morgenstern-Platz 1
1090 Wien
AUSTRIA

Prof. Dr. John C. Schotland
Department of Mathematics
Yale University
Box 208 283
New Haven, CT 06520
UNITED STATES

Prof. Dr. Thomas Schuster
Fachrichtung Mathematik
Universität des Saarlandes
Postfach 151150
66041 Saarbrücken
GERMANY

Prof. Dr. Jin Keun Seo
School of Mathematics and Computing
(Computational Science and
Engineering)
Yonsei University
Seoul 120-749
KOREA, REPUBLIC OF

Dr. Ekaterina Sherina
Fakultät für Mathematik
Universität Wien
Oskar-Morgenstern-Platz 1
1090 Wien
AUSTRIA

Prof. Dr. Samuli Siltanen
Department of Mathematics and
Statistics
University of Helsinki
P.O. Box 68
00014 University of Helsinki
FINLAND

Prof. Dr. Plamen Stefanov
Department of Mathematics
Purdue University
150 N. University Street
West Lafayette IN 47907-2067
UNITED STATES

JProf. Dr. Anne Wald
Institut für Numerische
und Angewandte Mathematik
Universität Göttingen
37083 Göttingen
GERMANY

Dr. James Webber
Brigham and Women's Hospital
15 Winslow Road
Belmont MA 02478
UNITED STATES

Prof. Dr. Benedikt Wirth
Fachbereich Mathematik und Informatik
Universität Münster
Einsteinstraße 62
48149 Münster
GERMANY